Investigation and development of novel oxygen permeable membranes for high-purity oxygen production

Von der Naturwissenschaftlichen Fakultät
der Gottfried Wilhelm Leibniz Universität Hannover
zur Erlangung des Grades

Doktor der Naturwissenschaften
Dr. rer. nat.

genehmigte Dissertation

von

M.Sc. Dipl.-Ing. (FH) Fangyi Liang

geboren am 05.04.1979 in Anhui, China

2013

Referent:	Prof. Dr. Jürgen Caro
Korreferentin:	Prof. Dr. Carla Vogt
Tag der Promotion:	28.01.2013

Preface

The presented results of this thesis were obtained since October 1, 2009 during my Ph. D. study at the Institute of Physical Chemistry and Electrochemistry at the Gottfried Wilhelm Leibniz Universität Hannover under the supervision of Prof. Dr. Jürgen Caro. In this period, I have also been a scientific co-worker and worked for the European project NEXT – GTL (Innovative catalytic technologies & materials for next gas to liquid processes).

Five research articles in which I have been the first author or the co-author are presented within this thesis. The following statement will point out my contribution to the articles collected in this thesis. For all these articles, I would like to acknowledge the fruitful discussions and valuable comments from the co-authors and referees, particularly from Prof. Dr. J. Caro, Prof. Dr. A. Feldhoff, Dr. H.Q. Jiang, Dr. H.X. Luo and M.Sc. K. Partovi.

Two articles, *Phase stability and permeation behavior of a dead-end* $Ba_{0.5}Sr_{0.5}Co_{0.8}Fe_{0.2}O_{3-\delta}$ *tube membrane in high-purity oxygen production* and *High-purity oxygen production by a dead-end* $Ba_{0.5}Sr_{0.5}Co_{0.8}Fe_{0.2}O_{3-\delta}$ *tube membrane*, are collected in Chapter 2. I wrote the first draft of those articles and got support on the manuscripts preparation from all the co-authors, especially from Prof. Dr. J. Caro, Prof. Dr. A. Feldhoff and Dr. H.Q. Jiang. The measurements of oxygen permeation and SEM, EDXS characterizations were mainly completed by myself. The dead-end BSCF tubes were produced by Dr. R. Kriegel from the Fraunhofer Institute IKTS Dresden/Hermsdorf (Germany). (HR)TEM, HAAD, EELS and SEAD characterizations and data interpretation were done by Prof. Dr. A. Feldhoff. Dr. H.X. Luo also gave many valuable suggestions to improve it.

The article, *High-Purity Oxygen Production Using Perovskite Hollow Fiber Membranes*, was written by me. Prof. Dr. J. Caro and Dr. H.Q. Jiang improved it. The dense hollow fiber membranes $BaCo_xFe_yZr_{1-x-y}O_{3-\delta}$ were provided by Dr. T. Schiestel from the Fraunhofer Institute of Interfacial Engineering and Biotechnology (IGB) in Stuttgart. All the measurements, calculations and interpretation were mainly carried out by myself. Additionally, I obtained support on the manuscript preparation from all co-authors.

Another article, *B-site La-doped BaFe$_{0.95-x}$La$_x$Zr$_{0.05}$O$_{3-\delta}$ perovskite-type membranes for oxygen separation* focusing on novel cobalt-free membranes for oxygen separation was collected in Chapter 4. I wrote the first draft and Prof. Dr. J. Caro spent much time on correcting and improving it. The BaFe$_{0.95-x}$La$_x$Zr$_{0.05}$O$_{3-\delta}$ powder was prepared by K. Partovi following my idea. All the measurements of oxygen permeation and SEM, EDXS characterizations were done by K. Partovi and me together. Dr. H.Q. Jiang and Dr. H.X. Luo also gave many valuable suggestions to improve it.

Another article, *A novel cobalt-free noble metal-free oxygen-permeable 40Pr$_{0.6}$Sr$_{0.4}$FeO$_{3-\delta}$ - 60Ce$_{0.9}$Pr$_{0.1}$O$_{2-\delta}$ dual phase membrane* was written by my colleague Dr. H.X. Luo. My contribution was to carry out oxygen permeation measurements and to share experimental knowledge.

All together, I have developed and investigated four membranes with different geometry (disc, tubular and hollow fiber) and chemical composition (Ba$_{0.5}$Sr$_{0.5}$Co$_{0.8}$Fe$_{0.2}$O$_{3-\delta}$, BaCo$_x$Fe$_y$Zr$_{1-x-y}$O$_{3-\delta}$, BaFe$_{0.95-x}$La$_x$Zr$_{0.05}$O$_{3-\delta}$, and 40Pr$_{0.6}$Sr$_{0.4}$FeO$_{3-\delta}$ - 60Ce$_{0.9}$Pr$_{0.1}$O$_{2-\delta}$) for oxygen permeation from air.

Acknowledgement

I would like to express my grateful appreciation to all the persons who have helped and encouraged me during my Ph.D. thesis research at the Institute of Physical Chemistry and Electrochemistry at the Gottfried Wilhelm Leibniz Universität Hannover.

First of all, I would like to express the deepest gratitude to my supervisor Prof. Dr. Jürgen Caro for giving me this opportunity to study and carry out this interesting scientific work in his group. I am deeply grateful for his fruitful support and patient guidance throughout my Ph. D. study. Especially, I am profoundly impressed by his hard-working attitude and his dedication to science. I have been fortunate to benefit from his many years of experience in research and his research insight. I also thank him for his enthusiasm in assisting me when I met problems in my daily life.

Furthermore, I thank Prof. Dr. Carla Vogt from the Institute for Inorganic Chemistry at the Gottfried Wilhelm Leibniz Universität Hannover for her kind interest in this work and for the acceptance to conduct the second expertise.

I would also like to thank Dr. Heqing Jiang, Prof. Dr. Armin Feldhoff, Prof. Dr. Haihui Wang and Dr. Huixia Luo for their valuable discussions and comments throughout my work. Special thanks go to Dr. Heqing Jiang for his help in the beginning of my Ph.D. A special acknowledgement is given to Prof. Dr. Haihui Wang and Dr. Huixia Luo for the lively discussion and the exchanges of knowledge. Exceptional thanks go to Prof. Dr. Armin Feldhoff for his valuable cooperation on TEM measurements.

Furthermore, I am very grateful to Prof. Dr. Yanshuo Li, Prof. Dr. Aisheng Huang, Dr. Helge Bux, Dr. Yi Liu, M.Sc. Zhengwen Cao, M.Sc. Nanyi Wang, Dr. Konstantin Efimov, Dr. Oliver Merka, Dipl.-Chem. Tobias Klande, Dr. Oliver Czuprat, and M.Sc. Kaveh Partovi for their assistance and helpful cooperation in the past three years. Special gratitude goes to Prof. Dr. Yanshuo Li, Prof. Dr. Aisheng Huang, Dr. Helge Bux for the fruitful collaboration in MOFs and Zeolite membranes. I am very pleased to share the office with Dr. Konstantin Efimov, Dr. Huixia Luo and M.Sc. Zhengwen Cao. I also thank Dr. Konstantin Efimov, Dipl.-Chem. Tobias Klande and Dr. Oliver Merka for their so kind help for XRD measurements.

I would like to give many thanks to Yvonne Gabbey-Uebe, Kerstin Janze, and Frank Steinbach for their kind supports in the technical or the administrative aspects in the past three years. I am very happy with the nice atmosphere in Prof. Caro's group. I want to express my gratitude to all the former and current members of our group for their kindness, help and friendship, especially Prof. Dr. Michael Wark, Dr. Monir Sharifi, Dr. Amira Ahmed, Dr. Jana Panke, Dr. Christian Dunkel, Dr. Florian Bittner, and Dipl.-Chem. Olga Wittich. I appreciate the great job done by the mechanical and electrical workshop, my special thanks to Mr. Bieder, Mr. Egly, Mr. Becker, Mr. Rogge, and Mr. Ribbe.

Finally, but not least, I would like to express my deepest thanks and regards to my dear parents, brother, sisters for their understandings, unlimited support, unconditional love, sacrifice and encouragement. My personal thanks go to my loving wife Juan for her support and unconditional love, and also to my lovely son Shaobo for being the sunshine and joy of my life.

Abstract

Oxygen transporting membranes (OTMs), based on mixed electronic and ionic conductors of perovskite-type oxides, have promising potential applications for high purity oxygen production, in catalytic membrane reactors and as cathodes in solid oxide fuel cells (SOFCs). In practice, the oxygen permeability and stability of OTMs under harsh operating conditions such as intermediate temperatures, large oxygen partial pressure gradients, are crucial for their industrial applications.

In the chapter 2, phase stability of cobalt-based perovskite-type $Ba_{0.5}Sr_{0.5}Co_{0.8}Fe_{0.2}O_{3-\delta}$ (BSCF) membrane for the high-purity oxygen production was first investigated. After the identification of stable operation conditions for the BSCF membrane, high-purity oxygen was produced from air in a dead-end BSCF tube membrane. Good BSCF stability was found when the BSCF membrane was operated at temperatures $\geq$ 850 °C and oxygen with a purity of almost 100 vol.% was obtained.

In the chapter 3, the Zr-doped $Ba_{1-x}Sr_xCo_{1-y}Fe_yO_{3-\delta}$ (BCFZ) hollow fiber membrane with better stability was also investigated for the oxygen production. Compared to the conventional disk and tubular membranes, membranes with hollow fiber geometry give not only high oxygen permeability but also lower materials costs because of very high values of the membrane area per unit volume. A high oxygen purity up to 99.9 vol.% and high permeation rates of almost 10 $cm^3(STP)cm^{-2}min^{-1}$ were obtained at 900 °C in a 150 h operation.

In the chapter 4, B-site La-doped $BaFe_{0.95-x}La_xZr_{0.05}O_{3-\delta}$ (BFLZ) perovskite-type oxide was developed as a novel cobalt-free OTM for oxygen separation in the intermediate temperature range. It was first time that the introduction of La on the B-site of a mixed oxide was successful and stabilized the cubic structure. Stable oxygen permeation fluxes of 0.63 and 1.24 $cm^3(STP)min^{-1}cm^{-2}$ were obtained during the long-term oxygen permeation operation of the BFLZ (x = 0.04) membrane over 170 h at 750 and 950 °C, respectively.

In the last chapter, a novel cobalt-free noble metal-free dual phase OTM with the composition $40Pr_{0.6}Sr_{0.4}FeO_{3-\delta}$ - $60Ce_{0.9}Pr_{0.1}O_{2-\delta}$ (40PSFO-60CPO) was studied for oxygen permeation using pure He and CO_2 as sweep gas and the partial oxidation of methane to synthesis gas.

Keywords: Oxygen transporting membrane, Perovskit, cubic structure, phase stability Oxygen permeation.

Zusammenfassung

Sauerstofftransportierende Membranen (OTM) als sowohl Elektronen als auch Sauerstoffionen gemischt leitende keramische Materialien haben vielversprechende Einsatzmöglichkeiten, z.B. für die Produktion von hochreinem Sauerstoff, in katalytischen Membranreaktoren und als Kathoden in Festoxidbrennstoffzellen (SOFC). Für die industrielle Praxis werden insbesondere eine hohe Sauerstoffpermeation und die Phasenstabilität der OTMs unter rauen Betriebsbedingungen wie z.B. bei hohen und mittleren Temperaturen, hohen Sauerstoffpartialdruckgradienten, in Anwesenheit reduzierender und reaktiver Gase, die entscheidenden Parametern für ihre erfolgreiche Anwendung sein.

Die Phasenstabilität der kobalthaltigen Perowskitmembran $Ba_{0.5}Sr_{0.5}Co_{0.8}Fe_{0.2}O_{3-\delta}$ (BSCF) bei der Herstellung von hochreinem Sauerstoff wurde im Kapitel 2 untersucht. Nach der Identifizierung der stabilen Betriebsbedingungen für die BSCF-Membran wurde hochreiner Sauerstoff aus Luft mit einer einseitig verschlossenen BSCF-Rohrmembran abgetrennt. Wenn die BSCF-Membran bei Temperaturen größer als 850 °C betrieben wurde, erwies sie sich als stabil, und Sauerstoff mit einer Reinheit von nahezu 100 % wurde erhalten.

In Kapitel 3 wurden Zr-dotierte $Ba_{1-x}Sr_xCo_{1-y}Fe_yO_{3-\delta}$ (BCFZ)-Hohlfasermembranen für die permeative Sauerstoffherstellung untersucht. Verglichen mit den herkömmlichen Scheiben- und Rohrmembranen geben die Hohlfasermembranen auf Grund ihrer geringen Wanddicke von < 100 µm nicht nur eine hohe Sauerstoffpermeanz sondern auch geringere Materialkosten, weil Hohlfasermembran eine hohe Membranfläche pro Volumeneinheit ermöglichen. Eine hohe Sauerstoffreinheit bis zu 99,9 % und eine hohe Sauerstoffpermeation von fast 10 $cm^3(STP)cm^{-2}min^{-1}$ wurden konstant über 150 h bei 900 °C gemessen.

In Kapitel 4 wurde eine auf der B-Position La-dotierte $BaFe_{0.95-x}La_xZr_{0.05}O_{3-\delta}$ (BFLZ) Membran als neue kobaltfreie OTM für die Sauerstoff-Trennung im mittleren Temperaturbereich entwickelt. Es wurde erstmals gezeigt, dass das relativ große La^{3+}-Ion auf die B-Position gebracht werden kann und dadurch die kubische Struktur stabilisiert. Stabile Sauerstoffpermeationsraten von 0,63 und 1,24 $cm^3(STP)cm^{-2}min^{-1}$ wurden während der Langzeitpermeation einer BFLZ (x = 0,04)-Membran über 170 h bei 750 und 950 °C gemessen.

In Kapitel 5 wurde eine neue kobaltfreie und edelmetallfreie zweiphasige OTM der Zusammensetzung $40Pr_{0.6}Sr_{0.4}FeO_{3-\delta} - 60Ce_{0.9}Pr_{0.1}O_{2-\delta}$ (40PSFO-60CPO) entwickelt und in der Sauerstoffpermeation sowie partiellen Oxidation von Methan zu Synthesegas untersucht.

Schlagwörter: Sauerstofftransportierende Membran, Perowskit, kubische Struktur, Phasenstabilität, Sauerstoffpermeation.

Content

1   Introduction

1.1   Motivation

Oxygen is the third-largest-volume chemical produced worldwide,[1] and most of the industrial applications for oxygen require high-purity oxygen. Depending on the amount and the purity of oxygen needed, several techniques are available to separate oxygen from air. The cryogenic fractionation technology after Linde can produce pure oxygen with oxygen concentration > 99 vol.%. Pressure swing adsorption (PSA)[2] can give oxygen with a purity of up to 95-97 vol.%. The membrane technology is also used for air-to-oxygen production. Because of the low separation factor, the oxygen enrichment of polymeric membranes[3] is of the order of around 50 vol.%. Dense perovskite ceramic membranes with mixed oxygen-ionic and electronic conductivity[4-7] provide a promising way for oxygen production. At high temperatures, oxygen-transporting membranes (OTMs) can separate oxygen from air, which is a gas mixture containing approximately 78 vol.% N_2 and 21 vol.% O_2,[8] or from other oxygen-containing gases. High-temperature air separation process can be better combined with the cycle coal gasification plants and other advanced power generation systems. OTMs can theoretically produce oxygen at purities of up to 100 % and are believed to possess the potential to reduce by 35 % the cost of high-purity oxygen production and 35 – 60 % energy compared to the conventional cryogenic processes.[9] Moreover, OTM reactors have been developed for such potential applications as the partial oxidation of hydrocarbons,[10-13] the production of hydrogen by thermal water splitting in combination with olefin and synthesis gas production,[14-16] and the decomposition of nitrogen oxides.[17, 18]

After Teraoka [19, 20] reported the pioneering papers about oxygen permeation through a $La_{1-x}A_xCo_{1-y}Fe_yO_{3-\delta}$ perovskite membrane, in the past few decades, many OTMs with high oxygen permeabilities have been developed that are based on mixed ionic-electronic conductors (MIEC) solid oxides, such as $Ba_{1-x}Sr_xCo_{1-y}Fe_yO_{3-\delta}$,[21, 22] and $La_{1-x}Sr_xCo_{1-y}Fe_yO_{3-\delta}$, [19, 23, 24] $BaCo_{0.4}Fe_{0.4}Zr_{0.2}O_{3-\delta}$,[25] $BaCo_{0.7}Fe_{0.2}Ta_{0.1}O_{3-\delta}$,[26] $Ba_{0.5}Sr_{0.5}Fe_{0.9}Al_{0.1}O_{3-\delta}$,[27] and $Ba_{0.5}Sr_{0.5}Fe_{0.8}Cu_{0.2}O_{3-\delta}$.[28] In practice, the oxygen permeability and stability of OTM under harsh operating conditions such as

intermediate temperatures, large oxygen partial pressure gradients, or reducing atmospheres, are crucial for their industrial applications. Despite much R&D effort, there is still no perovskite-type membrane in industrial application. This lack of applications is mainly due to the long-term stability problems of perovskites especially at low oxygen partial pressure at the usual operation temperature near 850 °C. Often high oxygen fluxes reduce the stability and vice versa.

Among the OTM materials, the cobalt-based perovskite-type membrane such as $(La_xSr_{1-x})(Co_yFe_{1-y})O_{3-\delta}$ or $(Ba_xSr_{1-x})(Co_yFe_{1-y})O_{3-\delta}$ are often thought to be the most promising materials because they show very good oxygen permeability. However, Cobalt-based membranes usually have a stability problem under reducing conditions or in the intermediate temperature (i.e. approximately 500-850°C) range. $Ba_{0.5}Sr_{0.5}Co_{0.8}Fe_{0.2}O_{3-\delta}$ (BSCF) with high oxygen permeability, which assumes a cubic perovskite structure, has been regarded as one of the most promising materials for oxygen separation from air[21, 22, 29-31] and as cathodes in solid oxide fuel cells (SOFCs).[32] Because of the high concentration of the mobile oxygen vacancies in the perovskite lattice,[33] BSCF exhibits a very high oxygen-permeation flux over a wide temperature range.[21] However, during operation in the intermediate temperature range, the oxygen-permeation flux through the BSCF membrane has been observed to decrease, which has been attributed in several reports to a partial decomposition of the bulk cubic perovskite phase.[34-39]

To improve the stability of the cobalt-based perovskite-type membrane, the reducible B-site ions (Co^{4+}/Co^{3+}, Fe^{4+}/Fe^{3+}) can be partially substitute by cations with constant valence (Ta^{5+}, Nb^{5+}, Zr^{4+}, Al^{3+}). Examples are $BaCo_{0.7}Fe_{0.2}Ta_{0.1}O_{3-\delta}$,[40, 41] $Ba_{1.0}Co_{0.7}Fe_{0.2}Nb_{0.1}O_{3-\delta}$,[42] $BaCo_{0.4}Fe_{0.6-x}Zr_xO_{3-\delta}$,[43] $BaCo_{0.4}Fe_{0.4}Zn_xZr_{0.2-x}O_{3-\delta}$,[27] $La_{0.3}Sr_{0.7}(Fe,Ga)O_{3-\delta}$,[44] and $Sr(Fe,Al)O_{3-\delta}$.[45]

Another way to solve the stability of the cobalt-based perovskite-type membrane is to develop the cobalt-free perovskite-type membrane with high oxygen permeability, such as $La_{1-x}Sr_xFeO_{3-\delta}$,[46] $Ba_{0.3}Sr_{0.7}FeO_{3-\delta}$,[47] $BaFe_{1-y}Ce_yO_{3-\delta}$,[48] $Ba_{0.5}Sr_{0.5}Fe_{0.8}Zn_{0.2}O_{3-\delta}$,[49] $Ba_{0.5}Sr_{0.5}Fe_{1-x}Al_xO_{3-\delta}$,[27] $(Ba_{0.5}Sr_{0.5})(Fe_{0.8}Cu_{0.2})O_{3-\delta}$,[28] $BaFe_{1-y}Zr_yO_{3-\delta}$,[50] and $Ba_{0.95}La_{0.05}FeO_{3-\delta}$.[51]

An alternative to the signal phase OTMs can be dual phase OTMs. Dual phase

OTMs which consist of an oxygen ionic conducting phase and an electronic conducting phase in a micro-scale phase mixture are considered to be promising substitutes for the single phase MIEC materials. The first generation of dual phase membranes consist of noble metal (such as Ag, Pd) powders as electronic and a ceramic particles as ionic conductors.[52-55] The second generation consist of two oxides, where one of the oxides acts as electron conductor instead of the noble metal.[56-59] At present, the novel cobalt-free noble-metal free dual-phase membrane material are attracting much interest due to the good phase stability in CO_2 and reducing atmospheres, their chemical compositions can be tailored according to practical requirements.

The main aims of this thesis are first to elucidate the reason of phase stability of cobalt-based perovskite-type BSCF membrane for the high-purity oxygen production in the high temperature and the intermediate temperature rang in the chapter 2. After the identification of stable operation conditions for the BSCF membrane, in the second part of the this chapter, high-purity oxygen was produced from air in a dead-end BSCF tube membrane by using (i) pressurized air/O_2-enriched air as feed, (ii) reduced pressure on the permeate side, and (iii) a combination of both. In the chapter 3, the Zr-doped BCFZ hollow fiber membrane with better stability was also investigated for the oxygen production. Compared to the conventional disk and tubular membranes, membranes with hollow fiber geometry give not only high oxygen permeability but also lower materials costs because of very high values of the membrane area per unit volume. In the chapter 4, B-site La-doped $BaFe_{0.95-x}La_xZr_{0.05}O_{3-\delta}$ (BFLZ) perovskite-type oxide was developed as a novel cobalt-free OTM for oxygen separation in the intermediate temperature rang. In the last chapter, a novel cobalt-free noble metal-free dual phase oxygen transporting membrane with the composition $40Pr_{0.6}Sr_{0.4}FeO_{3-\delta}$ - $60Ce_{0.9}Pr_{0.1}O_{2-\delta}$ (40PSFO-60CPO) was studied for oxygen permeation using pure He and CO_2 as sweep gas and the partial oxidation of methane (POM) to synthesis gas.

1.2   Oxygen separation technology

About 100 Mio tons of oxygen is produced every year from air by different separation techniques, and oxygen is used in almost every industrial sector for numerous applications.[60] The production of oxygen was based two technical approaches, which are cryogenic distillation and non-cryogenic distillation. The cryogenic distillation technology is currently the most cost-effective and effective process and uses the boiling point differences to separate oxygen from nitrogen and other constituents of air at ultra-low-temperature. The cryogenic distillation is typically for producing large quantities of oxygen with high recoveries and purities. The cryogenic fractionation technology after Linde can produce pure oxygen with an oxygen concentration > 99 vol.%. The first patent on cryogenic air separation plant for the production of oxygen was issued in 1902, now it is a proven and reliable process through continuous technology research and development. Due to the overall thermodynamic efficiency of the modern-day cryogenic air separation technology, this technique is likely reaching its theoretical limits, the cost of producing oxygen by the cryogenic air separation technology are unlikely to get reduced remarkably.[1]

The non-cryogenic distillation involves the pressure swing adsorption (PSA), which is based on the adsorption ability differences of gas species using molecular sieve adsorption, and the membrane separation process which is based on the difference in diffusion rates of gas species. Pressure swing adsorption (PSA) is a common technology. Zeolites are typical adsorbent materials in PSA processes for oxygen production. In PSA, oxygen is produced by passing air through a vessel containing adsorbent materials. PSA can give oxygen with a purity of up to 95-97 vol.%. Bed size is the controlling factor in the capital costs due to the cyclic nature of the adsorption process. Since production rate depends on the bed volume, capital costs increase linearly as a function of production rate compared to cryogenic plants. Efficiency limitations inherent in adsorption technology restrict its application to relatively small plants.

Membrane separation process for production of oxygen is currently using organic polymeric hollow-fiber membranes. Due to the smaller size of the oxygen molecule, most membrane materials are more permeable to oxygen than to nitrogen. The flux and the Selectivity are the two key parameters for the separation process. The O_2

concentration in the permeate is typically of the order of 30-50 vol.% under a pressure difference of about 10 bar.[3] Carbon dioxide and water usually appear in the permeate side, since they are more permeable than oxygen for most polymeric membranes. Polymeric membranes allow the production of oxygen enriched air and do not provide the separation factor and flux required for economical large-scale production of oxygen.

OTM produces oxygen by the passage of oxygen ions through the ceramic crystal structure. High purity oxygen (theoretically up to 100 %) can be obtained using OTM. Oxygen can be separated from air using OTM at high temperatures and pressures with high flux and purity in a single-stage operation. The OTM oxygen technology provide a radically different approach to producing low-cost, high-purity tonnage oxygen at temperatures synergistic with power production and many other oxygen intensive applications. If OTM oxygen systems combine cycle coal gasification plants and other advanced power generation systems, the cost of large-scale oxygen production from air can be reduced by approximately one-third compared to conventional cryogenic air separation technologies.[9]

1.3   Basic aspects of oxygen transporting membranes

Recently, oxygen transporting membranes (OTMs) with mixed ionic-electronic conductivity are attracting more and more attention as economical, efficient, and environment-friendly means to separate oxygen from air or other oxygen-containing gases with a high purity of theoretically up to 100 %.[61, 62] If the oxygen partial pressure on the two sides of an OTM is different, an oxygen flux is started to compensate this difference (see Figure 1.1). It can be seen from Figure 1.1 that the permeation process from the high oxygen partial pressure side to the low oxygen partial pressure side involves three progressive steps: (1) the conversion of oxygen molecules to oxygen ions at the surface of the membrane on air side, (2) the simultaneous bulk diffusion of oxygen ion and electron – or in the Kroeger Vink notation – the diffusion of oxygen lattice vacancies/electron holes in the bulk phase, and (3) the reformation of oxygen molecules after passing through the membrane on the permeate side.[44, 63] The first and third steps are usually called surface exchange steps and the second step is called bulk diffusion step. Oxygen permeation through an OTM can be limited by bulk diffusion

limitation, the surface exchange resistance, or both. The slowest step is expected to limit the overall oxygen permeation rate. It should be noted that the bulk diffusion will be the rate-limiting step rat when the thickness of the membrane is relatively thick. In the case that the oxygen ion bulk diffusion is the rate-limiting, the oxygen permeation rate through an OTM can be expressed by the Wagner equation (see Eq. 1.3).[64, 65]
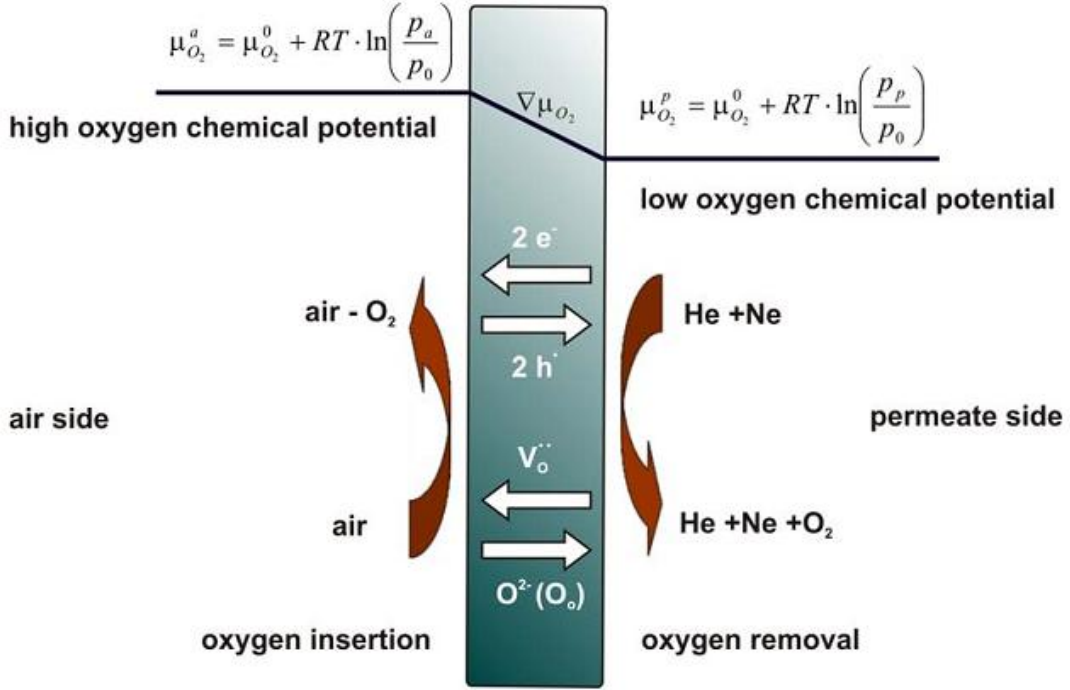
Figure 1.1 Schematic diagram of oxygen transport through a perovskite membrane.[66]

The molecular oxygen flux through a perovskite OTM is related to the chemical potential gradient $\nabla\mu(O_2)$

$$J_{O_2} = -\frac{1}{4(z_0 F)^2} \cdot \frac{\sigma_O \cdot (\sigma_h + \sigma_e)}{\sigma_O + (\sigma_h + \sigma_e)} \cdot \nabla\mu(O_2)$$

(Eq. 1.1)

F is Faraday constant, σ_O, σ_e and σ_h denote the partial conductivities of oxygen ions, electrons, and electron holes, respectively. The chemical potential gradient can be expressed by the derivative of the chemical activity of molecular oxygen

$$\nabla\mu(O_2) = RT \cdot \frac{\partial \ln a(O_2)}{\partial x}$$

(Eq. 1.2)

where R and T denote the gas constant and temperature, respectively. Assuming that both surfaces are in chemical equilibrium with the adjacent gas phases, the surface

oxygen activities can be expressed by the oxygen partial pressures. For the oxygen flux through a membrane of thickness L with the oxygen partial pressures $P_{O_2}^{'}$ and $P_{O_2}^{''}$ one obtains

$$J_{O_2} = -\frac{RT}{4^2 F^2 L} \cdot \int_{\ln P_{O_2}^{'}}^{\ln P_{O_2}^{''}} \frac{\sigma_O \cdot \sigma_{el}}{\sigma_O + \sigma_{el}} \, d\ln P_{O_2}$$

(Eq. 1.3)

with summarizing the partial conductivities σ_h and σ_e of the electrons and electron holes as electronic partial conductivity σ_{el}. Assuming that the oxygen ion migration governs the bulk transport ($\sigma_{el} \gg \sigma_o$) and the ionic conductivity σ_O depends in an exponential way - as it is often experimentally observed − on the oxygen partial pressure following the power law $\sigma_O = \sigma_O^0 \cdot (P_{O_2})^n$, the integration of Eq. 1.3 gives

$$J_{O_2} = -\frac{RT}{4^2 F^2 L} \frac{\sigma_O^0}{n} ((P_{O_2}^{'})^n - (P_{O_2}^{''})^n)$$

(Eq. 1.4)

For details see. [67]

However, if the walls of the OTM become sufficiently thin, the rate of surface processes (exchange of oxygen with the bulk OTM) gain influence. A characteristic membrane thickness L_c can be introduced for which the rate of the surface exchange is comparable to the rate of the diffusion-controlled oxygen ion transport through the membrane.[63, 68] Depending on the perovskite material under study and on the temperature (note that surface exchange and bulk diffusion have different activation energies) L_c can be of the order of 0.01-10 mm. That is to say that for membranes thinner than L_c there is no linear relationship between the oxygen flux J_{O2} and the reciprocal membrane thickness L^{-1} predicted by the Wagner equation in its usual form for bulk diffusion-controlled oxygen transport through an OTM of thickness L.[63]. Consequently, extremely thin supported perovskite layers often do not show the expected high oxygen flux since the surface exchange reaction becomes rate limiting rather than the oxygen bulk diffusion.

However, for mixed oxygen ion − electron conducting materials the surface processes can become rate limiting for oxygen transport through the membrane rather than bulk diffusion. Under surface reaction we understand the incorporation of oxygen

into the lattice (adsorption, dissociation, ionization, incorporation on a lattice vacancy) and vice versa on the permeate side. For BCFZ perovskite hollow fiber membrane with 170 µm wall thickness we found that the main transport mechanism is bulk diffusion with a contribution of the surface reaction.[69] From the value of n of Eq. 1.4 the rate-limiting step of the oxygen permeation can be identified.[70, 71] For negative values of n, the oxygen permeation is dominated by the bulk diffusion, while for $n \geq 0.5$ the exchange processes at the membrane surfaces can be assumed as rate-limiting. In the case of the surface exchange as rate-limiting step, a catalytic coating of the membrane can accelerate the oxygen flux. In the Surface Exchange Current Model,[72] J_{O2} gives a linear relationship with $(P_{O_2}^{''} / P_{O_2})^{0.5} - (P_{O_2}^{'} / P_{O_2})^{0.5}$ if oxygen transport is controlled by the surface exchange reaction. In the case of bulk diffusion control, J_{O2} is a linear function of $\ln(P_{O_2}^{''} / P_{O_2}^{'})$. However, a reliable way to determine the relative contributions of the surface processes and the oxygen bulk diffusion to the oxygen transport is the preparation of discs of different thickness. However, this way is time consuming it is and experimentally extremely difficult to prepare membranes thinner than 0.5 mm but the interesting critical thickness, where the change between bulk diffusion and surface exchange takes place, is often found to be around a few hundreds µm.

1.4 Structures of oxygen transporting materials

The most OTM materials presently studied are of perovskite type structure (ABO_3), also fluorite (AO_2),[73] Brownmillerite ($A_2B_2O_5$),[74] and pyrochlore ($A_2B_2O_7$)[75] structures are evaluated, since the latter two show oxygen transport already in the undoped formulation.[76] Among these OTM materials, perovskite-type membranes are the most studied materials for oxygen separation from air, since it shows high oxygen permeation rates at high temperatures. Perovskite-type oxides of the composition ABO_3 can host different cations on the A- and B-sites, where A-cation is occupied the large cation (mostly alkaline, alkaline-earth or rare-earth cation) and B-cation is smaller cation (mostly transition metals). The perovksite structure can form by a combination of ions in different valence state such as $A^{1+}B^{5+}O_3$, $A^{2+}B^{4+}O_3$, or $A^{3+}B^{3+}O_3$. The different A-site cation and B-site cation result in different lattice structures. A good benchmark

for the calculation of the lattice structure is the tolerance factor t described by Goldschmidt.[77]

$$t = \frac{r_A + r_O}{\sqrt{2}(r_B + r_O)}$$

(Eq. 1.5)

where r_A, r_B, and r_O are the ionic radii of the A-site metal ion, the B-site cation, and the oxygen ion (1.40 Å), respectively. The cubic perovskite structure can be maintained in the case of $0.75 \leq t \leq 1.0$ ($t = 1.0$ is ideal cubic perovskite structure).[78] When the tolerance factor is $t > 1.0$, a hexagonal structure tends to form. Furthermore, a perovskite-type oxide with cubic structure usually exhibits a higher oxygen permeability than those with other structures such as hexagonal, rhombohedral, or fluorite structures. The ideal cubic perovskite structure as shown in Figure 1.2, it is clearly to visualize the A cation in 12-fold oxygen coordination and the B-cation in 6-fold oxygen coordination, since the A cations occupy every hole which is created by 8 BO_6 octahedra. The BO_6 octahedra in the structure share corners infinitely in all 3 dimensions. In the ideal cubic perovskite structure, the B-O distance is equal to a/2 (a denotes the cubic unit cell parameter) while the A-O distance is $a/\sqrt{2}$.

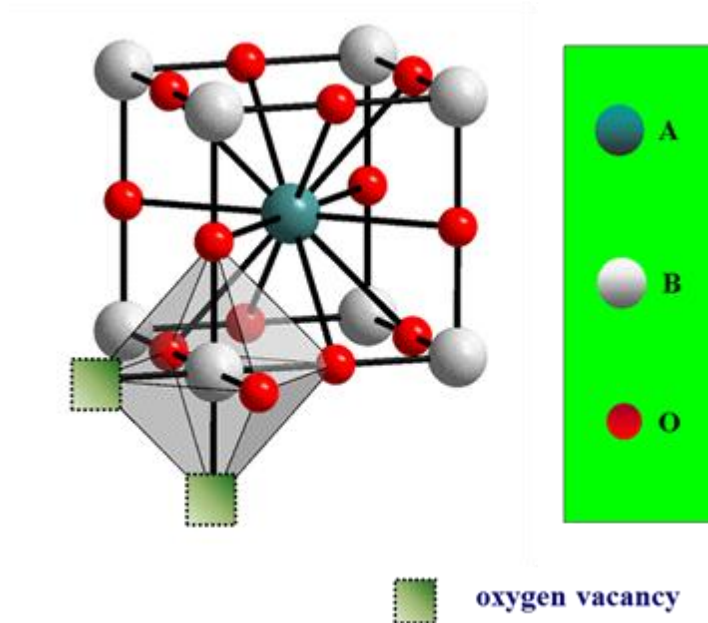

Figure 1.2 ABO_3 ideal perovskite structure showing oxygen octahedron containing the B ion linked through corners to form a tridimensional cubic lattice.[79]

To improve the oxygen permeability or the stability of OTM, the doping method

can be used to tailor the physical properties of the oxygen transporting materials through formation of non-integral stoichiometry phases or solid solutions by homogeneous doping with appropriate elements. ZrO_2 is the early and most successful example for stabilizing the oxide containing flexible redoxable cations such Co or other rare-earth oxides such as Y_2O_3. The improvement of the stability of the perovskite structure by introducing Zr on the B-site was reported by several authors.[43, 80, 81] Tong et al. investigated the Zr doped OTM materials of $BaCo_{0.4}Fe_{0.6-x}Zr_xO_{3-\delta}$, that shows a stable and ideal perovskite structure.[43] Yakovlev et al. recommended e.g. to stabilize $Ba_{0.5}Sr_{0.5}Co_{0.8}Fe_{0.2}O_{3-\delta}$ (BSCF) by bringing Zr on the B position.[81]

High oxygen conductivity of OTM depends on the structure type, the specific free volume of the lattice structure, and the oxygen vacancy concentration, those can be adjusted by the doping method. Improving the oxygen vacancy concentration of OMT can be doped with the easy redoxable cations, such as Co, Cu, or the cations with low valence, such as Al, Y, La, Ce. To satisfy the requirement of electrical neutrality, if higher valence cations are being added instead of lower valence cations, oxygen vacancy might be formed. The concentration of oxygen vacancy is a function of temperature and pressure of their components. Usually, OTM with cubic structure exhibits high oxygen permeability since it is isotropic structure with the homogeneous distribution of oxygen vacancy. The most OMT are mostly based on $BaFeO_{3-\delta}$ oxides. However, $BaFeO_{3-\delta}$ shows a low oxygen permeability and crystallizes in a hexagonal structure because of the ionic radius of Ba^{2+} which is too large to stabilize a cubic perovskite structure. The cubic perovskite structure of $BaFeO_{3-\delta}$ can be stabilized by (i) the partial substitution of the A-site with smaller cations, such as Sr, Ca, La, and Y,[47, 51] (ii) the partial substitution of the B-site with larger cations, such as Y, Cu, Ni, and Zr,[50, 82, 83] (iii) the partial substitution of both A- and B-sites by e.g. Y.[84] The partial substitution of the A-site with smaller cations can lead to a stabilization of the cubic perovskite structure. However, the volume of the cubic unit cell will be reduced which – in turn – reduces the oxygen flux. On the other hand, the partial substitution of the B-site with larger low-valency cations can result not only in the stabilization of the cubic perovskite structure, but can also increase the volume of the cubic unit cell and the oxygen vacancy concentration which are beneficial to the oxygen permeation.[6]

1.5   Preparation of OTM

1.5.1 Preparation of single phase OTM

The oxygen transporting materials can be prepared by numerous methods, such as solid state reaction, EDTA-citric acid sol-gel methods, chemical vapor deposition, coprecipitation, spray pyrolysis, hydrothermal synthesis, and combustion synthesis. The chemical and physical properties an OTM can affect by different preparation method which result in significantly microstructures such as grain size and density of membranes. In this thesis, four OTMs with different geometries (i.e. $Ba_{0.5}Sr_{0.5}Co_{0.8}Fe_{0.2}O_{3-\delta}$ (BSCF) dead-end tube membrane, $BaCo_xFe_yZr_{1-x-y}O_{3-\delta}$ (BCFZ) hollow fiber membranes, $BaFe_{0.95-x}La_xZr_{0.05}O_{3-\delta}$ (BFLZ) disc membrane and $40Pr_{0.6}Sr_{0.4}FeO_{3-\delta}$ - 60 $Ce_{0.9}Pr_{0.1}O_{2-\delta}$ (40PSFO-60CPO) dual phase disc membrane) were prepared by different methods.

a)   Conventional solid state reaction method of BSCF

Figure 1.3 Dead-end BSCF tube membrane with an outer diameter of 1 cm and 1 mm wall thickness as produced by the Fraunhofer Institute IKTS Dresden/Hermsdorf (Germany).

Among the above methods, the conventional solid state reaction method is the most widely used method for preparation of the perovskite-type oxide powders. The dead-end BSCF tubes (see Figure 1.3) were produced by the Fraunhofer Institute IKTS Dresden/Hermsdorf (Germany).[85] The powder of the BSCF was successfully prepared

by the conventional solid state reaction process, with $BaCO_3$, $SrCO_3$, Fe_2O_3, and Co_3O_4 as the raw materials. The components were weight in stoichiometric amount, milled together for a few hours and calcined at 1000 °C for 2h. The calcined powders were uniaxially pressed into pellets and sintered under ambient pressure in air to become gas-tight membrane discs with 10 mm in diameter and 1.0 mm in thickness. The BSCF tube membranes with an outer diameter of 10 mm, an inner diameter of 8 mm, and a length of 400 mm were manufactured by a phase inversion spinning followed by sintering. Then, One end of a BSCF tube and one side of a 1 mm thick BSCF disk were grinded to make a flat and even surface. A paste based on copper oxide used as sintering aid was screen printed on both surfaces. The screen printed areas were contacted and the tube - standing vertical on the plate -   was loaded with a weight of 300 g to support the joining which was carried out by a reaction-diffusion sintering at 980 °C with a dwell time of two hours as described recently.[86]

b) Preparation of perovskite BCFZ hollow fiber membrane
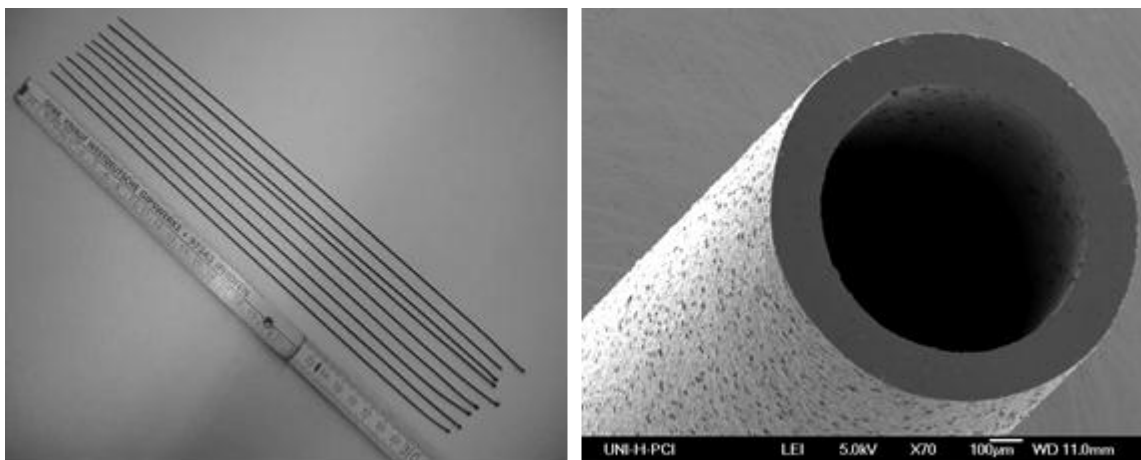
Figure 1.4 The sintered BCFZ hollow fiber membrane (SEM provided by Prof. Dr. A. Feldhoff).

Dense BCFZ perovskite hollow fiber membranes were manufactured at the Fraunhofer Institute for Interfacial Engineering and Biotechnology (IGB) in Stuttgart by a phase inversion spinning process followed by high-temperature sintering at 1320 °C.[87] A simple hydrolysis of the corresponding metal nitrates by an ammonium hydroxide solution was applied to get the precursor BCFZ material. The precursor was mixed with

a solution of polysulfone in 1-methyl-2-pyrrolidone and was ball-milled up to 24 h with a solid content of 50 - 60 mass %. The slurry was spun through a spinneret and the obtained infinite green hollow fiber was cut into 0.5 m long pieces before sintering the fiber in a hanging geometry. After sintering at 1300 °C for 5 h, as shown in Figure 1.6, the length of the green fiber reduced from 50 cm to ~ 32 cm and the sintered fiber had a wall thickness of around 0.17 mm with an outer diameter of 1.10 mm and an inner diameter of 0.76 mm, as shown in Figure 1.4.

c) The EDTA-citric acid sol-gel synthesis of perovskite BFLZ
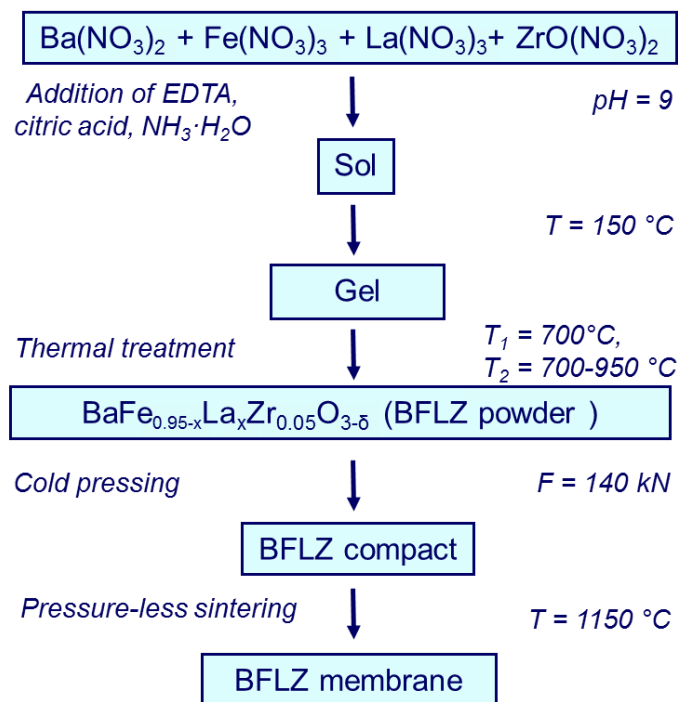
Figure 1.5 Flow chart of preparation of BFLZ powder with the EDTA-citric acid sol-gel method.

The EDTA-citric acid sol-gel method exhibits a better mixing of the starting materials and excellent chemical homogeneity in the final product since it offers control at molecular level.[88, 89] BFLZ powders were prepared by this EDTA-citric acid sol-gel method, as shown in Figure 1.5, The calculated amounts of $Ba(NO_3)_2$, $Fe(NO_3)_3$, $ZrO(NO_3)_2$ and $La(NO_3)_3$ in their appropriate stoichiometric ratios were dissolved in an aqueous solution, followed by the addition of EDTA and citric acid with the molar ratios of EDTA/citric acid/metal cations = 1:1.5:1. The pH value of the solution was adjusted

to around 9 by adding NH_4OH. The solution was then heated in the temperature range of 120 - 150 °C under constant stirring to obtain a dark gel. After the dark gel was burnt in a heating mantle, the obtained product was treated at 950 °C for 10 h to obtain BFLZ perovskite powder. The calcined powders were uniaxially pressed into pellets under 150 kN and sintered under ambient pressure at 1200 °C for 10 h in air to become gas-tight membrane discs with 14 mm in diameter and 1.1 mm in thickness.

1.5.2 Preparation of dual phase oxygen permeable membranes
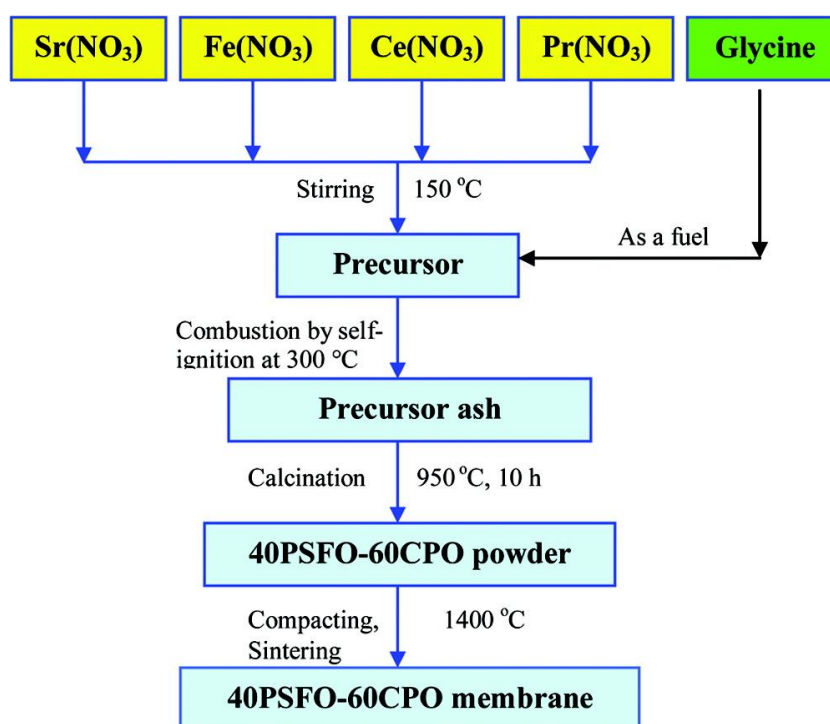
Figure 1.6 Flow chart for the one-pot one-step preparation of dual phase 40PSFO-60CPO membranes by the glycine-nitrate combustion process.[90]

Dual phase oxygen transporting powders can be prepared by a range of methods, such as in a simple mixing of the two oxide powders, packing method, loading method, and one-pot single-step method.[91] To achieve the high oxygen permeability of the dual phase membrane, the dual phase powder should have a small particle size and a low degree of agglomeration. The simple mixing of the two oxide powders method as the traditional synthesized method often requires several steps and gives the powder with a coarse agglomeration.[92] one-pot single-step methods shows a simple synthetic process and gives fine and homogeneous powders. One-pot single-step methods include the

one-pot single-step EDTA-citric acid process[58] and the one-pot single-step glycine-nitrate combustion process (GNP).[93] In this thesis, 40PSFO-60CPO dual phase membrane was perparaed by the one-pot single-step GNP.[90] Here, GNP is used to rapidly produce complex oxide ceramic powders of uniform composition on an atomic scale and fine enough to for sinter to a high density. The process flow chart is shown in Figure 1.6. A precursor was prepared by combining glycine and the metal nitrates $Sr(NO_3)_2$, $Fe(NO_3)_3$, $Ce(NO_3)_3$ and $Pr(NO_3)_3$ in their appropriate stoichiometric ratios in an aqueous solution. The molar ratio of glycine : total metal ions was 2 : 1. The precursor was stirred and heated at 150 °C in air to evaporate excess water until a viscous liquid was obtained. Further heating of the viscous liquid up to 300 °C caused the precursor liquid to auto-ignite. Combustion was rapid and self-sustaining, and a precursor ash was obtained. For comparison, the single phase $Pr_{0.6}Sr_{0.4}FeO_{3-\delta}$ (PSFO) and $Ce_{0.9}Pr_{0.1}O_{2-\delta}$ (CPO) materials were also prepared via the GNP method. All the powders were calcined at 950 °C in air for 10 h. The 40PSFO-60CPO powders were pressed to disk membranes under a pressure of 5 MPa in a stainless steel module with a diameter of 18 mm to get green disk membranes. These green disks were sintered at 1400 °C in air for 5 h.

1.6 Applications of OTM

1.6.1 Oxygen production in membrane separator

Oxygen-transporting membranes (OTMs) can separate oxygen from air, which is a gas mixture containing approximately 78 vol.% N_2 and 21 vol.% O_2,[8] or from other oxygen-containing gases. OTMs can theoretically produce oxygen at purities of up to 100 % and are believed to possess the potential to reduce the cost of high-purity oxygen production compared to the conventional cryogenic processes.[9] Moreover, OTM reactors have been developed for such potential applications as the partial oxidation of hydrocarbons,[10-13] the production of hydrogen by thermal water splitting in combination with olefin and synthesis gas production,[14-16] and the decomposition of nitrogen oxides.[17, 18]

Oxygen can be separated from air as the cheapest source of oxygen, if the oxygen

partial pressure on the feed side of the OTM is higher than that on the permeate side. This difference in the oxygen partial pressures can be achieved (i) by using sweep gases like steam, which can be easily separated from the permeated oxygen by condensation,[94] (ii) by using vacuum pumps to drain off the permeated oxygen, (iii) by pressurized air on the feed side of the OTM having pure oxygen on the permeate side at atmospheric pressure,[95] or (iv) by combining of the pumping on the permeated side and having pressurized air on the feed side.[31, 96, 97]
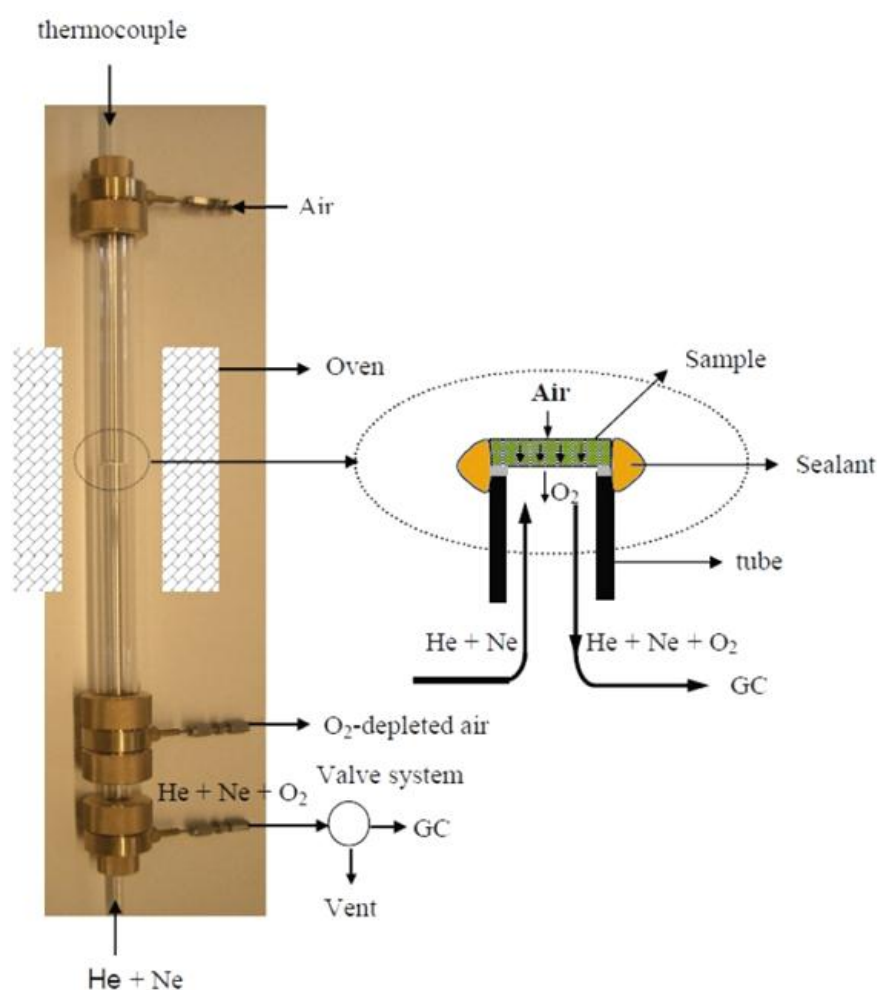
Figure 1.7 Schematic equipment for oxygen permeation in this work.[98]

So far, mainly relative thick disk-shaped membranes with a limited membrane area were studied because disks can be easily fabricated by a conventional pressing method. Although a multiple planar stack can be adopted to enlarge the membrane area to an industry-relevant scale, many problems, such as the high-temperature sealing and the pressure resistance, have to be faced.[99] Tubular membranes with diameters in the

centimeter range with thick walls were developed to reduce the engineering difficulties, especially the problems associated with the high-temperature sealing.[100] Oxygen permeation by using disc membrane in this thesis was studied in a home-made high-temperature oxygen permeation device, as shown in Figure 1.7. The disc membranes were sealed onto an alumina tube with a gold paste (Heraeus, Germany) at 950 $^{\circ}$C for 5 h. The feed side was fed with synthetic air (20 vol.% O_2 / 80 vol.% N_2), whereas Ne (99.995%) and He (99.995%) were fed to the sweep side. All gas flows were controlled by mass flow controllers (Bronkhorst, Germany) and all flow rates were regularly calibrated by using a bubble flow meter. The concentrations of the gases at the exit of the reactor were analyzed by an on-line gas chromatograph (Agilent 7890A) with a Molsieve 5A column. The total flow rate of the effluents on the permeate side was calculated by using Ne as an internal standard. The total O_2 leakage was calculated and subtracted from the total O_2 flux after the N_2 concentration was measured. It is assumed that the leaking of nitrogen and oxygen is in accordance with a Knudsen diffusion mechanism. The fluxes of leaked nitrogen and oxygen are related by Eq. 1.6.

$$D_k = J_{N_2}^{Leak} : J_{O_2}^{Leak} = \sqrt{\frac{32}{28}} \times \frac{C_{N_2}}{C_{O_2}}$$

(Eq. 1.6)

where D_k is the Knudsen diffusion factor, C_{O_2}, and C_{N_2} are the oxygen and nitrogen concentrations in the feed gas, respectively.

The oxygen permeation flux J_{O2} (cm^3 (STP) min^{-1} cm^{-2}) was then calculated by Eq. 1.7.

$$J_{O_2} = (C_{O_2} - \frac{C_{N_2}}{D_k}) \times \frac{F}{S}$$

(Eq. 1.7)

Here, C_{O_2}, and C_{N_2} are the oxygen and nitrogen concentrations determined by a calibrated gas chromatograph. F is the total flow rate at the outlet on the permeate/core side, and S is the effective surface for permeation.

The oxygen recovery has been calculated by

$$O_{2,recovery} = \frac{F_{O_2}}{F_{air,inlet} \cdot C_{O_2}}$$

(Eq. 1.8)

with F_{O2} as oxygen permeation flow rate, C_{O_2} the oxygen concentration in vol.% and $F_{air,inlet}$ as air flow rate at the inlet of the feed/shell side.

Tubular membranes were developed to reduce the engineering difficulties, especially the problem of the high temperature sealing. Moreover, the surface area of a tubular membrane can be produces lager than that of disc membrane and gives good mechanic stability. However, their small surface area to volume ratio and their relatively thick walls lead to a low oxygen flux and make them unfavorable in practice. In this thesis, A BSCF dead-end membrane was used for oxygen production in a dead-end membrane permeator as shown in Figure 1.8.[31, 36] A stream of air, as a nitrogen/oxygen mixture, is supplied from the left to the dead end of the tube and leaves the setup as oxygen-depleted air. Oxygen permeates the MIEC tube walls via a flux of oxygen anions, which is accompanied by counter flowing electrons. Permeated oxygen leaves the setup to the right via the interior of the tube to the right. In the experiment, parts of the tube membrane were coated by a gold paste (Heraeus), except the 3 cm part near the dead end. The tube segment was painted by the Au paste, which then was sintered at 950 °C for 5 h. This procedure was applied threefold to obtain a dense gold film, which the oxygen cannot permeate. Inspection by light microscope of the gold sealing after long-term permeation experiment revealed a still hole- and crack-free dense layer. This is consistent with the good compatibility of gold sealant with perovskite membrane as reported by Tong et al.[35] for 2000 h long high-temperature experiments. The uncoated part of our tube with an effective membrane area of 9.1 cm^2 for the outer membrane surface was placed in the middle of the oven, thus ensuring isothermal conditions. Oxygen-enriched air with 50 vol.% O_2 at an elevated pressure of 5 bar was fed at a rate of 500 cm^3(STP)min^{-1} to the feed side. Flow rates were controlled by gas mass-flow controllers (Bronkhorst). High-purity oxygen was produced at approximately 0.1 bar on the core/permeate side. This reduced pressure was achieved with a vacuum pump (Pfeiffer vacuum MVP 015-4). The flow of the outlet on the core/permeate side was mixed with neon (1.0 cm^3(STP)min^{-1}, 99.995%) as an internal standardization gas, which allowed the determination of the absolute flux of the permeate gas by an on-line coupled gas chromatograph (Agilent 7890A) that was equipped with a Carboxen 1000 column.
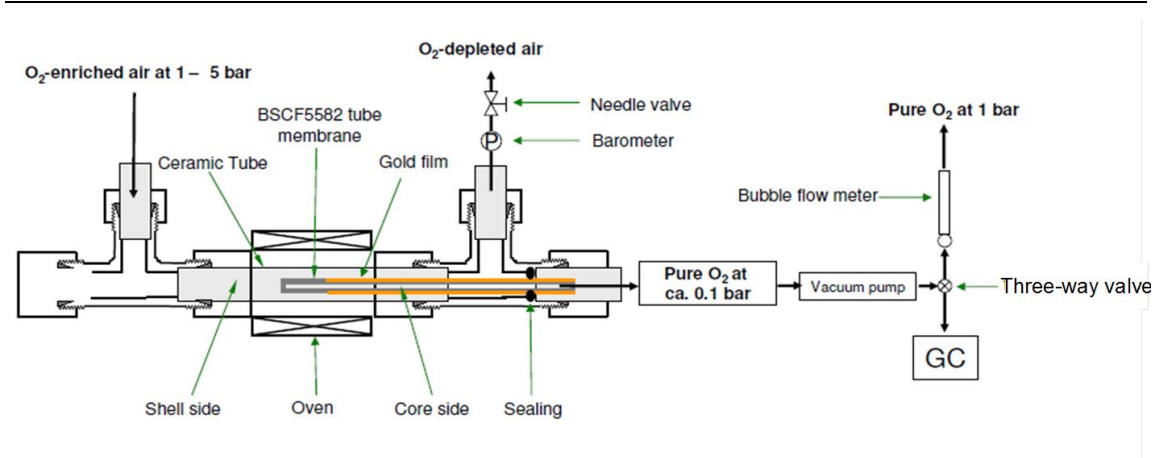
Figure 1.8 Permeator 2 in dead-end geometry for the production of pure O_2.

Compared to the disk and tubular membranes, hollow fiber membranes possess much larger membrane area per unit volume for oxygen permeation.[101] By keeping the two sealed ends outside the high temperature zone, polymer O-rings can be used. Furthermore, the resistance of the hollow-fiber membrane as a full material (i.e. non-supported) to oxygen permeation is very much reduced due to the thin wall as it is the case for supported thin perovskite films. Due to the thin wall, the materials costs of the hollow fiber membrane are reduced.
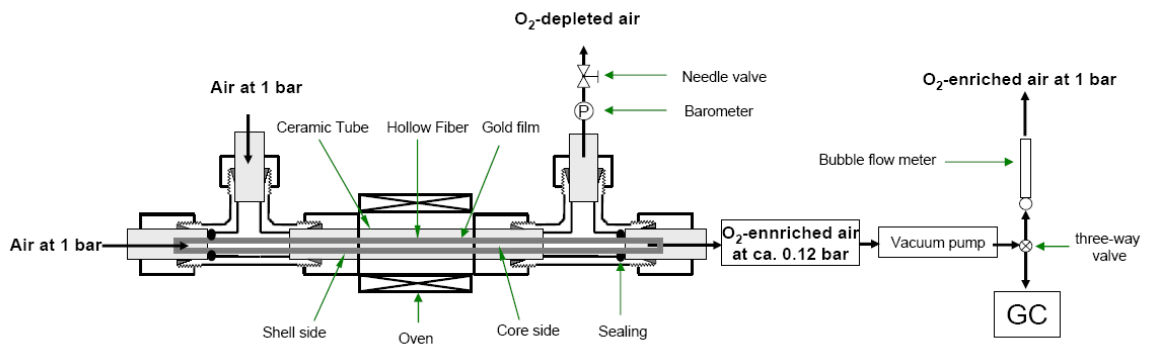
Figure 1.9 Permeator 1 in flow-through geometry for the production of O_2–enriched air.[96]

A hollow fiber membrane with the composition of BCFZ was used for the production of O_2-enriched air and of high-purity oxygen in a in a flow-through permeator and a dead-end membrane permeator, as shown in Figure 1.9 and Figure 1.10.[96] Figure 1.9 shows schematically the flow-through membrane permeators 1 used for the production of O_2-enriched air. The fibers used here had a length of 30 cm. The two ends of the BCFZ hollow fiber membrane were sealed by two silicone rubber rings outside the oven.

Synthetic air (O_2 concentration 20 vol.%) was fed to the shell side and another flow of synthetic air was sent through the core side at different flow rates (25-75 $cm^3 \, min^{-1}$). The reduced pressure on the core/permeate side of the hollow fiber membrane was kept at about 0.12 bar by connection to an oil-free diaphragm vacuum pump (Pfeiffer vacuum MVP 015-4). Due to the difference in the oxygen partial pressure between shell and core side, oxygen from the shell side permeates through the hollow fiber membrane to the core side and mixes there with air, thus forming O_2-enriched air.
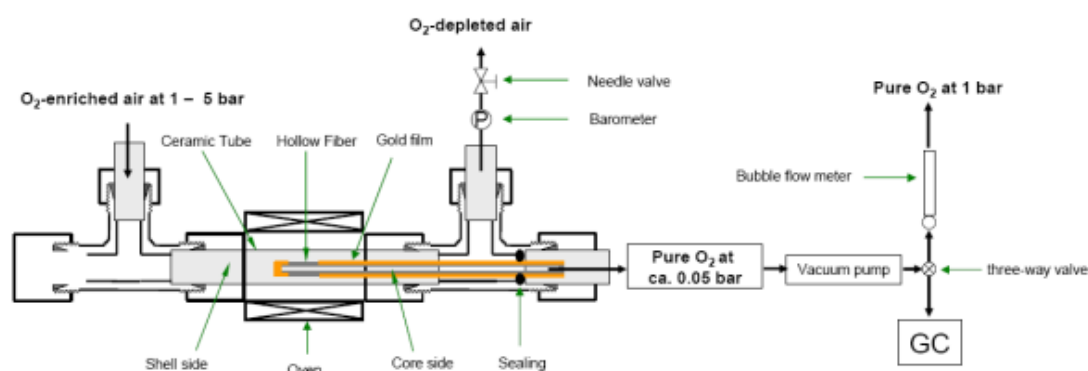

Figure 1.10 Permeator 2 in dead-end geometry for the production of pure O_2.[96]

Figure 1.10 presents the dead-end membrane permeator 2 used for the production of pure oxygen. The dead-end hollow fiber membrane is obtained by sealing one end of the BCFZ hollow fiber with a gold plug using Au paste (Hereaus, sintering the gold paste at 950 ^{o}C to make it gastight). The dead-end BCFZ hollow fiber was coated by dense gold film except the 3-cm part close to the end with gold-plug. The uncoated part (3 cm, effective membrane area: 0.86 cm^2) of the hollow fiber was put in the middle of the oven thus ensuring isothermal conditions. Synthetic air or oxygen enriched air at atmospheric or elevated pressures (1 – 5 bar) were fed to the shell/feed side. On the core side, high-purity oxygen was produced at about 0.05 bar. This reduced pressure on the core side was achieved with a vacuum pump (Pfeiffer vacuum MVP 015-4).

In recent years, many perovskite hollow fiber membranes have been successfully prepared by a phase-inversion/sintering process [87, 101-103]. Compared to other configurations such as planar or tubular membranes, the hollow fiber membranes can provide a much larger area per unit volume. Thus it is possible to reduce the membrane system size remarkably. Furthermore, the hollow fiber OTM can solve the problem of

the high-temperature sealing in fabricating membrane modules.[104] Recently, Tan et al.[105] investigated the pilot-scale production of oxygen from air using perovskite $La_{0.6}Sr_{0.4}Co_{0.2}Fe_{0.8}O_{3-\delta}$ hollow fiber membranes. The separation performances, stability, scaling up effect and the energy consumption of an OTM system prepared 889 one dead-end hollow fiber have been investigated both theoretically and experimentally. 3.1 L (STP) min^{-1} oxygen with the purity of 99.9 % was obtained in the OTM system at 1070 °C.

1.6.2 Partial oxidation of methane (POM) to synthesis gas

Synthesis gas ($CO + H_2$) is required for wide industrial processes, such as methanol or Fischer-Tropsch synthesis. Syngas can be produced by several ways e.g. by the catalytic partial oxidation (POM) (see Eq. 1.9) or the classical catalyticsteam reforming (SR) (see Eq. 1.10).

$$CH_4 + 1/2O_2 \rightleftarrows CO + 2H_2 \qquad \Delta_R H^0 = -38\,kJ/mol \qquad \text{(Eq.1.9)}$$

$$CH_4 + H_2O \rightleftarrows CO + 3H_2 \qquad \Delta_R H^0 = -206\,kJ/mol \qquad \text{(Eq. 1.10)}$$
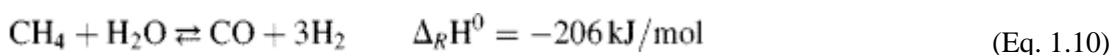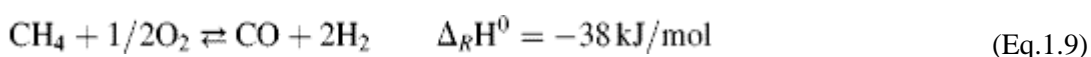
Compared with the recently main technology SR, the POM using OTM reactor to product synthesis gas has several potential advantages. Syngas production costs can be potentially reduced by integration the oxygen separation and POM in a membrane reactor. Furthermore, only the oxygen from air can be transported through the membrane to the reaction side, where it reacts with the methane to N_2-free syngas, the downstream requirements cannot tolerate the presence of N_2. Moreover, compared to steam reforming, a great advantage of the POM is a lower H_2/CO ratio of 2 (instead of 3), which is optimum for methanol synthesis or the Fischer-Tropsch process.

A number of single phase cobalt-containing perovskite-type membranes with a high oxygen permeation rate were reported to be successfully used in POM to synthesis gas.[7, 10, 106-108] However, these cobalt-containing perovskite membranes exhibit poor phase stability under a reducing environment. To improve the membrane stability, several concepts are being followed such as (i) reducing the relative amount of cobalt in the perovskite and co-doping the material with less-reducible metals such as Zr^{4+}, Ga^{3+} or Ta^{3+},[13, 109, 110] (ii) developing new oxygen transporting materials such as cobalt-free

OTM and dual phase OTM. Tong et al.[109] reported that syngas production in a membrane reactor made of $BaCo_{0.4}Fe_{0.4}Zr_{0.2}O_{3-\delta}$ can be operated steadily for more than 2200 h at 850 ^{o}C. Zhu et al.[107] developed a membrane reactor made of a cobalt-free $Ba_{0.15}Ce_{0.85}FeO_{3-\delta}$ material to produce syngas from methane. However, after operation for 140 h at 850 °C, the used membrane was obtained the decomposition of the membrane materials under such conditions. Dual phase membranes have been suggested as good substitutes with compositions that can be adjusted according to the practical requirements. Recently, many dual phase membranes were developed to the POM reaction. Zhu et al. studied a disk-type dual phase membrane reactors based on wt. % $Sm_{0.15}Ce_{0.85}O_{1.925}$ - 25 wt. % $Sm_{0.6}Sr_{0.4}Fe_{1-x}Al_xO_{3-\delta}$ (x = 0 or 0.3) for the syngas production by POM. They reported that these dual phase reactors can be steadily in the POM to syngas generation for more than 1100 h at 950 °C.[111, 112]

1.6.3 Coupling of reactions in an OTM reactor
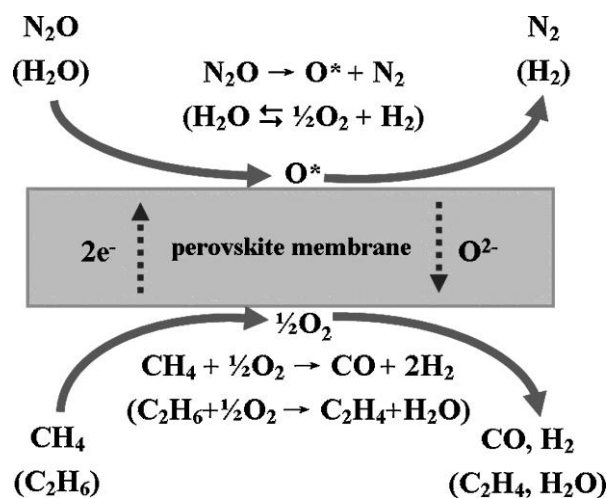
Figure 1.11 Concept of water splitting and N_2O decomposition in an OTM reactor.[113]

One of the major advantages of OTM reactors is that two reactions can be coupled in one membrane reactor; the products will be kept separated on the two sides of the membrane and a subsequent procedure is not necessary to separate the products. If an OTM is used to remove O_2 as it is generated, the conversion of a reaction can be increased. Recently, our group successfully used the single phase perovskite-type BCFZ hollow fiber membrane in the equilibrium-limited water splitting and the kinetically

controlled N_2O decomposition with the coupling POM or the oxidative coupling of methane (OCM),[14-18, 113] as shown in Figure 1.11.

Hydrogen is attracting more and more attention because it is recommend an alternative source to fossil fuels to solve the worldwide energy demands and global climate change. And water is the ideal source for the generation of large amounts of hydrogen. However, the equilibrium constant of water dissociation is very small even at a relatively high temperature. If the equilibrium-limited water splitting and POM were coupled in an OTM reactor, a high H_2 production flux of 3.1 ml/min·cm^2 was obtained at 950 ^{o}C.[113]

N_2O has recently received much attention because it is a greenhouse gas with 310 times greenhouse effect than CO_2. However, the catalytic decomposition of nitrous oxide (N_2O)[114-117] over perovskite catalysts, most of the catalysts cannot tolerate the co-existence of O_2 because adsorbed oxygen blocks the catalytically active sites for the N_2O decomposition.[117] If an OTM is used to remove the inhibitor oxygen from the N_2O side with coupling POM, the total decomposition of N_2O can be obtained in a OTM reactor.[17, 113]

1.7 **Bibliography**

[1] Bose, A.C., Inorganic membranes for energy and environmental applications. *Springer*, New York, **2009**, p 4.

[2] Jasra, R.V.; Choudary, N.V.; Bhat, S.G.T. Separation of gases by pressure swing adsorption. *Sep. Sci. Technol.* **1991**, 26, 885-930.

[3] Matson, S.L.; Ward, W.J.; Kimura, S.G.; Browall, W.R. Membraneoxygenenrichment: II. Economicassessment. *J. Membr. Sci.* **1986**, 29, 79-96.

[4] Chen, C.S.; Feng, S.J.; Ran, S.; Zhu, D.C.; Liu, W.; Bouwmeester, H.J.M. Conversion of methane to syngas by a membrane-based oxidation-reforming process. *Angew. Chem. Int. Ed.* **2003**, 42, 5196-5198.

[5] Kharton, V.V.; Yaremchenko, A.A.; Kovalevsky, A.V.; Viskup, A.P.; Naumovich, E.N.; Kerko, P.F. Perovskite-type oxides for high-temperature oxygen separation membranes. *J. Membr. Sci.* **1999**, 163, 307-317.

[6] Liu, Y.Y.; Tan, X.Y.; Li, K. Mixed conducting ceramics for catalytic membrane processing. *Catal. Rev. Sci. Eng.* **2006**, 48, 145-198.

[7] Caro, J.; Caspary, K.J.; Hamel, C.; Hoting, B.; Kölsch, P.; Langanke, B.; Nassauer, K.; Schiestel, T.; Schmidt, A.; Schomaecker, R.; Seidel-Morgenstern, A.; Tsotsas, E.; Voigt, I.; Wang, H.; Warsitz, R.; Werth, S.; Wolf, A. Catalytic membrane reactors for partial oxidation using perovskite hollow fiber membranes and for partial hydrogenation using a catalytic membrane contactor. *Ind. Eng. Chem. Res.* **2007**, 46, 2286-2294.

[8] Lide, D.R., CRC handbook of chemistry and physics. *CRC Press*, Boca Raton, **1997**.

[9] Armstrong, P.A.; Bennet, D.L.; Fprster, E.P.T.; van Stein, E.E. *The gasification technology conference*, Washington DC, USA, **3-6 October 2004**.

[10] Bouwmeester, H.J.M. Dense ceramic membranes for methane conversion. *Catal. Today* **2003**, 82, 141-150.

[11] Tsai, C.Y.; Dixon, A.G.; Moser, W.R.; Ma, Y.H. Dense perovskite membrane reactors for partial oxidation of methane to syngas. *AIChE J.* **1997**, 43, 2741-2750.

[12] Shao, Z.P.; Dong, H.; Xiong, G.X.; Gong, Y.; Yang, W.S. Performance of a mixed-conducting ceramic membrane reactor with high oxygen permeability for methane conversion. *J. Membr. Sci.* **2001**, 183, 181-192.

[13] Yang, W.S.; Wang, H.H.; Zhu, X.F.; Lin, L.W. Development and application of oxygen permeable membrane in selective oxidation of light alkanes. *Top. Catal.* **2005**, 35, 155-167.

[14] Jiang, H.Q.; Cao, Z.W.; Schirrmeister, S.; Schiestel, T.; Caro, J. A coupling

strategy to produce hydrogen and ethylene in a membrane reactor. *Angew. Chem. Int. Ed.* **2010**, 49, 5656-5660.

[15] Jiang, H.Q.; Liang, F.Y.; Czuprat, O.; Efimov, K.; Feldhoff, A.; Schirrmeister, S.; Schiestel, T.; Wang, H.H.; Caro, J. Improvement of oxygen permeation for hydrogen production from water dissociation in surface-modified $BaCo_xFe_yZr_{1-x-y}O_{3-\delta}$ hollow fiber membrane. *Chem. Eur. J.* **2010**, 16, 7898-7903.

[16] Jiang, H.Q.; Wang, H.H.; Werth, S.; Schiestel, T.; Caro, J. Simultaneous production of hydrogen and synthesis gas by combining water splitting with partial oxidation of methane in a hollow-fiber membrane reactor. *Angew. Chem. Int. Ed.* **2008**, 47, 9341-9344.

[17] Jiang, H.Q.; Wang, H.H.; Liang, F.Y.; Werth, S.; Schiestel, T.; Caro, J. Direct decomposition of nitrous oxide to nitrogen by in situ oxygen removal with a perovskite membrane. *Angew. Chem. Int. Ed.* **2009**, 48, 2983-2986.

[18] Jiang, H.Q.; Xing, L.; Czuprat, O.; Wang, H.H.; Schirrmeister, S.; Schiestel, T.; Caro, J. Highly effective NO decomposition by in situ removal of inhibitor oxygen using an oxygen transporting membrane. *Chem. Commun.* **2009**, 6738-6740.

[19] Teraoka, Y.; Zhang, H.M.; Furukawa, S.; Yamazoe, N. Oxygen permeation through perovskite-type oxides. *Chem. Lett.* **1985**, 1743-1746.

[20] Teraoka, Y.; Nobunaga, T.; Yamazoe, N. Effect of cation substitution on the oxygen semipermeability of perovskite-type oxides. *Chem. Lett.* **1988**, 503-506.

[21] Shao, Z.P.; Yang, W.S.; Cong, Y.; Dong, H.; Tong, J.H.; Xiong, G.X. Investigation of the permeation behavior and stability of a $Ba_{0.5}Sr_{0.5}Co_{0.8}Fe_{0.2}O_{3-\delta}$ oxygen membrane. *J. Membr. Sci.* **2000**, 172, 177-188.

[22] Vente, J.F.; McIntosh, S.; Haije, W.G.; Bouwmeester, H.J.M. Properties and performance of $Ba_xSr_{1-x}Co_{0.8}Fe_{0.2}O_{3-delta}$ materials for oxygen transport membranes. *J. Solid State Electrochem.* **2006**, 10, 581-588.

[23] Qiu, L.; Lee, T.H.; Liu, L.M.; Yang, Y.L.; Jacobson, A.J. Oxygen permeation studies of $SrCo_{0.8}Fe_{0.2}O_{3-delta}$. *Solid State Ionics* **1995**, 76, 321-329.

[24] Bouwmeester, H.J.M.; Den Otter, M.W.; Boukamp, B.A. Oxygen transport in $La_{0.6}Sr_{0.4}Co_{1-y}Fe_yO_{3-delta}$. *J. Solid State Electrochem.* **2004**, 8, 599-605.

[25] Yang, L.; Wu, Z.T.; Jin, W.Q.; Xu, N.P. Structure and oxygen permeability of $BaCo_{0.4}Fe_{0.6-x}Zr_xO_{3-\delta}$ oxide: Effect of the synthesis method. *Ind. Eng. Chem. Res.* **2004**, 43, 2747-2752.

[26] Luo, H.X.; Tian, B.B.; Wei, Y.Y.; Wang, H.H.; Jiang, H.Q.; Caro, J. Oxygen permeability and structural stability of a novel tantalum-doped perovskite $BaCo_{0.7}Fe_{0.2}Ta_{0.1}O_{3-\delta}$. *AIChE J.* **2010**, 56, 604-610.

[27] Martynczuk, J.; Liang, F.Y.; Arnold, M.; Sepelak, V.; Feldhoff, A. Aluminum-Doped Perovskites As High-Performance Oxygen Permeation

Materials. *Chemistry of Materials* **2009**, 21, 1586-1594.

[28] Efimov, K.; Halfer, T.; Kuhn, A.; Heitjans, P.; Caro, J.; Feldhoff, A. Novel cobalt-free oxygen-permeable perovskite-type membrane. *Chem. Mater.* **2010**, 22, 1540-1544.

[29] Lu, H.; Tong, J.H.; Cong, Y.; Yang, W.S. Partial oxidation of methane in $Ba_{0.5}Sr_{0.5}Co_{0.8}Fe_{0.2}O_{3-delta}$ membrane reactor at high pressures. *Catal. Today* **2005**, 104, 154-159.

[30] Wang, H.H.; Tablet, C.; Feldhoff, A.; Caro, J. Investigation of phase structure, sintering, and permeability of perovskite-type $Ba_{0.5}Sr_{0.5}Co_{0.8}Fe_{0.2}O_{3-delta}$ membranes. *J. Membr. Sci.* **2005**, 262, 20-26.

[31] Liang, F.Y.; Jiang, H.Q.; Luo, H.X.; Kriegel, R.; Caro, J. High-purity oxygen production by a dead-end $Ba_{0.5}Sr_{0.5}Co_{0.8}Fe_{0.2}O_{3-delta}$ tube membrane. *Catal. Today* **2012**, 193, 95-100.

[32] Shao, Z.P.; Haile, S.M. A high-performance cathode for the next generation of solid-oxide fuel cells. *Nature* **2004**, 431, 170-173.

[33] Kriegel, R.; Kircheisen, R.; Töpfer, J. Oxygen stoichiometry and expansion behavior of $Ba_{0.5}Sr_{0.5}Co_{0.8}Fe_{0.2}O_{3-\delta}$. *Solid State Ionics* **2010**, 181, 64-70.

[34] Arnold, M.; Gesing, T.M.; Martynczuk, J.; Feldhoff, A. Correlation of the formation and the decomposition process of the BSCF perovskite at intermediate temperatures. *Chem. Mater.* **2008**, 20, 5851-5858.

[35] Efimov, K.; Xu, Q.A.; Feldhoff, A. Transmission electron microscopy study of $Ba_{0.5}Sr_{0.5}Co_{0.8}Fe_{0.2}O_{3-\delta}$ perovskite decomposition at intermediate temperatures. *Chem. Mater.* **2010**, 22, 5866-5875.

[36] Liang, F.Y.; Jiang, H.Q.; Luo, H.X.; Caro, J.; Feldhoff, A. Phase stability and permeation behavior of dead-end $Ba_{0.5}Sr_{0.5}Co_{0.8}Fe_{0.2}O_{3-\delta}$ tube membrane in high-purity oxygen production. *Chem. Mater.* **2011**, 23, 4765-4772.

[37] Mueller, D.N.; De Souza, R.A.; Weirich, T.E.; Roehrens, D.; Mayer, J.; Martin, M. A kinetic study of the decomposition of the cubic perovskite-type oxide $Ba_xSr_{1-x}Co_{0.8}Fe_{0.2}O_{3-delta}$ (BSCF) (x=0.1 and 0.5). *Phys. Chem. Chem. Phys.* **2010**, 12, 10320-10328.

[38] Švarcová, S.; Wiik, K.; Tolchard, J.; Bouwmeester, H.J.M.; Grande, T. Structural instability of cubic perovskite $Ba_xSr_xSr_{1-x}Co_{1-y}Fe_yO_{3-\delta}$. *Solid State Ionics* **2008**, 178, 1787-1791.

[39] van Veen, A.C.; Rebeilleau, M.; Farrusseng, D.; Mirodatos, C. Studies on the performance stability of mixed conducting BSCFO membranes in medium temperature oxygen permeation. *Chem. Commun.* **2003**, 32-33.

[40] Bux, H.; Liang, F.Y.; Li, Y.S.; Cravillon, J.; Wiebcke, M.; Caro, J. Zeolitic Imidazolate Framework Membrane with Molecular Sieving Properties by Microwave-Assisted Solvothermal Synthesis. *J. Am. Chem. Soc.* **2009**, 131,

16000-16001.

[41]   Luo, H.X.; Wei, Y.Y.; Jiang, H.Q.; Yuan, W.H.; Lv, Y.X.; Caro, J.; Wang, H.H. Performance of a ceramic membrane reactor with high oxygen flux Ta-containing perovskite for the partial oxidation of methane to syngas. *J. Membr. Sci.* **2010**, 350, 154-160.

[42]   Jiang, H.Q.; Wang, H.H.; Liang, F.Y.; Werth, S.; Schiestel, T.; Caro, J. Direct Decomposition of Nitrous Oxide to Nitrogen by In Situ Oxygen Removal with a Perovskite Membrane. *Angew. Chem. Int. Ed.* **2009**, 48, 2983-2986.

[43]   Tong, J.H.; Yang, W.S.; Zhu, B.C.; Cai, R. Investigation of ideal zirconium-doped perovskite-type ceramic membrane materials for oxygen separation. *J. Membr. Sci.* **2002**, 203, 175-189.

[44]   Liang, F.Y.; Caro, J., Perovskite Membranes for high temperature oxygen separation. In *Membrane Engineering for the Treatment of Gases*, E. Drioli, Ed. Royal Society of Chemistry, **July 2011**; Vol. 2 p192-221.

[45]   Kharton, V.V.; Shaula, A.L.; Snijkers, F.M.M.; Cooymans, J.F.C.; Luyten, J.J.; Yaremchenko, A.A.; Valente, A.A.; Tsipis, E.V.; Frade, J.R.; Marques, F.M.B.; Rocha, J. Processing, stability and oxygen permeability of $Sr(Fe, Al)O_3$-based ceramic membranes. *J. Membr. Sci.* **2005**, 252, 215-225.

[46]   Tenelshof, J.E.; Bouwmeester, H.J.M.; Verweij, H. Oxygen-transport through $La_{1-x}Sr_xFeO_{3-delta}$ membranes .1. permeation in air/He gradients. *Solid State Ionics* **1995**, 81, 97-109.

[47]   Teraoka, Y.; Shimokawa, H.; Kang, C.Y.; Kusaba, H.; Sasaki, K. Fe-based perovskite-type oxides as excellent oxygen-permeable and reduction-tolerant materials. *Solid State Ionics* **2006**, 177, 2245-2248.

[48]   Zhu, X.F.; Wang, H.H.; Yang, W.S. Novel cobalt-free oxygen permeable membrane. *Chem. Commun.* **2004**, 1130-1131.

[49]   Wang, H.H.; Tablet, C.; Feldhoff, A.; Caro, J. A cobalt-free oxygen-permeable membrane based on the perovskite-type oxide $Ba_{0.5}Sr_{0.5}Zn_{0.2}Fe_{0.8}O_{3-delta}$. *Adv. Mater.* **2005**, 17, 1785-1786.

[50]   Watanabe, K.; Takauchi, D.; Yuasa, M.; Kida, T.; Shimanoe, K.; Teraoka, Y.; Yamazoe, N. Oxygen Permeation Properties of Co-Free Perovskite-Type Oxide Membranes Based on $BaFe_{1-y}Zr_yO_{3-delta}$. *J. Electrochem. Soc.* **2009**, 156, E81-E85.

[51]   Kida, T.; Takauchi, D.; Watanabe, K.; Yuasa, M.; Shimanoe, K.; Teraoka, Y.; Yamazoe, N. Oxygen Permeation Properties of Partially A-Site Substituted BaFeO3-delta Perovskites. *J. Electrochem. Soc.* **2009**, 156, E187-E191.

[52]   Wu, K.; Xie, S.; Jiang, G.S.; Liu, W.; Chen, C.S. Oxygen permeation through $(Bi_2O_3)_{0.74}(SrO)_{0.26}$-$Ag_{40\% \text{ v/o}}$ composite. *J. Membr. Sci.* **2001**, 188, 189-193.

[53]   Kim, J.; Lin, Y.S. Synthesis and oxygen permeation properties of ceramic-metal

dual-phase membranes. *J. Membr. Sci.* **2000**, 167, 123-133.

[54]   Chen, C.S.; Boukamp, B.A.; Bouwmeester, H.J.M.; Cao, G.Z.; Kruidhof, H.; Winnubst, A.J.A. Microstructural development, electrical properties and oxygen permeation of zirconia-palladium composites. *Solid State Ionics* **1995**, 76, 23-28.

[55]   Chen, C.S.; Kruidhof, H.; Bouwmeester, H.J.M.; Verweij, H.; Burggraaf, A.J. Thickness dependence of oxygen permeation through erbia-stabilized bismuth oxide silver composites. *Solid State Ionics* **1997**, 99, 215-219.

[56]   Kharton, V.V.; Kovalevsky, A.V.; Viskup, A.P.; Shaula, A.L.; Figueiredo, F.M.; Naumovich, E.N.; Marques, F.M.B. Oxygen transport in $Ce_{0.8}Gd_{0.2}O_{2-delta}$-based composite membranes. *Solid State Ionics* **2003**, 160, 247-258.

[57]   Nigge, U.; Wiemhofer, H.D.; Romer, E.W.J.; Bouwmeester, H.J.M.; Schulte, T.R. Composites of $Ce_{0.8}Gd_{0.2}O_{1.9}$ and $Gd_{0.7}Ca_{0.3}CoO_{3-delta}$ as oxygen permeable membranes for exhaust gas sensors. *Solid State Ionics* **2002**, 146, 163-174.

[58]   Kagomiya, I.; Iijima, T.; Takamura, H. Oxygen permeability of nanocrystalline $Ce_{0.8}Gd_{0.2}O_{1.9}$-$CoFe_2O_4$ mixed-conductive films. *J. Membr. Sci.* **2006**, 286, 180-184.

[59]   Wang, B.; Yi, J.; Winnubst, L.; Chen, C. Stability and oxygen permeation behavior of $Ce_{0.8}Sm_{0.2}O_{2-delta}$-$La_{0.8}Sr_{0.2}CrC_{3-delta}$ composite membrane under large oxygen partial pressure gradients. *J. Membr. Sci.* **2006**, 286, 22-25.

[60]   Burggraaf, H.J.M.; Bouwmeester, A.J., Dense ceramic membranes for oxygen separation. In *Fundamentals of inorganic membrane science and technology*, H. J. M. Burggraaf, Ed. Elseiver **1996**; Vol. 4, pp 435–528.

[61]   Sunarso, J.; Baumann, S.; Serra, J.M.; Meulenberg, W.A.; Liu, S.; Lin, Y.S.; da Costa, J.C.D. Mixed ionic-electronic conducting (MIEC) ceramic-based membranes for oxygen separation. *J. Membr. Sci.* **2008**, 320, 13-41.

[62]   Dittmeyer, R.; Caro, J., Catalytic Membrane Reactors. In *Handbook of Heterogeneous Catalysis*, second ed.; G. Ertl; Knözinger, H.; Schüth, F.; Weitkamp, J., Eds. Wiley-VCH, **2008**; Vol. 4, p 2198-2248.

[63]   Bouwmeester, H.J.M.; Burggraaf, A.J., Fundamentals of Inorganic Membrane Science and Technology. In *Membrane Science and Technology Series*, A. J. Burggraaf; Cot, L., Eds. Elsevier, Amsterdam, **1996**; Vol. 4, p 435-528.

[64]   Basini, L. Fuel rich catalytic combustion: Principles and technological developments in short contact time (SCT) catalytic processes. *Catal. Today* **2006**, 117, 384-393.

[65]   Schroeder, M. Modeling of dense ceramic bilayer membranes. *Phys. Chem. Chem. Phys.* **2005**, 7, 166-172.

[66]   Arnold, M. Studies on the solid state chemistry of perovskite-type oxides for oxygen separating membranes. Dissertation, *Leibniz University Hannover*, **2008**, p 24.

[67]   Schroeder, M. On the behaviour of mixed-conducting complex metal oxides in oxygen potential gradients. Habil Thesis, *RWTH Aachen*, **2006**.

[68]   Guizard, C.G.; Julbe, A.C., Recent Advances in Gas Separation by Microporous Ceramic Membranes. In *Membrane Science and Technology Series*, N. K. Kanellopoulos, Ed. Elsevier, Amsterdam, **2000**; Vol. 6, p 435-472.

[69]   Tablet, C.; Grubert, G.; Wang, H.H.; Schiestel, T.; Schroeder, M.; Langanke, B.; Caro, J. Oxygen permeation study of perovskite hollow fiber membranes. *Catal. Today* **2005**, 104, 126-130.

[70]   Wang, H.; Schiestel, T.; Tablet, C.; Schroeder, M.; Caro, J. Mixed oxygen ion and electron conducting hollow fiber membranes for oxygen separation. *Solid State Ionics* **2006**, 177, 2255-2259.

[71]   Huang, K.Q.; Schroeder, M.; Goodenough, J.B., Oxygen Permeation in Co-containing Perovskites: Surface Exchange vs. Bulk Diffusion. In *Proceedings of the International Symposium "Solid State Ionic Devices"*, E. D. Wachsman; Akridge, J. R.; Liu, M.; Yamazoe, N., Eds. The Electrochemical Society Proceedings Series, **1999**; p 95.

[72]   Kim, S.; Yang, Y.L.; Jacobson, A.J.; Abeles, B. Oxygen surface exchange in mixed ionic electronic conductor membranes. *Solid State Ionics* **1999**, 121, 31-36.

[73]   Hohnke, D.K. Ionicconduction in dopedoxides with the fluoritestructure. *Solid State Ionics* **1981**, 5, 531-534.

[74]   Istomin, S.Y.; Abdyusheva, S.V.; Svensson, G.; Antipov, E.V. Synthesis, crystal and magnetic structure of a novel brownmillerite-type compound $Ca_2Co_{1.6}Ga_{0.4}O_5$. *J. Solid State Chem.* **2004**, 177, 4251-4257.

[75]   Ohgushi, K.; Yamaura, J.-i.; Ichihara, M.; Kiuchi, Y.; Tayama, T.; Sakakibara, T.; Gotou, H.; Yagi, T.; Ueda, Y. Structural and electronic properties of pyrochlore-type $A_2Re_2O_7(A = Ca, Cd, and Pb)$. *Phys. Rev. B* **2011**, 83.

[76]   Bredesena, R.; Jordal, K.; Bolland, A. High-temperature membranes in power generation with CO2 capture. *Chem. Eng. Process.* **2004**, 43, 1129-1158.

[77]   Goldschmidt, V.M. The laws of crystal chemistry. *Naturwissenschaften* **1926**, 14, 477-485.

[78]   Cook, R.L.; Sammells, A.F. On the systematic selection of perovskite solid electrolytes for intermediate temperature fuel cells. *Solid State Ionics* **1991**, 45, 311-321.

[79]   http://uk.wikipedia.org/wiki/%D0%A4%D0%B0%D0%B9%D0%BB:Kristallstr uktur_Per ovskit.png

[80]   Yang, L.; Tan, L.; Gu, X.H.; Jin, W.Q.; Zhang, L.X.; Xu, N.P. A new series of $Sr(Co,Fe,Zr)O_{3-(delta)}$ perovskite-type membrane materials for oxygen permeation. *Ind. Eng. Chem. Res.* **2003**, 42, 2299-2305.

[81]   Yakovlev, S.; Yoo, C.Y.; Fang, S.; Bouwmeester, H.J.M. Phase transformation and oxygen equilibration kinetics of pure and Zr-doped $Ba_{0.5}Sr_{0.5}Co_{0.8}Fe_{0.2}O_{3-delta}$ perovskite oxide probed by electrical conductivity relaxation. *Appl. Phys. Lett.* **2010**, 96, 254101.

[82]   Kida, T.; Yamasaki, A.; Watanabe, K.; Yamazoe, N.; Shimanoe, K. Oxygen-permeable membranes based on partially B-site substituted $BaFe_{1-y}M_yO_{3-delta}$ (M=Cu or Ni). *J. Solid State Chem.* **2010**, 183, 2426-2431.

[83]   Liu, X.T.; Zhao, H.L.; Yang, J.Y.; Li, Y.; Chen, T.; Lu, X.G.; Ding, W.Z.; Li, F.S. Lattice characteristics, structure stability and oxygen permeability of $BaFe_{1-x}Y_xO_{3-delta}$ ceramic membranes. *J. Membr. Sci.* **2011**, 383, 235-240.

[84]   Zhang, K.; Ran, R.; Ge, L.; Shao, Z.P.; Jin, W.Q.; Xu, N.P. Double-site yttria-doped $Sr_{1-x}Y_xCo_{1-y}Y_yO_{3-delta}$ perovskite oxides as oxygen semi-permeable membranes. *J. Alloys Compd.* **2009**, 474, 477-483.

[85]   Voigt, I.; Pippardt, U.; Burckhardt, W.; Kriegel, R.; Schulz, M.; Sommer, E.; Reuner, W.; Kanis, M., High temperature oxygen separation with ceramic membranes. In *11. Aachener Membrankolloquium*, **2007**; pp 133-144.

[86]   Kriegel, R.; Kircheisen, R.; Ritter, K. *DE 10 2009 050 019 B3*, 2011.03.17, **2009**.

[87]   Schiestel, T.; Kilgus, M.; Peter, S.; Caspary, K.J.; Wang, H.; Caro, J. Hollow fibre perovskite membranes for oxygen separation. *J. Membr. Sci.* **2005**, 258, 1-4.

[88]   Feldhoff, A.; Arnold, M.; Martynczuk, J.; Gesing, T.M.; Wang, H. The sol-gel synthesis of perovskites by an EDTA/citrate complexing method involves nanoscale solid state reactions. *Solid State Sci.* **2008**, 10, 689-701.

[89]   Feldhoff, A.; Martynczuk, J.; Wang, H. Advanced $Ba_{0.5}Sr_{0.5}Zn_{0.2}Fe_{0.8}O_{3-delta}$ perovskite-type ceramics as oxygen selective membranes: Evaluation of the synthetic process. *Prog. Solid State Chem.* **2007**, 35, 339-353.

[90]   Luo, H.; Jiang, H.; Klande, T.; Cao, Z.; Liang, F.; Wang, H.; Caro, J. Novel Cobalt-Free, Noble Metal-Free Oxygen-Permeable $40Pr_{0.6}Sr_{0.4}FeO_{3-\delta}-60Ce_{0.9}Pr_{0.1}O_{2-\delta}$ Dual-Phase Membrane. *Chem. Mater.* **2012**, 24, 2148-2154.

[91]   Kharton, V.V., Solid State Electrochemistry II: Electrodes, Interfaces and Ceramic membranes. **2011**, p 416.

[92]   Basile, A.; Gallucci, F., Membranes for membrane reactors: preparation, optimization and selection. **2011**, p 130.

[93]   Kharton, V.V.; Kovalevsky, A.V.; Yaremchenko, A.A.; Snijkers, F.M.M.; Cooymans, J.F.C.; Luyten, J.J.; Markov, A.A.; Frade, J.R.; Marques, F.M.B. Oxygen transport and thermomechanical properties of $SrFe(Al)O_{3-delta}-SrAl_2O_4$ composites: microstructural effects. *J. Solid State Electrochem.* **2006**, 10, 663-673.

[94]   Wang, H.H.; Kolsch, P.; Schiestel, T.; Tablet, C.; Werth, S.; Caro, J. Production of high-purity oxygen by perovskite hollow fiber membranes swept with steam. *J. Membr. Sci.* **2006**, 284, 5-8.

[95]   Ito, W.; Nagai, T.; Sakon, T. Oxygen separation from compressed air using a mixed conducting perovskite-type oxide membrane. *Solid State Ionics* **2007**, 178, 809-816.

[96]   Liang, F.Y.; Jiang, H.Q.; Schiestel, T.; Caro, J. High-purity oxygen production from air using perovskite hollow fiber membranes. *Ind. Eng. Chem. Res.* **2010**, 49, 9377-9384.

[97]   Zhu, X.F.; Sun, S.M.; Cong, Y.; Yang, W.S. Operation of perovskite membrane under vacuum and elevated pressures for high-purity oxygen production. *J. Membr. Sci.* **2009**, 345, 47-52.

[98]   Wang, H.H.; Tablet, C.; Feldhoff, A.; Caro, H. Investigation of phase structure, sintering, and permeability of perovskite-type $Ba_{0.5}Sr_{0.5}Co_{0.8}Fe_{0.2}O_{3-delta}$ membranes. *J. Membr. Sci.* **2005**, 262, 20-26.

[99]   Dyer, P.N.; Richards, R.E.; Russek, S.L.; Taylor, D.M. Ion transport membrane technology for oxygen separation and syngas production. *Solid State Ionics* **2000**, 134, 21-33.

[100]   Wang, H.H.; Cong, Y.; Yang, W.S. Oxygen permeation study in a tubular $Ba_{0.5}Sr_{0.5}Co_{0.8}Fe_{0.2}O_{3-delta}$ oxygen permeable membrane. *J. Membr. Sci.* **2002**, 210, 259-271.

[101]   Tan, X.Y.; Liu, Y.T.; Li, K. Mixed conducting ceramic hollow-fiber membranes for air separation. *AIChE J.* **2005**, 51, 1991-2000.

[102]   Tan, X.Y.; Liu, Y.T.; Li, K. Preparation of LSCF ceramic hollow-fiber membranes for oxygen production by a phase-inversion/sintering technique. *Ind. Eng. Chem. Res.* **2005**, 44, 61-66.

[103]   Wang, Z.G.; Yang, N.T.; Meng, B.; Tan, X.Y.; Li, K. Preparation and oxygen permeation properties of highly asymmetric $La_{0.6}Sr_{0.4}Co_{0.2}Fe_{0.8}O_{3-alpha}$ perovskite hollow-fiber membranes. *Ind. Eng. Chem. Res.* **2009**, 48, 510-516.

[104]   Tan, X.Y.; Li, K. Oxygen production using dense ceramic hollow fiber membrane modules with different operating modes. *AIChE J.* **2007**, 53, 838-845.

[105]   Tan, X.Y.; Wang, Z.G.; Meng, B.; Meng, X.X.; Li, K. Pilot-scale production of oxygen from air using perovskite hollow fibre membranes. *J. Membr. Sci.* **2010**, 352, 189-196.

[106]   Wang, H.H.; Cong, Y.; Yang, W.S. Investigation on the partial oxidation of methane to syngas in a tubular $Ba_{0.5}Sr_{0.5}Co_{0.8}Fe_{0.2}O_{3-delta}$ membrane reactor. *Catal. Today* **2003**, 82, 157-166.

[107]   Zhu, X.; Wang, H.; Cong, Y.; Yang, W. Partial oxidation of methane to syngas in

BaCe$_{0.15}$Fe$_{0.85}$O$_{3-delta}$ membrane reactors. *Catal. Lett.* **2006**, 111, 179-185.

[108] Wang, H.; Tablet, C.; Schiestel, T.; Werth, S.; Caro, J. Partial oxidation of methane to syngas in a perovskite hollow fiber membrane reactor. *Catal. Commun.* **2006**, 7, 907-912.

[109] Tong, J.H.; Yang, W.S.; Cai, R.; Zhu, B.C.; Lin, L.W. Novel and ideal zirconium-based dense membrane reactors for partial oxidation of methane to syngas. *Catal. Lett.* **2002**, 78, 129-137.

[110] Luo, H.; Wei, Y.; Jiang, H.; Yuan, W.; Lv, Y.; Caro, J.; Wang, H. Performance of a ceramic membrane reactor with high oxygen flux Ta-containing perovskite for the partial oxidation of methane to syngas. *J. Membr. Sci.* **2010**, 350, 154-160.

[111] Zhu, X.; Li, Q.; Cong, Y.; Yang, W. Syngas generation in a membrane reactor with a highly stable ceramic composite membrane. *Catal. Commun.* **2008**, 10, 309-312.

[112] Zhu, X.; Li, Q.; He, Y.; Cong, Y.; Yang, W. Oxygen permeation and partial oxidation of methane in dual-phase membrane reactors. *J. Membr. Sci.* **2010**, 360, 454-460.

[113] Jiang, H.Q.; Wang, H.H.; Liang, F.Y.; Werth, S.; Schirrmeister, S.; Schiestel, T.; Caro, J. Improved water dissociation and nitrous oxide decomposition by in situ oxygen removal in perovskite catalytic membrane reactor. *Catal. Today* **2010**, 156, 187-190.

[114] Centi, G.; Galli, A.; Montanari, B.; Perathoner, S.; Vaccari, A. Catalytic decomposition of N_2O over noble and transition metal containing oxides and zeolites. Role of some variables on reactivity. *Catal. Today* **1997**, 35, 113-120.

[115] Gunasekaran, N.; Rajadurai, S.; Carberry, J.J. Catalytic decomposition of nitrous oxide over perovskite type solid oxide solutions and supported noble metal catalysts. *Catal. Lett.* **1995**, 35, 373-382.

[116] Perez-Ramirez, J.; Kapteijn, F.; Mul, G.; Moulijn, J.A. Superior performance of ex-framework FeZSM-5 in direct N_2O decomposition in tail-gases from nitric acid plants. *Chem. Commun.* **2001**, 693-694.

[117] Russo, N.; Mescia, D.; Fino, D.; Saracco, G.; Specchia, V. N_2O decomposition over perovskite catalysts. *Ind. Eng. Chem. Res.* **2007**, 46, 4226-4231.

2 Phase stability and permeation behavior of a dead-end $Ba_{0.5}Sr_{0.5}Co_{0.8}Fe_{0.2}O_{3-\delta}$ (BSCF) tube membrane

2.1 Summary

Among the OTM materials, the perovskite $Ba_{0.5}Sr_{0.5}Co_{0.8}Fe_{0.2}O_{3-\delta}$ (BSCF), which has a cubic structure, is one of the most studied materials for oxygen separation from air and as cathode in solid-oxide fuel cells due to its high oxygen transport properties. Because of the high concentration of the mobile oxygen vacancies in the perovskite lattice, BSCF exhibits a very high oxygen-permeation flux over a wide temperature range. However, for permeation temperatures below 850 °C, stability problems are reported. The structural instability of BSCF is attributed to an unsuitable redox state of cobalt that exhibits an ionic radius that is too small to be tolerated by the cubic perovskite structure, which then becomes unstable.

In the first part of this chapter, we will first study the phase stability of BSCF membrane in a high-purity oxygen atmosphere as it is present on the permeate side of the membrane. The microstructure of a BSCF membrane, which developed during operation under a dynamic flow of oxygen in the intermediate temperature (ca. 500-850 °C) range, were investigated in detail by X-ray diffraction (XRD), Scanning electron microscopy (SEM), Energy dispersive X-ray spectroscopy (EDXS), Transmission electron microscopy (TEM), Scanning transmission electron microscopy (STEM), Selected area electron diffraction (SAED), and Electron energy-loss spectroscopy (EELS). At 950 °C, a high oxygen purity of almost 100 vol.% and a stable oxygen-permeation flux were observed during the long-term operation for 100 h. However, at 750 °C, the oxygen-permeation flux continuously decreases with time, and the BSCF tube membrane is structurally unstable. The phase instability of BSCF is due to a partial decomposition of the bulk cubic perovskite phase into a hexagonal perovskite, $Ba_{0.5\pm x}Sr_{0.5\pm x}CoO_{3-\delta}$, and a trigonal mixed oxide $Ba_{1-x}Sr_xCo_{2-y}Fe_yO_{5-\delta}$. The strong formation of secondary phases at higher local oxygen chemical potentials during dynamic oxygen flux suggests that the valence and spin state of the most easy redoxable

cation (i.e., cobalt) is the key for an understanding of BSCF's decomposition in the intermediate temperature range. The phase stability of BSCF (i.e., cobalt in the proper redox state) can be maintained by operating BSCF membranes in the high-temperature regime.

In the second part of this chapter, after the identification of stable operation conditions for the BSCF membrane, pure oxygen will be produced using dead-end BSCF tubes in a (i) pressure-driven process, (ii) vacuum process, and (iii) by combining both techniques. In all cases, good BSCF stability was found when the BSCF membrane was operated at temperatures $\geq$ 850 °C and oxygen with a purity of almost 100 vol.% was obtained. It was also found that, for the same oxygen partial pressure difference, the oxygen permeation flux in the vacuum process is significantly higher than that in the pressure-driven process at all investigated temperatures. Moreover, in all cases, oxygen permeation and oxygen ionic conductivity can be described by the Wagner theory for bulk diffusion of oxygen ions as rate-limiting step with the logarithmic ratio of the oxygen partial pressures on feed and permeate sides as driving force.

2.2 Phase stability and permeation behavior of a dead-end Ba$_{0.5}$Sr$_{0.5}$Co$_{0.8}$Fe$_{0.2}$O$_{3-\delta}$ tube membrane in high-purity oxygen production

Fangyi Liang, Heqing Jiang, Huixia Luo, Jürgen Caro and Armin Feldhoff

Phase Stability and Permeation Behavior of a Dead-End Ba$_{0.5}$Sr$_{0.5}$Co$_{0.8}$Fe$_{0.2}$O$_{3-\delta}$ Tube Membrane in High-Purity Oxygen Production

Fangyi Liang,[†] Heqing Jiang,[‡] Huixia Luo,[†] Jürgen Caro,[†] and Armin Feldhoff[*,†]

[†]Institute of Physical Chemistry and Electrochemistry, Leibniz University Hannover, Callinstrasse 3A, D-30167 Hannover, Germany

[‡]Max-Planck-Institut für Kohlenforschung, Kaiser-Wilhelm-Platz 1 D-45470 Mülheim an der Ruhr, Germany

ABSTRACT: Phase stability and oxygen permeation behavior of Ba$_{0.5}$Sr$_{0.5}$Co$_{0.8}$Fe$_{0.2}$O$_{3-\delta}$ (BSCF) dead-end tube membranes were investigated in long-term oxygen production at 950 and 750 °C. At 950 °C, the BSCF tube membranes exhibit good long-term phase stability and a stable oxygen permeation flux. However, at the intermediate temperature of 750 °C, both the oxygen permeation flux and the oxygen purity decrease continuously. This behavior is related to the formation of two secondary phases that are a hexagonal perovskite, Ba$_{0.5\pm x}$Sr$_{0.5\pm x}$CoO$_{3-\delta}$, and a trigonal mixed oxide, Ba$_{1-x}$Sr$_x$Co$_{2-y}$Fe$_y$O$_5$, that evolved in the ceramic membrane made of cubic BSCF perovskite during the dynamic flow of oxygen through it. Tensile stress as a result of phase formation causes the development of cracks in the membrane, which spoil the purity of the permeated oxygen. The partial degradation of cubic BSCF perovskite in the intermediate temperature range (750 °C) was more pronounced under the strongly oxidizing conditions on the oxygen supply (feed) side than on the oxygen release (permeate) side of the membrane. The structural instability of BSCF is attributed to an unsuitable redox state of cobalt, that exhibits an ionic radius that is too small to be tolerated by the cubic perovskite structure, which then becomes unstable. The phase stability of cubic BSCF (i.e., the proper redox states of cobalt) can be maintained by operating the membrane in the high temperature regime (950 °C).

KEYWORDS: perovskite, mixed conductor, decomposition, oxygen permeation, oxygen production
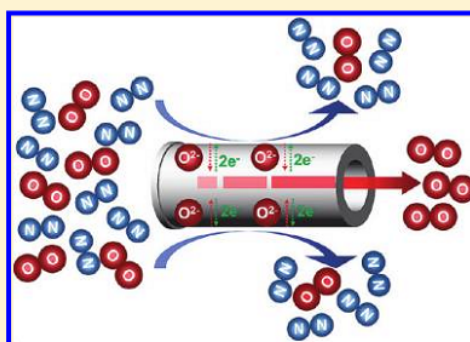
1. INTRODUCTION

Oxygen is the third-largest-volume chemical produced worldwide,[1] and most of the industrial applications for oxygen require high-purity oxygen. Oxygen-transporting membranes (OTMs) can separate oxygen from air, which is a gas mixture containing approximately 78 vol % N$_2$ and 21 vol % O$_2$,[2] or from other oxygen-containing gases. OTMs can theoretically produce oxygen at purities of up to 100% and are believed to possess the potential to reduce the cost of high-purity oxygen production compared to the conventional cryogenic processes.[3] Moreover, OTM reactors have been developed for such potential applications as the partial oxidation of hydrocarbons,[4−8] the production of hydrogen by thermal water splitting in combination with olefin and synthesis gas production,[9−11] and the decomposition of nitrogen oxides.[12,13]

High-purity oxygen can be obtained with the use of OTMs when the oxygen partial pressure at one surface (feed side) is higher than that at the opposite surface (permeate side). The oxygen partial pressure difference can be achieved through the elevation of the oxygen partial pressure on the feed side by the compression of air to pressures higher than 1 bar, the reduction of the oxygen pressure on the permeate side by a vacuum pump, a combination of both techniques, or the use of steam as a condensable sweep gas on the permeate side.[14] The thermal activation of a membrane's oxygen-transport properties

requires the OTM to operate at temperatures of approximately 700−950 °C. The authors of several studies on the high-purity oxygen production have been reported using tubular membrane geometries, instead of conventional flat disks, which are capillary hollow-fiber[15,16] or tube membranes[17,18] that overcome the problem of high-temperature sealing by allowing the seal to be placed in the cold zone.

In the past few decades, many OTMs with high oxygen permeabilities have been developed that are based on mixed ionic-electronic conductors (MIEC) solid oxides, such as SrCo$_{0.8}$Fe$_{0.2}$O$_{3-\delta}$,[19] BaCo$_{0.4}$Fe$_{0.4}$Zr$_{0.2}$O$_{3-\delta}$,[20] BaCo$_{0.7}$Fe$_{0.2}$Ta$_{0.1}$O$_{3-\delta}$,[21] Ba$_{0.5}$Sr$_{0.5}$Fe$_{0.9}$Al$_{0.1}$O$_{3-\delta}$,[22] Ba$_{0.5}$Sr$_{0.5}$Fe$_{0.8}$Cu$_{0.2}$O$_{3-\delta}$,[23] and Ba$_{0.5}$Sr$_{0.5}$Co$_{0.8}$Fe$_{0.2}$O$_{3-\delta}$ (denoted BSCF).[24] Among these compounds, BSCF, which assumes a cubic perovskite structure, has been regarded as one of the most promising materials for oxygen separation from air and for cathodes in solid-oxide fuel cells.[25] Because of the high concentration of the mobile oxygen vacancies in the perovskite lattice,[26] BSCF exhibits a very high oxygen-permeation flux over a wide temperature range.[24] Zhu et al.[18] have observed the stable oxygen permeation behavior of a BSCF perovskite tube membrane under vacuum and elevated pressures
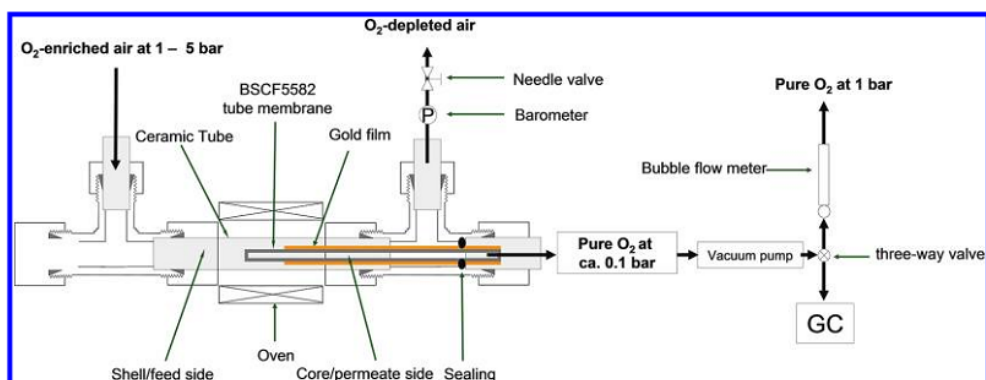
Figure 1. Permeator in dead-end geometry for the production of high-purity oxygen.

for high-purity oxygen production at 925 °C. However, Shao et al.[24] and van Veen et al.[27] have reported that stable oxygen permeation is achieved only when the operating temperatures are higher than 850 °C. During operation in the intermediate temperature (IT, i.e., approximately 500−850 °C) range, however, the oxygen-permeation flux through the BSCF membrane has been observed to decrease, which has been attributed in several reports[24,28−31] to a partial decomposition of the bulk cubic perovskite phase. Shao et al.[24] and Rebeilleau-Dassoneville et al.[28] have observed reflections of noncubic phases in the X-ray diffraction (XRD) patterns of BSCF after the samples were annealed in the IT range. Based on the same experimental technique, Švarcová et al.[30] have described the occurrence of hexagonal perovskite (2H or 4H polymorphs) in addition to the cubic phase. Arnold et al.[29,32] have investigated the formation of cubic BSCF in a sol−gel-based process by analyzing XRD powder patterns that were obtained in situ in the IT range and from quenched intermediate powders. They observed diffraction patterns similar to those observed by Švarcová et al.[30] during partial decomposition of BSCF in the same temperature range. They also noted the reciprocity between the formation and decomposition processes of BSCF. Using transmission electron microscopy (TEM), Arnold et al.[29] clearly showed that some phases, that evolved in the IT range can be described as distorted polytypes with different sequences of cubic and hexagonal close-packed layers, that consist of oxygen and A-site cations (Ba or Sr). These polytypes therefore constitute intergrown structures of cubic and 2H hexagonal perovskite. Using TEM, Mueller et al.[33] observed structural changes not only in the grain boundaries of polycrystalline BSCF ceramic, but also in the BSCF grains themselves by the formation of extended platelets. They mainly addressed the grain boundaries and found barium and cobalt-enriched 2H hexagonal perovskite. Efimov et al.[31] studied, by TEM, BSCF powder and ceramic that had been exposed to IT. They found not only barium- and cobalt-enriched hexagonal perovskite, which was assigned an approximate stoichiometry of $Ba_{0.6}Sr_{0.4}CoO_{3−\delta}$, but also barium-enriched and heavily cobalt-enriched trigonal 15R-related $Ba_{1−x}Sr_xCo_{2−y}Fe_yO_{5−\delta}$. The first XRD diffractograms taken by Shao et al.[24] of a BSCF membrane after it was dynamically operated in an oxygen permeation flux for 400 h at 750 °C showed significantly stronger reflection intensities from additional phases on the feed (air) side as compared to the permeate (helium) side. Microstructure investigations in the aforementioned studies, however, were made solely on BSCF powders or ceramic pellets after they were annealed in a static (air) atmosphere.

In this report, we extend the work of Shao et al.[24] and investigate the microstructure of a BSCF membrane, which developed during operation under a dynamic flow of oxygen in the IT range, by scanning electron microscopy (SEM) analysis, TEM, and XRD. We correlate the observed membrane microstructure, which differs between the feed and permeate side, with the oxygen permeation behavior (i.e., oxygen flux and oxygen purity). Dead-end BSCF tube membranes were used for the high-purity oxygen production using air or oxygen-enriched air as feed gases.

2. EXPERIMENTAL SECTION

Oxygen Production in Dead-End Membrane Reactor. The $Ba_{0.5}Sr_{0.5}Co_{0.8}Fe_{0.2}O_{3−\delta}$ (BSCF) tubes (400 mm long, 10 mm outer diameter, 1 mm wall thickness) were purchased from Fraunhofer Institute IKTS Dresden/Hermsdorf (Germany). One of the two ends of the tube is closed by an approximately 1 mm thick disk of the same BSCF material.[34]

Oxygen was produced in a dead-end membrane permeator as shown in Figure 1. A stream of air, as a nitrogen/oxygen mixture, is supplied from the left to the dead end of the tube and leaves the setup as oxygen-depleted air. Oxygen permeates the MIEC tube walls via a flux of oxygen anions, which is accompanied by counterflowing electrons. Permeated oxygen leaves the setup to the right via the interior of the tube to the right. In the experiment, parts of the tube membrane were coated by a gold paste (Heraeus), except the 3 cm part near the dead end. The tube segment was painted by the Au paste, which then was sintered at 950 °C for 5 h. This procedure was applied 3-fold to obtain a dense gold film, which the oxygen can not permeate. Inspection by light microscope of the gold sealing after long-term permeation experiment revealed a still hole- and crack-free dense layer. This is consistent with the good compatibility of gold sealant with perovskite membrane as reported by Tong et al.[35] for 2000 h long high-temperature experiments. The uncoated part of our tube with an effective membrane area of 9.1 cm² for the outer membrane surface was placed in the middle of the oven, thus ensuring isothermal conditions. Oxygen-enriched air with 50 vol. % O_2 at an elevated pressure of 5 bar was fed at a rate of 500 cm³(STP)min⁻¹ to the feed side. Flow rates were controlled by gas mass-flow controllers (Bronkhorst). High-purity oxygen was produced at approximately 0.1 bar on the core/permeate side. This reduced pressure was achieved with a vacuum pump (Pfeiffer vacuum MVP 015−4). The flow of the outlet on the core/permeate side was mixed with neon (1.0 cm³ (STP)min⁻¹, 99.995%) as an internal standardization gas, which allowed the determination of the absolute flux of the permeate gas by an online coupled gas chromatograph (Agilent 7890A) that was equipped with a Carboxen 1000 column.
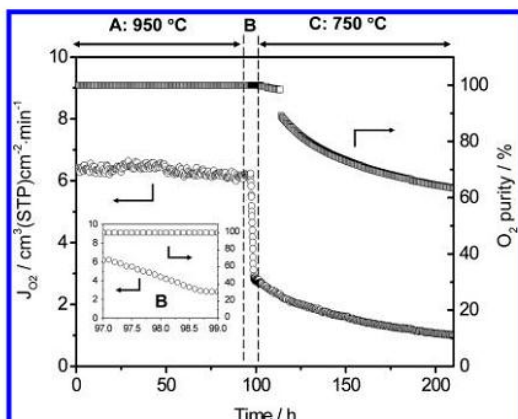
Figure 2. Long-term operation of oxygen production using a dead-end BSCF tube membrane at 950 and 750 °C. Shell/feed side: 50 vol % oxygen-enriched air at 5 bar with a flow rate of 500 cm³(STP) min⁻¹. Core/permeate side: O₂ at approximately 0.1 bar. Inset B shows the continuous decrease of the oxygen flux from the isothermal region A at 950 °C to the isothermal region C at 750 °C. For the associated XRD results, see Figure 7; for SEM micrographs see Figure 8.

The leaking of nitrogen and oxygen through pores or cracks is assumed to be in accordance with the Knudsen diffusion mechanism. Then, for the experiment with 50 vol % oxygen-enriched air at the feed side, the fluxes of leaked nitrogen and oxygen are related by eq 1.

$$J_{N_2}^{Leak} : J_{O_2}^{Leak} = \sqrt{\frac{32}{28}} \frac{0.5}{0.5} = 1.07 \tag{1}$$

The oxygen permeation flux J_{O_2} (cm³ (STP) min⁻¹ cm⁻²) can be calculated by eq 2, in which the leakage of oxygen is subtracted by taking into account the leakage of nitrogen.

$$J_{O_2} = \left(C_{O_2} - \frac{C_{N_2}}{1.07} \right) \frac{F}{S} \tag{2}$$

Here, C_{O_2} and C_{N_2} are the oxygen and nitrogen concentrations estimated from calibrated gas chromatograph. F is the total flow rate of the outlet on the core/permeate side, and S is the effective surface for permeation.

Tools for Microstructure Analysis. The XRD data were collected in a $\theta/2\theta$ geometry on a Bruker D8 Advance instrument equipped with a Cu K$_\alpha$ radiation at 40 kV and 40 mA. A receiving slit of 0.05 mm was used and data were collected in step-scan mode in the 2θ range of $20° < 2\theta < 80°$ at intervals of $0.02°$. Scanning electron microscopy (SEM) was performed with a JEOL JSM-6700F at a low excitation voltage of 2 kV for imaging with secondary electrons and at 5 kV for backscattered-electron channelling contrast imaging. Specimens for the latter purpose were prepared using a Buehler VibroMet 2 vibratory polisher. Transmission electron microscopy (TEM) was performed on a JEOL JEM-2100F that was equipped with a Gatan Imaging Filter (GIF 2001) and an Oxford Instruments INCA TEM 200 light-element energy-dispersive X-ray (EDX) spectrometer. Scanning transmission electron microscopy (STEM) imaging was performed on appropriate bright- and dark-field detectors. TEM imaging, selected area electron diffraction (SAED), and electron energy-loss spectroscopy (EELS) were performed on the charge-coupled device (CCD) camera of the GIF.

3. RESULTS AND DISCUSSION

Permeation Behavior of Dead-End BSCF Tube Membrane. The reliability of the dead-end BSCF tube membrane in the
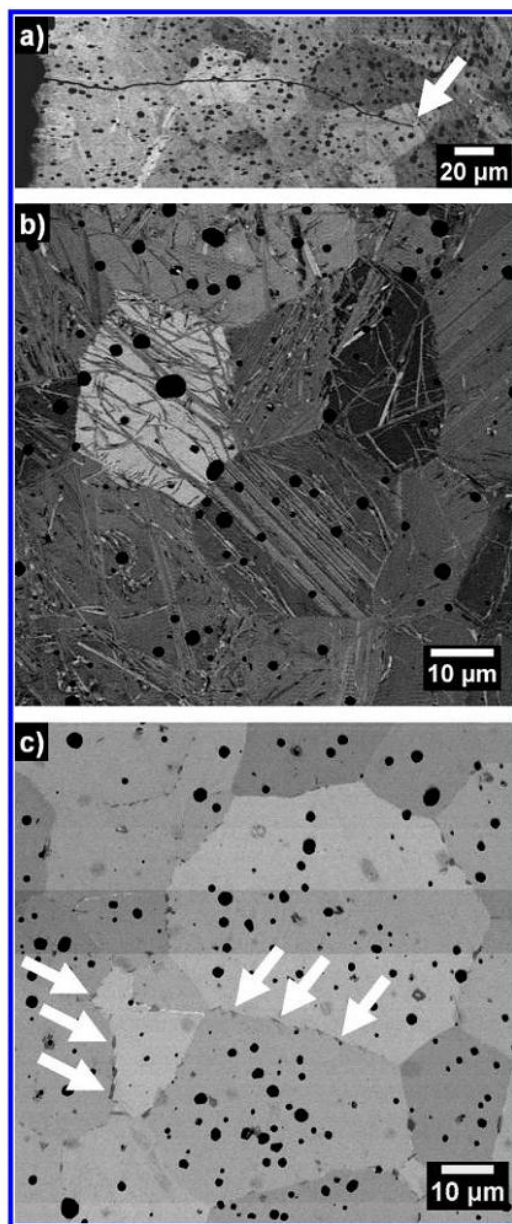

Figure 3. Backscattered-electron channelling contrast images of the BSCF perovskite tube membrane cross-section after the long-term permeation experiment shown in Figure 2 (100 h at 950 °C, 120 h at 750 °C): (a) Overview of shell/feed side showing an approximately 200 μm long crack running into the membrane from the left (shell/feed side). The crack tip is marked by an arrow. (b) Area close to the shell/feed side showing secondary phases criss-crossing BSCF grains. (c) Area close to core/permeate side showing secondary phases in the grain boundaries. Some phases are marked by arrows. Note that the closed porosity of the ceramic membrane appears as black dots.

production of oxygen was evaluated with a feed of 50 vol % oxygen-enriched air at 5 bar and a reduced pressure of approximately 0.1 bar on the permeate side at 950 and 750 °C, as shown in Figure 2. The oxygen-enriched air with different oxygen contents can be produced by using either the organic polymeric

38

hollow-fiber membranes[36] or perovskite hollow-fiber membranes.[15,37] At 950 °C, the oxygen-permeation flux and the oxygen purity were found to be constant over a time period of 100 h. A high oxygen purity of almost 100 vol % (gas chromatograph did not detect any N_2) and a stable oxygen permeation flux of 6.3 $cm^3cm^{-2}min^{-1}$ were observed. The high oxygen purity indicates that the gas leakage is negligible, even at a pressure difference of approximately 6 bar, because of the perfect connection between the BSCF tube and the BSCF disk that forms the dead-end part of the membrane. Moreover, the dead-end tube membrane's geometry can solve the problem of high-temperature sealing by allowing the use of silicon rings outside the high-temperature zone. A stable performance of a dead-end BSCF tube membrane with silver as sealant at 925 °C has also been reported by Zhu et al.[18]

When the temperature was slowly decreased by 2 °Cmin^{-1} from 950 to 750 °C, the oxygen purity initially remains constant at 100%, but the oxygen-permeation flux continuously decreases from 6.6 to 2.8 cm^3 (STP) cm^{-2} min^{-1} (inset in Figure 2). At 750 °C, the oxygen-permeation flux decreases continuously with time from 2.8 cm^3 (STP) cm^{-2} min^{-1} to 1.0 $cm^3cm^{-2}min^{-1}$ after 120 h. This observation is in good agreement with the findings of Shao et al.,[24] van Veen at al.,[27] and Efimov et al.[31] At 750 °C, first the oxygen purity decreases slowly over 10 h. This initial decrease of in the oxygen concentration may be due to a low constant nitrogen flux that results from small sealing imperfections or membrane pin holes, which become increasingly significant if the oxygen flux is decreased by a decrease in the temperature. After approximately 10 h at 750 °C, a sudden decrease in the oxygen purity is observed which is related to the formation of small cracks in the membrane. The further growth of the cracks causes a further decrease of the oxygen purity with time, as shown in Figure 2. Cracks run radially from the perimeter (feed side) into the tube membrane and can be observed in SEM micrographs. After the permeation experiment shown in Figure 2 (100 h at 950 °C and 120 h at 750 °C) was completed, a cross-section of the tube membrane was prepared by vibration polishing to preserve the material's crystallinity to the very surface of the specimen so that backscattered-electron channelling contrast imaging could be applied. Figure 3a shows an overview of the shell/feed side with a crack approximately 200 μm in length. The crack appears black in contrast, because no material is present in the crack opening that could scatter the electrons to the detector. The same holds true for closed porosity, which also is seen as black.

Microstructure Overview. At the higher magnification in Figure 3b, orientation-dependent backscattered-electron channelling contrast allows not only individual BSCF grains with sizes of approximately 20−40 μm to be distinguished but also secondary phases in the grain boundaries and, more significantly, those running through the bulk grains. These secondary phases are predominantly observed in a region up to approximately 200 μm below the shell/feed side, which constitutes the side with the highest oxygen chemical potential in the permeation experiment. Remember, cracks are observed in the same region. Obviously, the formation of secondary phases leads to an accumulation of internal stresses. At the core/permeate side, which is shown in Figure 3c, the situation is different. Here, microstructure changes are essentially restricted to the grain boundaries that are decorated by platelike crystals. Almost no secondary phases run through the BSCF grains.

Microstructure at the Core/Permeate Side. The situation at the core/permeate side is shown in more detail in Figure 4a by bright-field TEM. The distribution of secondary phases at the boundary between BSCF grains 1 and 2 (**A** and **B**) is sketched in the STEM micrograph of Figure 4b. Based on the elemental distributions of Figures 4c to g, phase **B** is enriched in oxygen and in cobalt but depleted in strontium, as compared to BSCF. By quantification of the local EDX spectra, a 2:1 ratio of B-site to A-site cations was observed. This ratio is consistent with a complex trigonal oxide of approximate composition $Ba_{1-x}Sr_xCo_{2-y}Fe_yO_{5-\delta}$, as reported by Efimov et al.[31] The compositional parameters of approximately $x = 0.15$ and $y = 0.25$, however, vary locally. In the **A** regions, smaller crystallites with diameters less than 200 nm were formed. These crystallites decorate the interface between the platelet of phase **B** and grain 1, but are also observed to the lower right. Their occurrence correlates with **A** regions that are almost free of iron (see Figure 4g). The quantification results of local EDX spectra show less than 1 at % iron. Enrichments of cobalt (Figure 4f) and oxygen (Figure 4c) are observed. It is noteworthy that barium and strontium content varies locally in the opposite manner (compare Figures 4d and e). With reference to Efimov et al.[31] and Mueller et al.,[33] we postulate that hexagonal perovskites $Ba_{0.5\pm x}Sr_{0.5\pm x}CoO_{3-\delta}$ (with x $\approx$ 0.1) were formed in region **A**. Although a strontium-enriched hexagonal perovskite is not expected according to other investigators, Figures 4d, e, and g clearly indicate that iron depleted regions correlate with different barium and strontium contents.

The different phases in the grain-boundary region appear with characteristic oxygen fine structures in the EEL spectra of Figure 5a. The O−K fine structure from BSCF corresponds to the room-temperature spectrum reported by Arnold et al.[37] and the one for the hexagonal perovskite (**A**) to the X-ray absorption near-edge structure (XANES) observed by Harvey et al.[39] Hexagonal perovskite is indicated by the absence of the Fe-$L_{2,3}$ signal, which can be seen only very weakly in Figure 5a. The oxygen fine structure of $Ba_{1-x}Sr_xCo_{2-y}Fe_yO_{5-\delta}$ (**B**) is published here for the first time. Some interesting features are noted at the Co-$L_{2,3}$ and Ba-$M_{4,5}$ edges. The Ba-M_5 white line appears constant at 788 eV for all phases and can be used as an internal standard (see Arnold et al.[38] and Efimov et al.[31]) to estimate shifts in the Co-L_3 edge. For BSCF, differences between the maxima of Ba-M_5 and Co-L_3 result in an estimate of 4.4 eV, which is smaller than the value that can be read from the spectrum reported by Efimov et al.[31] This result suggests a stronger oxidation of cobalt in BSCF in our experiment as a result of our use of high-pressure oxygen-enriched air on the feed side of the membrane. The increased oxidation of cobalt also explains why the shift of Co-L_3 to the right is only approximately 0.3 eV, compared to 0.7 eV in the experiment by Efimov et al.[31] More interesting is the observation that the Co-L_3 maximum for the hexagonal perovskite is shifted by 1.0 eV to the right as compared to BSCF. This result indicates that the oxidation state of cobalt is the highest in the hexagonal phase, which leads us directly to the reason for the phase decomposition of BSCF under the chosen operating conditions: the decomposition is induced by an unsuitable valence and spin state of cobalt, which is exposed to the strongly oxidizing conditions in the IT range and is associated with a small ionic radius that makes cobalt unstable in the cubic perovskite structure, as reported by Arnold et al.[29] and Efimov et al.[31] The temperature-dependent EELS experiment by Arnold et al.[38] also suggests a 3+ valence and low-spin state of cobalt in BSCF in the IT range. Our EELS observation (Figure 5b) of higher oxidation states of cobalt in the grain-boundary phases, as compared to BSCF, correlates
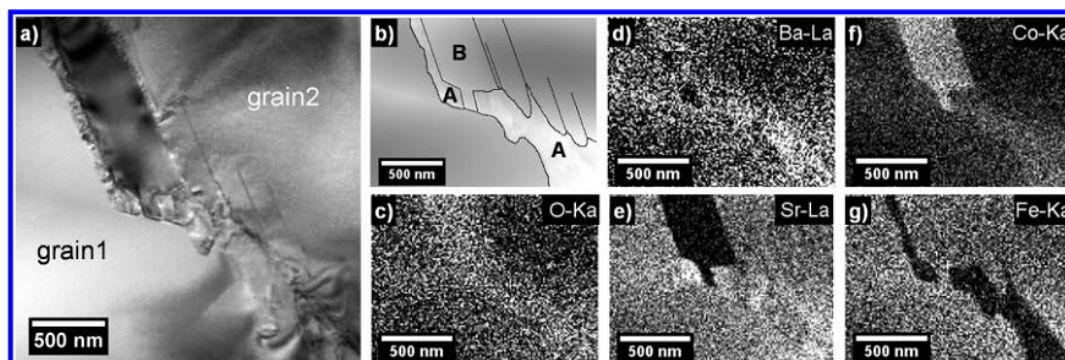
ARTICLE

Figure 4. TEM investigation near the core/permeate side showing a grain boundary region. (a) Bright-field TEM, (b) annular dark-field STEM with grain-boundary phases labeled A and B. (c–g) EDXS elemental distributions (bright contrast correlates with high elemental concentration).
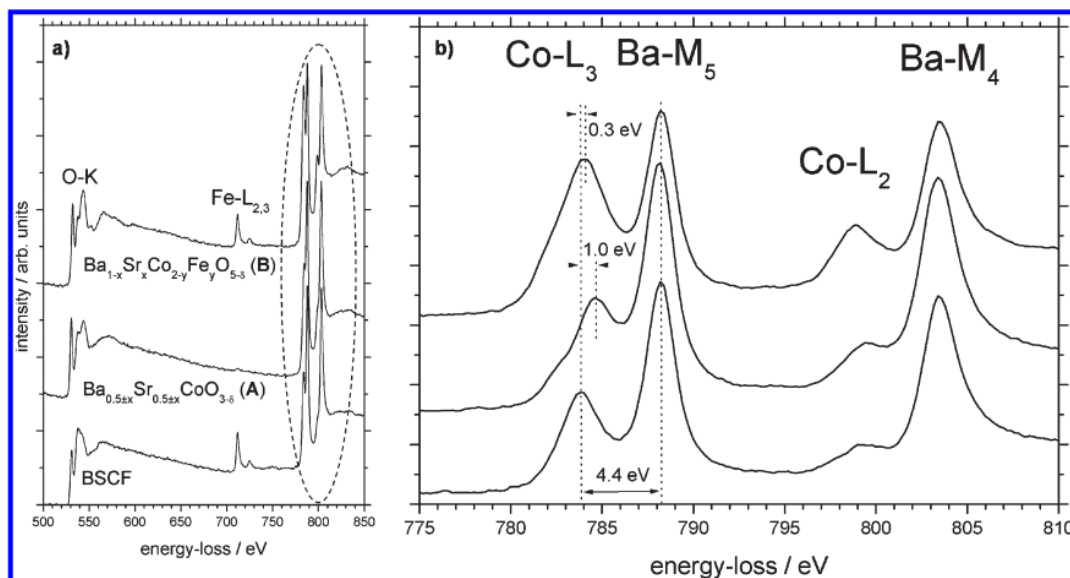

Figure 5. EEL spectra of BSCF and grain-boundary phases near the core/permeate side (see Figure 4b) showing (a) O–K, Fe-L$_{2,3}$, Co-L$_{2,3}$, and Ba-M$_{4,5}$ ionization edges; and (b) a close-up of the Co-L$_{2,3}$ and Ba-M$_{4,5}$ ionization edges.

with the higher amount of oxygen observed in the EDXS elemental distribution in Figure 4c.

Microstructure at the Shell/Feed Side. In agreement with the SEM micrographs in Figure 3, the STEM bright-field micrograph of Figure 6a shows that, near the shell/feed side, microstructure changes are not restricted to the grain boundaries. In the grain boundaries, the same phases are observed as those near the core/permeate side. However, the hexagonal phase (**A**) is the major component relative to the heavily cobalt-enriched trigonal phase (**B**), which was observed to be wrapped by phase **A**. Both phase **A** and phase **B** form extended platelets and separate grains 3 and 4 in Figure 6a. However, they are also found running straight through grain 4 almost parallel to the grain boundary. More interesting, however, are the dense arrays of hexagonal perovskite phase (**A**) that are seen in both grains, which differs from our previous observations. The circle in grain 3 marks the area from which the SAED pattern in Figure 6b was observed. The diffraction pattern shows common strong reflections from cubic BSCF and hexagonal perovskite (**A**) and additional weak reflections that

are attributed only to hexagonal perovskite (**A**). The pattern was indexed in the same manner reported by Mueller et al.,[33] indicating that the close-packed layers of the cubic and hexagonal perovskite are arranged in parallel. Moreover, a comparison of Figures 6a and b indicates that the hexagonal lamellae are grown along cubic $\langle 110 \rangle_c$ directions, which are denoted explicitly as $[101]_c$ and $[011]_c$ here. The cubic $\langle 110 \rangle_c$ directions coincide with the average global directions of oxygen migration in cubic perovskite.[40] Therefore, the hexagonal lamellae formed in our experiments correlate with oxygen pathways in cubic BSCF. The hexagonal lamellae intergrew coherently with the cubic BSCF grains as is evident from in the HRTEM micrograph in Figure 6c. The crystals are observed in the projection along $[11\underline{1}]_c$ such that columns of equal amounts of A-site and B-site cations are observed edge-on and appear as bright spots. Columns of oxygen are located halfway between the bright spots; however, they cannot be seen because of their weak scattering. In any event, the brightness of the spots that represent cationic columns varies locally, which suggests local compositional variations.
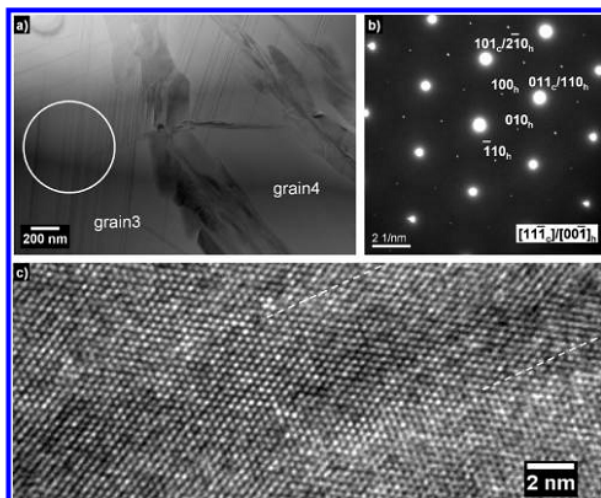
Chemistry of Materials

Figure 6. TEM investigation near the shell/feed side showing a grain-boundary region: (a) Bright-field STEM, (b) SAED pattern of encircled area in a, and (c) HRTEM of hexagonal lamella in cubic BSCF along [11$\underline{1}$]c. Lamella is located between the dashed lines.

Discussion of BSCF's Partial Decomposition. With the findings concerning the local oxygen content and the cobalt valence/spin state, as previously discussed in context with Figures 4 and 5 (core/permeate side), and 6 (shell/feed side), we can identify the appearance of the hexagonal perovskite arrays with migration channels of oxygen in cubic BSCF perovskite, which exhibits the most strongly oxidizing local conditions. In addition, the evolved microstructure strongly suggests that the ideal situation of a rigid metal cationic framework has not been achieved, in that only the anionic oxygen is mobile.[41] Now, the cationic cobalt in BSCF appears to migrate to regions of higher oxygen concentration (oxygen migration pathways). There, cobalt changes its valence and spin state, and then the perovskite structure transforms. To expand the findings of Arnold et al.[29] and Efimov et al.,[31] we identify an unsuitable valence and spin state of cobalt as the main reason for the partial decomposition of BSCF while operating at 750 °C, as opposed to 950 °C. This view is supported by the observation (see Figure 3) that the microstructure changes are more severe at the oxygen-supply side (most strongly oxidizing conditions) as compared to the permeate side. Moreover, observation that the partial decomposition is restricted to the grain boundaries at the core/permeate side points out that the grain boundary environment may be significantly different from the grain volume. The preceding arguments lead then to the conclusion that, at the core/permeate side, oxygen content in the grain boundaries is higher than in the grain volume. Probably, here oxygen is transported preferentially in the grain boundary regions.

More Aspects of Evolved Microstructure. The phases identified by TEM analysis are also observed in the XRD patterns, which were collected on scans of membrane surfaces. Figure 7 shows the XRD patterns of the BSCF membrane before and after the aforementioned long-term operation. The crystal structures on both the feed and permeate sides of the starting BSCF membrane are a pure cubic-perovskite phase (Figure 3a). After the long-term operation, the cubic BSCF perovskite remains as the major phase. However, a hexagonal perovskite $Ba_{0.5\pm x}Sr_{0.5\pm x}CoO_{3-\delta}$ (**A**) has formed on the shell/feed side. Rebeilleau-Dassonneville et al.[28] and Efimov et al.[31] have observed the corresponding signals of
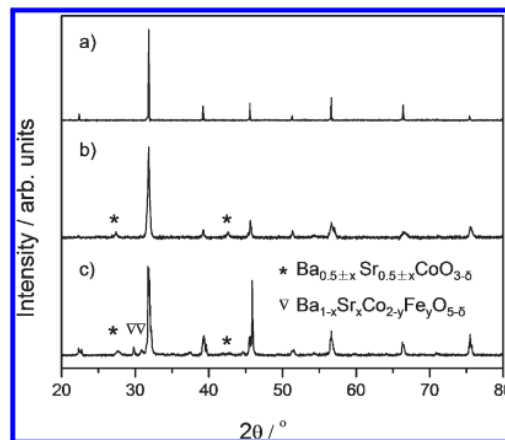

Figure 7. XRD patterns of the BSCF tube membrane: (a) shell-side surface (which is identical to the core-side surface) before permeation, (b) shell/feed-side surface, and (c) core/permeation-side surface after the long-term permeation experiment shown in Figure 2 (100 h at 950 °C, 120 h at 750 °C). For SEM micrographs, see Figure 8.

$Ba_{0.5\pm x}Sr_{0.5\pm x}CoO_{3-\delta}$ (**A**) in XRD patterns and Efimov identified the chemical composition of this phase by STEM-EDXS as $Ba_{0.6}Sr_{0.4}CoO_{3-\delta}$. Here, however, the barium and strontium contents vary locally and the phase can be strontium-enriched (see Figure 4d and e). On the shell/feed side, the content of trigonal $Ba_{1-x}Sr_xCo_{2-y}Fe_yO_{5-\delta}$ (**B**) is too small to be detected by XRD. However, on the core/permeate side, in addition to besides $Ba_{0.5\pm x}Sr_{0.5\pm x}CoO_{3-\delta}$ (**A**), $Ba_{1-x}Sr_xCo_{2-y}Fe_yO_{5-\delta}$ (**B**) is also clearly seen as an additional phase. According to Efimov et al.,[31] trigonal $Ba_{1-x}Sr_xCo_{2-y}Fe_yO_{5-\delta}$ (**B**) can be indexed in space group R$\bar{3}$m and is structurally related to $BaCo_{10}O_{17}$, which was reported by Sun et al.[42] Because of the structural similarity, $Ba_{1-x}Sr_xCo_{2-y}Fe_yO_{5-\delta}$ (**B**) is assumed to give an XRD pattern similar to that of $BaCo_{10}O_{17}$, even though only the structure of the latter phase has been fully resolved thus far (ICSD collection code 240501). We emphasize that the B-site (cobalt and iron) to A-site (barium and strontium) ratio we observed in our analysis is too small to match a stoichiometry of $BaCo_{10}O_{17}$. The main reflection of cubic BSCF perovskite at approximately 32° seems to be broadened. The additional intensities can be attributed to the aforementioned additional phases of hexagonal and trigonal symmetry, which evolve during the partial decomposition of the bulk cubic BSCF phase.

To sort our findings, lets have a look on Figure 8, which presents secondary-electron micrographs of the shell/feed side surface, the cross-sectional area near the shell/feed side, and the core/permeate-side surface of the BSCF membrane before and after the oxygen-permeation experiment of Figure 2 (100 h at 950 °C and 120 h at 750 °C). After the long-term oxygen-permeation experiment in the IT range, secondary phases protrude from the bulk grains at the surface of the shell/feed side (see Figure 8d). In the corresponding broken cross-section (Figure 8e), an approximately 1 μm thick grain-boundary phase is clearly observed. According to the XRD results (see Figure 7b) and the aforementioned TEM results (Figure 6), the secondary phase is primarily the hexagonal perovskite $Ba_{0.5\pm x}Sr_{0.5\pm x}CoO_{3-\delta}$ (**A**). At the core/permeate side (Figure 8f), decoration of grain boundaries is clearly visible, the decorations are composed of trigonal $Ba_{1-x}Sr_xCo_{2-y}Fe_yO_{5-\delta}$ (**B**) and hexagonal perovskite $Ba_{0.5\pm x}Sr_{0.5\pm x}CoO_{3-\delta}$ (**A**), as was analyzed in
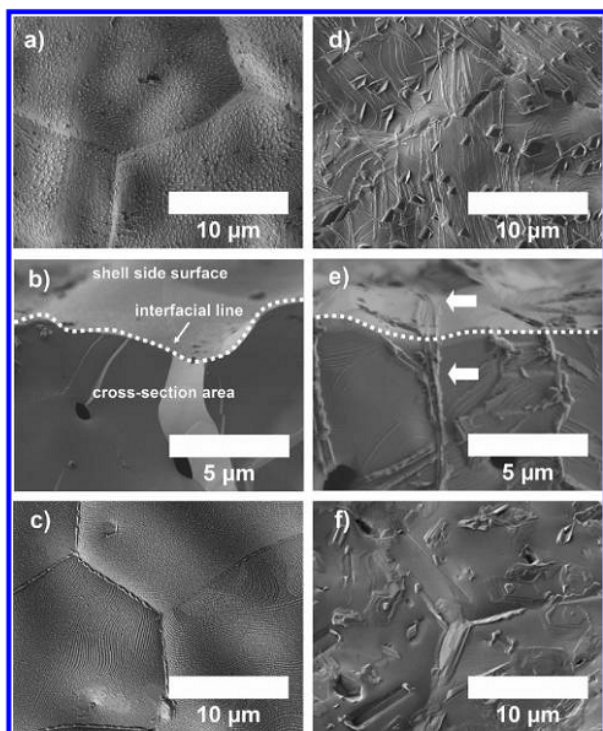
41

Chemistry of Materials

Figure 8. Microstructures of the BSCF perovskite tube membrane before and after the oxygen permeation experiment: Surface view of shell/feed side (a) before and (d) after permeation; broken cross-sectional area near the shell/feed side (b) before and (e) after permeation; surface view of the core/permeation side (c) before and (f) after permeation. For the permeation experiment, see Figure 2; for the XRD patterns, see Figure 7c. White arrows in e mark secondary phase at grain boundary.

context with Figure 4. In the vicinity of internal porosity, hexagonal features (**A**) also appear inside the grains.

CONCLUSIONS

The long-term phase stability and oxygen permeability of dead-end BSCF tube membranes (400 mm long, 10 mm outer diameter, 1 mm wall thickness) were studied under practice-relevant permeation conditions at 950 and 750 °C. A high oxygen purity of almost 100 vol. % and a stable oxygen-permeation flux were observed during the long-term operation for 100 h at 950 °C. However at 750 °C, the oxygen-permeation flux continuously decreases with time, and the BSCF tube membrane is structurally unstable. The phase instability of BSCF is due to a partial decomposition of the bulk cubic perovskite phase into a hexagonal perovskite, $Ba_{0.5\pm x}Sr_{0.5\pm x}CoO_{3-\delta}$, and a trigonal mixed oxide $Ba_{1-x}Sr_xCo_{2-y}Fe_yO_{5-\delta}$. At the core/permeate side, the formation of secondary phases is predominantly restricted to the grain boundaries. At the shell/feed side, which constitutes the region of highest oxygen chemical potential during dynamic oxygen flux through the BSCF membrane material, the formation of secondary phases is most pronounced. Here, the secondary phase is mainly the cobalt-enriched hexagonal perovskite, which is not only found in grain boundaries, but also runs through the bulk grains, leading to important internal stresses, that give rise to membrane cracking at the oxygen-feed side. The stronger formation of secondary

phases at higher local oxygen chemical potentials during dynamic oxygen flux suggests that the valence and spin state of the most flexible redoxable cation (i.e., cobalt) is the key to an understanding of BSCF's decomposition in the intermediate temperature range. The phase stability of BSCF (i.e., the proper redox states of cobalt) can be maintained by operating BSCF membranes in the high-temperature regime (950 °C).

AUTHOR INFORMATION

Corresponding Author
*E-mail: armin.feldhoff@pci.uni-hannover.de.

REFERENCES

(1) Bose, A. C., *Inorganic Membranes for Energy and Environmental Applications*; Springer: New York, 2009; p 4.
(2) Lide, D. R. *CRC Handbook of Chemistry and Physics*; CRC Press: Boca Raton, FL, 1997.
(3) Armstrong, P. A.; Bennet, D. L.; Fprster, E. P. T.; van Stein, E. E. ITM Oxygen for Gasification. In *2004 Gasification Technology Conference: New Technologies Development*; Washington, D.C., Oct 3–6, 2004; Gasification Technologies Council: Arlington, VA, 2004.
(4) Bouwmeester, H. J. M. *Catal. Today* **2003**, *82*, 141.
(5) Tsai, C. Y.; Dixon, A. G.; Moser, W. R.; Ma, Y. H. *AIChE J.* **1997**, *43*, 2741.
(6) Shao, Z. P.; Dong, H.; Xiong, G. X.; Gong, Y.; Yang, W. S. *J. Membr. Sci.* **2001**, *183*, 181.
(7) Yang, W. S.; Wang, H. H.; Zhu, X. F.; Lin, L. W. *Top. Catal.* **2005**, *35*, 155.
(8) Caro, J.; Caspary, K. J.; Hamel, C.; Hoting, B.; Kolsch, P.; Langanke, B.; Nassauer, K.; Schiestel, T.; Schmidt, A.; Schomacker, R.; Seidel-Morgenstern, A.; Tsotsas, E.; Voigt, I.; Wang, H. H.; Warsitz, R.; Werth, S.; Wolf, A. *Ind. Eng. Chem. Res.* **2007**, *46*, 2286.
(9) Jiang, H. Q.; Cao, Z. W.; Schirrmeister, S.; Schiestel, T.; Caro, J. *Angew Chem Int Ed.* **2010**, *49*, 5656.
(10) Jiang, H. Q.; Liang, F. Y.; Czuprat, O.; Efimov, K.; Feldhoff, A.; Schirrmeister, S.; Schiestel, T.; Wang, H. H.; Caro, J. *Chem.—Eur. J.* **2010**, *16*, 7898.
(11) Jiang, H. Q.; Wang, H. H.; Werth, S.; Schiestel, T.; Caro, J. *Angew. Chem., Int. Ed.* **2008**, *47*, 9341.
(12) Jiang, H. Q.; Wang, H. H.; Liang, F. Y.; Werth, S.; Schiestel, T.; Caro, J. *Angew. Chem., Int. Ed.* **2009**, *48*, 2983.
(13) Jiang, H. Q.; Xing, L.; Czuprat, O.; Wang, H. H.; Schirrmeister, S.; Schiestel, T.; Caro, J. *Chem. Commun.* **2009**, 6738.
(14) Wang, H. H.; Kolsch, P.; Schiestel, T.; Tablet, C.; Werth, S.; Caro, J. *J. Membr. Sci.* **2006**, *284*, 5.
(15) Liang, F. Y.; Jiang, H. Q.; Schiestel, T.; Caro, J. *Ind. Eng. Chem. Res.* **2010**, *49*, 9377.
(16) Tan, X. Y.; Wang, Z. G.; Meng, B.; Meng, X. X.; Li, K. *J. Membr. Sci.* **2010**, *352*, 189.
(17) Ito, W.; Nagai, T.; Sakon, T. *Solid State Ionics* **2007**, *178*, 809.

(18) Zhu, X. F.; Sun, S. M.; Cong, Y.; Yang, W. S. *J. Membr. Sci.* **2009**, *345*, 47.

(19) Teraoka, Y.; Zhang, H. M.; Furukawa, S.; Yamazoe, N. *Chem. Lett.* **1985**, 1743.

(20) Yang, L.; Wu, Z. T.; Jin, W. Q.; Xu, N. P. *Ind. Eng. Chem. Res.* **2004**, *43*, 2747.

(21) Luo, H. X.; Tian, B. B.; Wei, Y. Y.; Wang, H. H.; Jiang, H. Q.; Caro, J. *AIChE J.* **2010**, *56*, 604.

(22) Martynczuk, J.; Liang, F. Y.; Arnold, M.; Sepelak, V.; Feldhoff, A. *Chem. Mater.* **2009**, *21*, 1586.

(23) Efimov, K.; Halfer, T.; Kuhn, A.; Heitjans, P.; Caro, J.; Feldhoff, A. *Chem. Mater.* **2010**, *22*, 1540.

(24) Shao, Z. P.; Yang, W. S.; Cong, Y.; Dong, H.; Tong, J. H.; Xiong, G. X. *J. Membr. Sci.* **2000**, *172*, 177.

(25) Shao, Z. P.; Haile, S. M. *Nature* **2004**, *431*, 170.

(26) Kriegel, R.; Kircheisen, R.; Töpfer, J. *Solid State Ionics* **2010**, *181*, 64.

(27) van Veen, A. C.; Rebeilleau, M.; Farrusseng, D.; Mirodatos, C. *Chem. Commun.* **2003**, 32.

(28) Rebeilleau-Dassonneville, M.; Rosini, S.; van Veen, A. C.; Farrusseng, D.; Mirodatos, C. *Catal. Today* **2005**, *104*, 131.

(29) Arnold, M.; Gesing, T. M.; Martynczuk, J.; Feldhoff, A. *Chem. Mater.* **2008**, *20*, 5851.

(30) Švarcová, S.; Wiik, K.; Tolchard, J.; Bouwmeester, H. J. M.; Grande, T. *Solid State Ionics* **2008**, *178*, 1787.

(31) Efimov, K.; Xu, Q. A.; Feldhoff, A. *Chem. Mater.* **2010**, *22*, 5866.

(32) Arnold, M.; Wang, H.; Martynczuk, J.; Feldhoff, A. *J. Am. Ceram. Soc.* **2007**, *90*, 3651.

(33) Mueller, D. N.; De Souza, R. A.; Weirich, T. E.; Roehrens, D.; Mayer, J.; Martin, M. *Phys. Chem. Chem. Phys.* **2010**, *12*, 10320.

(34) Kriegel, R.; Kircheisen, R. DE 10 2009 050 019 B3, 2011.03.17, 2009.

(35) Tong, J.; Yang, W.; Cai, R.; Zhu, B.; Lin, L. *Catal. Lett.* **2002**, *78*, 129.

(36) Spillman, R. Economics of Gas Separation Membrane Processes. In *Membrane Science and Technology*; Noble, R. D., Stern, S. A., Eds.; Elsevier: New York, 1996; Vol. 2, p 269.

(37) Wang, H. H.; Werth, S.; Schiestel, T.; Caro, J. *Angew. Chem., Int. Ed.* **2005**, *44*, 6906.

(38) Arnold, M.; Xu, Q.; Tichelaar, F. D.; Feldhoff, A. *Chem. Mater.* **2009**, *21*, 635.

(39) Harvey, A. S.; Yang, Z.; Infortuna, A.; Beckel, D.; Purton, J. A.; Gauckler, L. J. *J. Phys.: Condens. Matter* **2009**, *21*, 015801.

(40) Yashima, M., Structural disorder, diffusion pathway of mobile oxide ions, and crystal structure in perovskite-type oxides and related materials. In *Perovskite Oxide for Fuel Cells*, Ishihara, T., Ed.; Springer: Dordrecht, The Netherlands, 2009; p 117.

(41) Goodenough, J. B., Crystalline solid electrolytes II: Materials design. In *Solid State Electrochemistry*; Bruce, P. G., Ed.; Cambridge University Press: Cambridge, U.K., 1995; p 43.

(42) Sun, J. L.; Yang, M.; Li, G. B.; Yang, T.; Liao, F. H.; Wang, Y. X.; Xiong, M.; Lin, J. H. *Inorg. Chem.* **2006**, *45*, 9151.

43

2.3 High-purity oxygen production by a dead-end Ba$_{0.5}$Sr$_{0.5}$Co$_{0.8}$Fe$_{0.2}$O$_{3-\delta}$ tube membrane

Fangyi Liang**,** Heqing Jiang, Huixia Luo, Jürgen Caro and Armin Feldhoff

High-purity oxygen production by a dead-end $Ba_{0.5}Sr_{0.5}Co_{0.8}Fe_{0.2}O_{3-\delta}$ tube membrane

Fangyi Liang[a], Heqing Jiang[b], Huixia Luo[a], Ralf Kriegel[c], Jürgen Caro[a,*]

[a] *Institute of Physical Chemistry and Electrochemistry, Leibniz University Hannover, Callinstr. 3A, D-30167 Hannover, Germany*
[b] *Max-Planck-Institut für Kohlenforschung, Kaiser-Wilhelm-Platz 1, D-45470 Mülheim an der Ruhr, Germany*
[c] *Fraunhofer Institute for Ceramic Technologies and Systems (IKTS), Michael Faraday Str. 1, D-07629 Hermsdorf, Germany*

ARTICLE INFO

ABSTRACT

High-purity oxygen was produced by dead-end $Ba_{0.5}Sr_{0.5}Co_{0.8}Fe_{0.2}O_{3-\delta}$ (BSCF) tube membranes which were sealed by a reaction-diffusion sintering process. First, phase stability of BSCF membrane in a pure oxygen atmosphere – as it is present on the permeate side of the membrane – was studied at 750 and 950 °C, respectively. After the identification of stable operation conditions of BSCF membranes, we studied the oxygen permeation at 950 °C using dead-end BSCF tubes (1 cm outer diameter, 1 mm wall thickness) in (i) a pressure-driven process, (ii) a vacuum process, and (iii) combining both techniques. In all cases, a high oxygen purity of almost 100 vol.% can be obtained at operation temperatures $\geq$ 850 °C. The oxygen permeation flux, the oxygen recovery, and the oxygen ionic conductivity were investigated. It was found that – for the same oxygen partial pressure difference – the oxygen permeation flux in the vacuum process is significantly higher than that in the pressure-driven process at all investigated temperatures. Moreover, in all cases, oxygen permeation and oxygen ionic conductivity can be described by the Wagner theory for bulk diffusion of oxygen ions as rate-limiting step with the logarithmic ratio of the oxygen partial pressures on feed and permeate sides as driving force.

© 2011 Elsevier B.V. All rights reserved.

1. Introduction

About 100 Mio tons of oxygen are produced every year from air by different separation techniques, mostly by cryogenic distillation of air after Linde [1]. Oxygen transporting membranes (OTMs), which can separate oxygen from air or oxygen containing gases with a high purity of theoretically up to 100%, have attracted increasing attention as an alternative to the energy and investment intensive cryogenic distillation. Different operation modes for the oxygen production using OTMs are possible, e.g. the use of condensable recirculating sweep gases like steam [2,3], elevated pressure on the feed side [4], or the use of vacuum pumps on the permeate side [5–9].

Among the OTM materials, the perovskite $Ba_{0.5}Sr_{0.5}Co_{0.8}Fe_{0.2}O_{3-\delta}$ (BSCF) [10–13] is one of the most studied materials for oxygen separation from air [14] and as cathodes in solid-oxide fuel cells due to its high oxygen transport properties [15]. However, for permeation temperatures below 850 °C, stability problems are reported [10,16–19]. To solve the stability problem, Yakovlev et al. recommended, e.g. to stabilize BSCF by bringing Zr

on the B position [20]. Another way to handle the stability problem is to identify stable operation conditions.

Most stability studies are focused on the BSCF membrane material in contact with the fed air. In this paper, we will first study the phase stability of BSCF membrane in a pure oxygen atmosphere as it is present on the permeate side of the membrane. After the identification of stable operation conditions for the BSCF membrane, in the second part of this paper pure oxygen will be produced from air in a dead-end BSCF tube membrane by applying elevated pressure on the feed side and/or vacuum on the permeate side under variation of the permeation parameters.

2. Experimental

The dead-end BSCF tubes with an outer diameter of 10 mm, an inner diameter of 8 mm, and a length of 400 mm (see Fig. 1) were produced by the Fraunhofer Institute IKTS Dresden/Hermsdorf (Germany) [21]. One end of a BSCF tube and one side of a 1 mm thick BSCF disk were grinded to make a flat and even surface. A paste based on copper oxide as sintering aid was screen printed on both grinded surfaces. The screen printed areas were contacted and the tube – standing vertical on the plate – was loaded with a weight of 300 g to support the joining which was carried out by a reaction-diffusion sintering at 980 °C with a dwell time of two hours as described recently [22].

Fig. 1. Dead-end BSCF tube membrane with an outer diameter of 1 cm and 1 mm wall thickness as produced by IKTS.

A dead-end membrane permeator was used for oxygen production as described in detail elsewhere [23]. Synthetic air or oxygen-enriched air at atmospheric or elevated pressures (1–5 bar) was used as feed gases. The flow rates were controlled by gas mass flow controllers (Bronkhorst). High-purity oxygen was produced either at reduced pressure (vacuum process) or at atmospheric pressure of 1 bar (pressure-driven process) on the permeate/core side. The pressures on the feed/shell and permeate/core sides were measured by pressure transducers (Swagelok). In the vacuum process, the reduced pressure was achieved by using a vacuum pump (Pfeiffer vacuum MVP 015-4) realizing a vacuum pressure between 0.08 and 0.12 bar. For quantitative correlation and interpretation, in this paper an average oxygen pressure of 0.1 bar is used as a rough estimate. Oxygen concentrations were analyzed by an online coupled gas chromatograph (Agilent 7890A) equipped with a Carboxen 1000 column. The oxygen permeation flow rate F_{O_2} was directly determined by using a bubble flow meter.

It is assumed that the leaking of nitrogen and oxygen is in accordance with a Knudsen diffusion mechanism. The fluxes of leaked nitrogen and oxygen are related by Eq. (1).

$$D_k = J_{N_2}^{Leak} : J_{O_2}^{Leak} = \sqrt{\frac{32}{28}} \times \frac{C_{N_2}}{C_{O_2}} \qquad (1)$$

where D_k is the Knudsen diffusion factor, C_{O_2}, and C_{N_2} are the oxygen and nitrogen concentrations in the feed gas, respectively.

The oxygen permeation flux J_{O_2} (cm^3 (STP[1]) min^{-1} cm^{-2}) was then calculated by Eq. (2).

$$J_{O_2} = \left(C_{O_2} - \frac{C_{N_2}}{D_k} \right) \times \frac{F}{S} \qquad (2)$$

Here, C_{O_2}, and C_{N_2} are the oxygen and nitrogen concentrations determined by a calibrated gas chromatograph. F is the total flow rate at the outlet on the permeate/core side, and S is the effective surface for permeation.

The oxygen recovery has been calculated by

$$O_{2,recovery} = \frac{F_{O_2}}{F_{air,inlet} \cdot C_{O_2}} \qquad (3)$$

with F_{O_2} as oxygen permeation flow rate, C_{O_2} the oxygen concentration in vol.% and $F_{air,inlet}$ as air flow rate at the inlet of the feed/shell side.

Simulating the exposure of the BSCF material to pure oxygen as it takes place on the permeate/core side of the membrane, pure
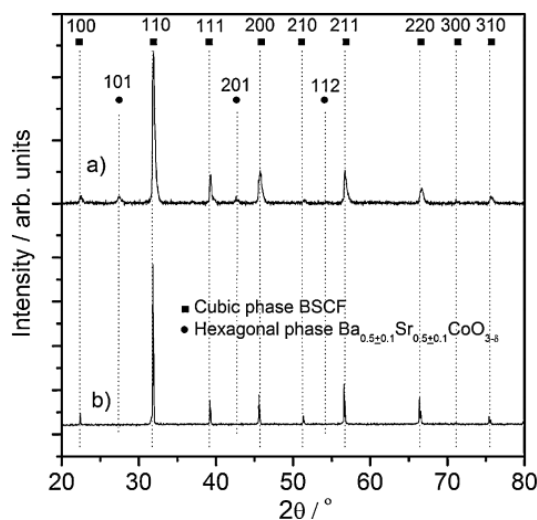
---

[1] STP = standard temperature and pressure.

Fig. 2. XRD patterns of the BSCF membranes after exposed to 100% oxygen for 5 days at (a) 750 °C and (b) 950 °C. The Bragg positions correspond to cubic perovskite with $a = 0.398$ nm. The reflections of hexagonal phase Ba$_{0.5\pm0.1}$Sr$_{0.5\pm0.1}$CoO$_{3-\delta}$ correspond to the (1 0 1), (2 0 1), (1 1 2) planes. Near to the BSCF perovskite peaks, in (b) there are other non-identified peaks that can belong to the iron-enriched BSCF phase which is formed during the partial decomposition of the bulk cubic BSCF phase into hexagonal Ba$_{0.5\pm0.1}$Sr$_{0.5\pm0.1}$CoO$_{3-\delta}$.

oxygen with a flux of 30 ml (STP)/min was sent through a fixed bed of BSCF membrane pieces inside an alumina tube for 5 days at 750 °C and 950 °C, respectively.

The XRD data were collected in a $\theta/2\theta$ geometry on a Bruker D8 Advance instrument with monochromatic Cu K$_\alpha$ radiation at 40 kV and 40 mA and a receiving slit of 0.05 mm using a step-scan mode in the 2θ range of 20–80° with intervals of 0.02. Scanning electron microscopy (SEM) was performed with a JEOL JSM-6700F at a low excitation voltage of 2 kV for imaging with secondary electrons.

3. Results and discussion

Fig. 2 shows the XRD patterns of the BSCF membranes treated at 750 °C and 950 °C, respectively, for 5 days in pure oxygen. If BSCF is exposed to pure oxygen at 750 °C, in addition to the cubic BSCF phase, a second phase was found and could be identified as a hexagonal perovskite of the composition Ba$_{0.5\pm0.1}$Sr$_{0.5\pm0.1}$CoO$_{3-\delta}$ (Fig. 2a) as described in detail in our previous study [23]. A transformation of the cubic BSCF into the hexagonal perovskite was also found by Švarcová et al. [18] after treating the BSCF powder in pure oxygen at 800–850 °C. The formation of the hexagonal phase is ascribed to a partial decomposition of the bulk cubic BSCF perovskite in an intermediate temperature range (500–850 °C). Rebeilleau-Dassonneville et al. [16], Efimov et al. [19], and Müller et al. [24] have observed the same additional reflections (28° and 42.5° 2θ) of a new phase in the XRD pattern after treating the BSCF powder in air at intermediate temperatures. However, no phase transition was observed, if the BSCF membrane was treated at 950 °C for 5 days in pure oxygen (see Fig. 2b).

The SEM images of the BSCF membrane before and after treatment for 5 days in pure oxygen at 750 °C and 950 °C are given in Fig. 3. On the surface of the un-tested BSCF membrane (Fig. 3a) unidentified nanoparticles decorating the terraces were found. The BSCF tubes were sintered in their production process at 1130 °C in air with a cooling rate of 2 K/min. From energy dispersive X-ray spectroscopy (EDXS) we found that these particles are Co-enriched.

Fig. 4. Influence of the flow rate of the fed air (20 vol.% O_2) on oxygen recovery and oxygen permeation flux for two feed pressures at 950 °C. Feed side: air at 1 bar (■,□) and 5 bar (●,○) with different flow rates. Permeate side: pure O_2 at 0.1 bar (fluctuating between 0.08 and 0.12 bar).
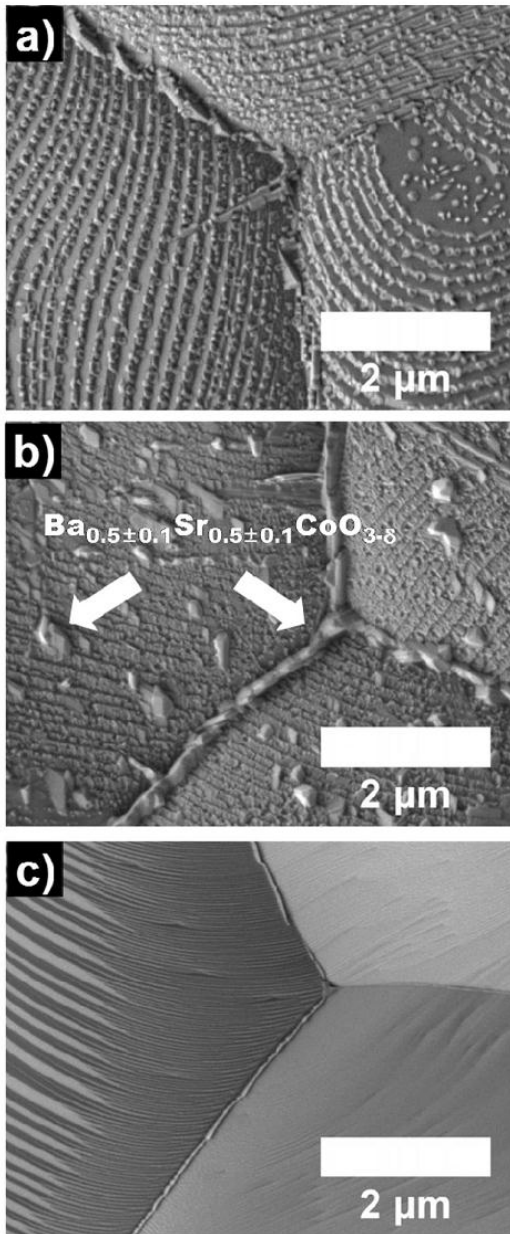

Fig. 3. Microstructures of the BSCF perovskite tube membrane (a) before and after treating in 100% oxygen for 5 days at (b) 750 °C, and (c) 950 °C. For the XRD patterns, see Fig. 2. White arrows in (b) mark the phase of hexagonal perovskite $Ba_{0.5\pm0.1}Sr_{0.5\pm0.1}CoO_{3-\delta}$ [23].

As shown in Fig. 3b, some new island-like particles appear on the surface and in the grain boundaries of BSCF membrane treated at 750 °C. In accordance with our previous finding [23], these particles in the grain boundaries are identified by XRD (see Fig. 2a) as hexagonal perovskite $Ba_{0.5\pm0.1}Sr_{0.5\pm0.1}CoO_{3-\delta}$. However, no additional phase formation was observed when treating the BSCF membrane in pure oxygen at 950 °C (see Fig. 3c). It can be seen in Fig. 3c that the surface of the BSCF membrane is smooth and free of the nanoparticles that were found in Fig. 3a on terraces and in Fig. 3b in
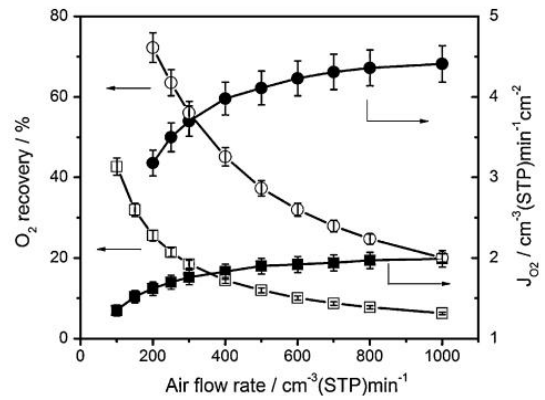
grain boundaries. Thus, it can be concluded that the decomposition of BSCF forming the hexagonal perovskite phase is suppressed at high temperatures and at high oxygen partial pressure which is in accordance with a previous finding [25]. Furthermore, the nanoparticles decorating the terraces (see Fig. 3a) were either evaporated or consumed by the bulk. Shao et al. [10] and van Veen et al. [26] also reported that a stable oxygen permeation of BSCF perovskite membrane can be only achieved if the operation temperatures are higher than 850 °C [10,16–19]. As stated above, in a previous study we found that the oxygen permeation flux decreases with time at a permeation temperature of 750 °C due to the decomposition of the bulk cubic perovskite phase into a hexagonal perovskite $Ba_{0.5\pm01}Sr_{0.5\pm0.1}CoO_{3-\delta}$ and a trigonal Co-enriched mixed oxide $Ba_{1-x}Sr_xCo_{2-y}Fe_yO_{3-\delta}$ [23]. Therefore, in this paper the oxygen permeation was mainly investigated at the high temperature of 950 °C.

Oxygen permeation flux and oxygen recovery are two important parameters for a large-scale oxygen production. The oxygen recovery can be adjusted by the air flow rate and the air pressure. Fig. 4 shows the influence of the air flow rate and the air pressure on the oxygen recovery and the oxygen permeation flux at 950 °C. At the same air pressure, the oxygen recovery decreases with increasing air flow rate, whereas the oxygen permeation fluxes increase with increasing air flow rate. It was found (Fig. 4) that the oxygen permeation flux increased steeply up to an air flow rate of 500 cm³ (STP) min⁻¹, whereas a further increase of the air flow rate only slightly enhances the oxygen permeation flux. Accordingly, a compromise between the oxygen permeation flux and the oxygen recovery can be achieved by adjusting the air flow rate. At the same air flow rate, oxygen recovery and oxygen permeation flux increase with increasing the air pressure. For example, at the air flow rate of 500 cm³ (STP) min⁻¹, the oxygen permeation flux increases from 1.9 to 4.1 cm³ (STP) cm⁻² min⁻¹, while the oxygen recovery increases from 12% to 37% with increasing the air pressure from 1 to 5 bar.

If the oxygen partial pressure on the two sides of an OTM is different, an oxygen flux across the OTM can be observed. In the case that oxygen ion bulk diffusion rather than surface processes are rate limiting, the oxygen permeation flux J_{O_2} can be expressed by the Wagner equation [27]

$$J_{O_2} = -\frac{RT}{4^2F^2L}\int_{\ln P_2}^{\ln P_1} \frac{\sigma_i \cdot \sigma_e}{\sigma_i + \sigma_e}\,d\ln P_{O_2} \qquad (4)$$
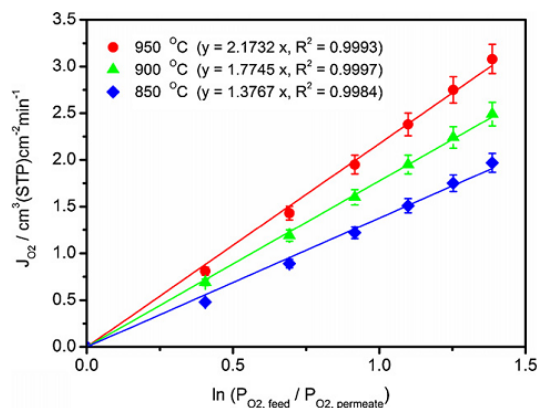
Fig. 5. Oxygen permeation rate as a logarithmic function of the oxygen partial pressure ratio on the feed and permeate sides at different temperatures for the pressure-driven process. Feed side: air flow rate = 500 cm³ (STP) min⁻¹ at different oxygen partial pressure differences. Permeate side: pure O_2 at 1 bar.

Fig. 6. Calculated oxygen ionic conductivity as a function of temperature at different oxygen partial pressures on the feed and permeate sides for the pressure-driven process (from Fig. 5).

where σ_e and σ_i are the electronic and ionic conductivities, respectively. R, F, T, and L denote the gas constant; Faraday constant; temperature; and thickness of the membrane, respectively [28]. P_1 and P_2 are the oxygen partial pressures on permeate side and feed side, respectively. Integration of Eq. (4) for assuming $\sigma_e \gg \sigma_i$ and constant σ_i gives [28]

$$J_{O_2} = -\frac{RT\sigma_i}{4^2 F^2 L}\ln\frac{P_1}{P_2} \tag{5}$$

It is interesting to note that the pressure dependence of the oxygen fluxes as shown in Fig. 4 can be explained by the Wagner concept according to Eq. (5) with the logarithm of the oxygen partial pressures across the membrane as the driving force. In the pressure-driven process with 5 bar and 1 bar air on the feed side and pure oxygen at about 0.1 bar on the permeate side, the logarithms of the ratio of the oxygen partial pressures $\ln(P_1/P_2)$ gives 2.3. In accordance with this prediction, the ratio of the oxygen fluxes at the feed pressures of 5 and 1 bar with a constant permeate pressure of about 0.1 was found to be 2.2 (cf. Fig. 4), which is comparable with the prediction from the Wagner theory.

When the pressure on the permeate side is fixed at 1 bar, pure oxygen can be obtained at atmospheric pressure, if the oxygen partial pressure difference across the membrane is higher than 1 bar. The oxygen partial pressure ratio can be increased by elevating the pressure of atmospheric air with 21 vol.% O_2 or by using O_2-enriched air. O_2-enriched air of different oxygen content can be produced by using either organic polymeric hollow-fiber membranes [29] or perovskite hollow fiber membranes [7,30]. Fig. 5 shows the oxygen permeation rate as a logarithmic function of the oxygen partial pressure ratio representing the driving force of the process. The oxygen partial pressure difference was established by elevating the pressure of the O_2-enriched air with 50 vol.% oxygen as feed. For example, an oxygen partial pressure difference of 1.0 bar across the membrane can be established by using compressed oxygen-enriched air with 50 vol.% oxygen at 4 bar on the feed side while keeping the permeated oxygen at 1 bar. It was found, that the oxygen permeation fluxes at all temperatures increase linearly as logarithmic function of the oxygen partial pressure ratio which is in agreement with the Wagner theory (see Eq. (5)) assuming that the oxygen transport is limited by oxygen ion bulk diffusion. Similar results have been published recently for BSCF membranes [31].
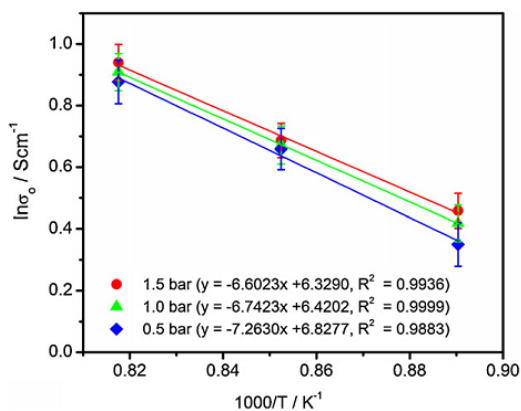
According to the Wagner theory (Eq. (5)), the oxygen ionic conductivity at various oxygen partial pressure ratios and temperatures can be calculated by Eq. (6):

$$\sigma_i = -J_{O_2}\frac{4^2 F^2 L}{RT}\left(\ln\frac{P_1}{P_2}\right)^{-1} \tag{6}$$

Fig. 6 shows the calculated oxygen ionic conductivity as a function of temperature at different oxygen partial pressures on the feed and permeate sides for the pressure-driven process (Fig. 5). It can be found from Fig. 6 that the oxygen ionic conductivity increases linearly with increasing the reciprocal temperature which is in agreement with the prediction from the Wagner theory (see Eq. (6)) for bulk diffusion of oxygen ions as rate-limiting step. Moreover, the oxygen ionic conductivity increases also with increasing the oxygen partial pressure difference between the feed and permeate sides. The oxygen ionic conductivity of the dead-end BSCF tube at 900 °C is ca 1.9 S cm⁻¹. A similar value of an oxygen ionic conductivity of ca 1.4 S cm⁻¹ was reported by Chen et al. [32] for a 1.1 mm thick BSCF disk membrane at 900 °C.
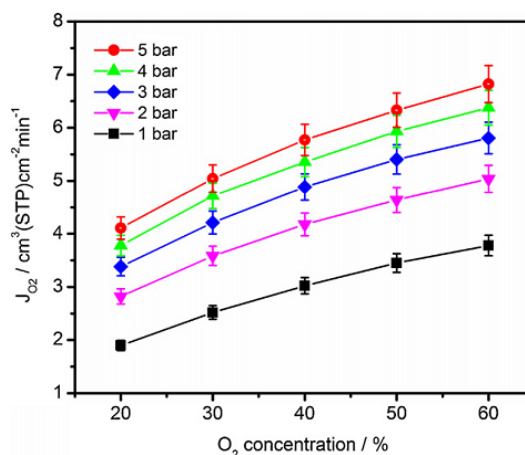

Fig. 7. Influence of oxygen concentration in the fed air on the production of oxygen for different feed pressures at 950 °C in the vacuum process. Feed side: O_2-enriched air flow rate = 500 cm³ (STP) min⁻¹. Permeate side: pure O_2 at 0.1 bar (fluctuating between 0.08 and 0.12 bar).
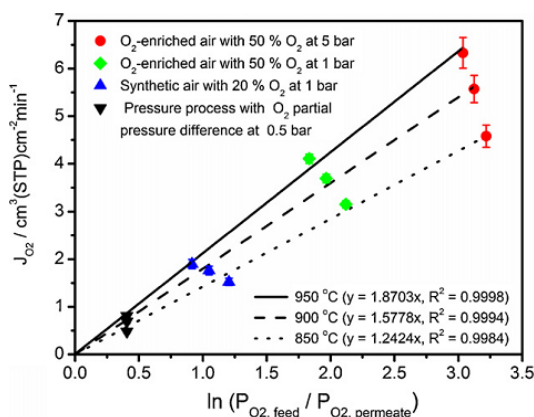
Fig. 8. The oxygen permeation fluxes in the vacuum and pressure-driven processes as function of the logarithm of the partial pressure ratios on feed and permeate sides from 850 to 950 °C. Permeate side: pure oxygen at 0.1 bar (fluctuating between 0.08 and 0.12 bar) by using a vacuum pump or 1 bar in the pressure-driven process. Feed side: air gas flow rate = 500 cm^3 (STP) min^{-1}.

Fig. 9. Oxygen permeation fluxes as function of oxygen partial pressure difference in the vacuum and pressure-driven processes at 950 °C. Permeate side: pure oxygen at reduced pressure of 0.1 bar (fluctuating between 0.08 and 0.12 bar) using a vacuum pump or 1 bar in the pressure-driven process. Feed side: feed gas flow rate = 500 cm^3 (STP) min^{-1} with 50 vol.% O$_2$ at different pressures.

Fig. 7 shows the influence of the oxygen concentration in the fed air on the oxygen production at different feed pressures at 950 °C. It was found that the oxygen permeation fluxes increase with both increasing the oxygen concentration in the fed air and the feed pressure, suggesting that any increase of the oxygen concentration in the fed air has the same effect as increasing the feed pressure. It can be expected from Wagner's theory that the oxygen permeation flux increases with the feed pressure, but the corresponding incremental growth for a stepwise increase of the feed pressure drops for a constant pressure step with increasing absolute pressure. For example, the same pressure difference of 1 bar from 1 to 2 bar and from 4 to 5 bar between feed and permeate, gives the different oxygen permeation fluxes of 0.9 cm^3 (STP) cm^{-2} min^{-1} and 0.3 cm^3 (STP) cm^{-2} min^{-1}. Wang et al. reported that the oxygen permeation flux can be increased by elevating the air pressure until 50 atm [33]. The compression cost in the pressure-driven process can have a negative impact on the economics. However, the same holds true for the production of oxygen-enriched air as feed. On the other hand, the space-time yield of the permeator in the production of oxygen will increase. It has to be noted that a high feed pressure can be problematic in practice due to, e.g. the mechanical stability, and the sealing of the membranes. Therefore, a relative low pressure on the feed side is desired, and the oxygen permeation flux can be raised by using oxygen-enriched air as feed. For example, the oxygen permeation flux increases from 4.1 to 6.8 cm^3 (STP) cm^{-2} min^{-1} when increasing the oxygen concentration in the fed O$_2$-enriched air from 20 to 60 vol.% at 5 bar and 950 °C (Fig. 7).

Similar like Fig. 5 for the pressure-driven process, Fig. 8 shows the oxygen permeation fluxes in the vacuum and pressure-driven processes as function of the logarithm of the oxygen partial pressure ratios on the feed and permeate sides from 850 to 950 °C. The straight lines of F_{O_2} vs. ln($P_{O_2,\text{feed}}/P_{O_2,\text{permeate}}$) for all temperatures indicate again, that oxygen permeation can be described well by the Wagner theory (Eq. (5)) for oxygen ion diffusion in the bulk as rate-limiting step. In a recent paper by Kovalevsky et al. [34] the role of surface oxygen exchange on oxygen permeation through a BSCF membrane was studied and corresponding O$_2$ flux limitations were expected for a membrane thickness below 1 mm.

It can be found from Fig. 8 that a higher oxygen permeation flux was obtained in the vacuum process using the synthetic air with 20 v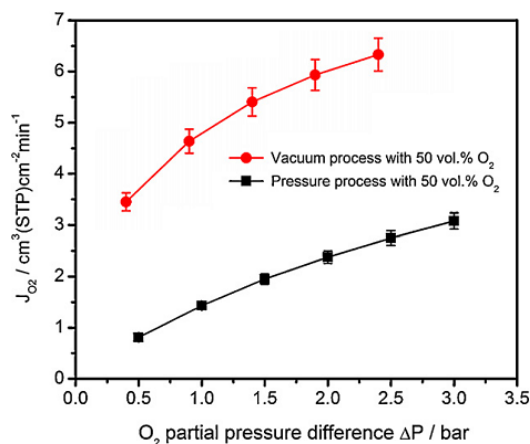ol.% oxygen at 1 bar as feed gas compared to the pressure-driven process with an oxygen partial pressure difference of 0.5 bar (air with 50 vol.% oxygen at 3 bar on the feed side, oxygen pressure of 1 bar on the permeate side). Moreover, in the vacuum process, the oxygen permeation fluxes can be significantly enhanced when raising the oxygen concentration in the feed from 20 to 50 vol.%. In addition, in a combination of both the vacuum and the pressure-driven process, the oxygen permeation fluxes can be further enhanced by using oxygen enriched air with 50 vol.% oxygen.

Fig. 9 shows the dependence of the oxygen permeation flux on the oxygen partial pressure difference at 950 °C when using 50 vol.% O$_2$-enriched air as feed gas. If the oxygen pressure on the permeate side is fixed (at 0.1 bar or 1 bar), the oxygen partial pressure difference across the membrane can be adjusted by the feed pressure and oxygen content of the fed gas. For the same oxygen partial pressure difference, the oxygen permeation flux in the vacuum process is significantly higher than that in the pressure-driven process. This experimental finding can be explained again by the Wagner theory since the oxygen permeation flux J_{O_2} is proportional to the logarithmic ratio of the oxygen partial pressures P_1 and P_2 on feed and permeate side if all other conditions are fixed. As an example, a higher oxygen permeation flux can be obtained for the oxygen partial pressure difference of 0.5 bar in the vacuum process with the driving force (ln(0.6/0.1)) than for the oxygen partial pressure difference of 3.0 bar in the pressure-driven process with the driving force (ln(3/1)). Here, our experimental results of high-purity oxygen production is in good agreement with the straightforward process analysis by Tan and Li [9] and Kriegel et al. [8] showing that the vacuum operation is more economical to produce oxygen from air compared to the pressure operation and a membrane process using a sweep gas. However, Tan and Li [9] reported that a relative leakage of 44% existed in the oxygen production with the vacuum operation using La$_{0.6}$Sr$_{0.4}$Co$_{0.2}$Fe$_{0.8}$O$_{3-\delta}$ at 1180 °C.

Due to the difficulties in sealing the membrane at high temperatures, there are only a few reports on the separation of pure oxygen by using OTMs. In this work, a high oxygen purity of almost 100 vol.% (gas chromatography does not detect any N$_2$) was found at operation temperatures ≥ 850 °C. The high oxygen purity indicates that the BSCF tube and the BSCF disk forming the dead-end part of the membrane has been sealed perfectly. Moreover, the open side of the dead-end tube membranes was simply sealed by

silicone rubber rings outside the high-temperature zone. Therefore, the dead-end tube membranes geometry can solve the problem of the high-temperature sealing.

4. Conclusions

To identify stable operation conditions for a BSCF membrane in the high-purity oxygen production, the stability of the BSCF membranes was tested in pure oxygen at 950 °C and 750 °C – as it is the case on the permeate side in high-purity oxygen production. A secondary phase of a hexagonal perovskite $Ba_{0.5\pm0.1}Sr_{0.5\pm0.1}CoO_{3-\delta}$ forms from the cubic BSCF after treatment in pure oxygen at 750 °C. However, no phase transformation was found by treating BSCF at 950 °C in a pure oxygen atmosphere.

Good BSCF stability was found when the BSCF membrane was operated at temperatures ≥ 850 °C and oxygen with a purity of almost 100 vol.% was obtained. Oxygen recovery increases with increasing air pressure, but decreases with increasing air flow rate. Oxygen permeation flux and space-time yield of the high-purity oxygen production can be raised using oxygen-enriched air as feed at relatively low feed pressure of a few bar. The oxygen ionic conductivity increases with increasing temperature and the natural logarithm of the oxygen partial pressures ratio of the feed to permeate sides. The oxygen permeability and the oxygen ionic conductivity of BSCF tube membrane can be well explained by Wagner's theory for oxygen ion bulk diffusion as rate-limiting step.

Oxygen permeability was measured for the pressure-driven process (air at up to 5 bar as feed gas, pure oxygen at 1 bar as permeate) and for the vacuum process (permeated oxygen at reduced pressure of 0.1 bar) as well as for combining both techniques. For the same oxygen partial pressure difference, the oxygen permeation flux in the vacuum process is significantly higher than that in the pressure-driven process. This finding is in complete agreement with Wagner theory indicating that the oxygen flux is proportional to the logarithm of the oxygen partial pressure ratio on feed and permeate sides. Nevertheless, limitations of the oxygen flux by the surface exchange can be expected for asymmetric membranes, hollow fibers or capillaries with lower wall thickness.

Acknowledgements

References

[1] J. Ermsley, Oxygen, Nature's Building Blocks: An A–Z Guide to the Elements, Oxford University Press, Oxford, England (UK), 2001.
[2] H.H. Wang, P. Kölsch, T. Schiestel, C. Tablet, S. Werth, J. Caro, J. Membr. Sci. 284 (2006) 5.
[3] A. Leo, S.M. Liu, J.C.D. da Costa, Sep. Purif. Technol. 78 (2011) 220.
[4] W. Ito, T. Nagai, T. Sakon, Solid State Ionics 178 (2007) 809.
[5] X.F. Zhu, S.M. Sun, Y. Cong, W.S. Yang, J. Membr. Sci. 345 (2009) 47.
[6] X.Y. Tan, Z.G. Wang, B. Meng, X.X. Meng, K. Li, J. Membr. Sci. 352 (2010) 189.
[7] F.Y. Liang, H.Q. Jiang, T. Schiestel, J. Caro, Ind. Eng. Chem. Res. 49 (2010) 9377.
[8] R. Kriegel, W. Burckhardt, I. Voigt, M. Schulz, E. Sommer, Proc. 10. ICIM, Tokyo, Japan, 18–22.08.2008.
[9] X.Y. Tan, K. Li, AIChE J. 53 (2007) 838.
[10] Z.P. Shao, W.S. Yang, Y. Cong, H. Dong, J.H. Tong, G.X. Xiong, J. Membr. Sci. 172 (2000) 177.
[11] H. Lu, J.H. Tong, Y. Cong, W.S. Yang, Catal. Today 104 (2005) 154.
[12] H.H. Wang, C. Tablet, A. Feldhoff, J. Caro, J. Membr. Sci. 262 (2005) 20.
[13] J.F. Vente, S. McIntosh, W.G. Haije, H.J.M. Bouwmeester, J. Solid State Electrochem. 10 (2006) 581.
[14] J. Sunarso, S. Baumann, J.M. Serra, W.A. Meulenberg, S. Liu, Y.S. Lin, J.C.D. da Costa, J. Membr. Sci. 320 (2008) 13.
[15] Z.P. Shao, S.M. Haile, Nature 431 (2004) 170.
[16] M. Rebeilleau-Dassonneville, S. Rosini, A.C. van Veen, D. Farrusseng, C. Mirodatos, Catal. Today 104 (2005) 131.
[17] M. Arnold, T.M. Gesing, J. Martynczuk, A. Feldhoff, Chem. Mater. 20 (2008) 5851.
[18] S. Švarcová, K. Wiik, J. Tolchard, H.J.M. Bouwmeester, T. Grande, Solid State Ionics 178 (2008) 1787.
[19] K. Efimov, Q.A. Xu, A. Feldhoff, Chem. Mater. 22 (2010) 5866.
[20] S. Yakovlev, C.Y. Yoo, S. Fang, H.J.M. Bouwmeester, Appl. Phys. Lett. 96 (2010) 254101.
[21] I. Voigt, U. Pippardt, W. Burckhardt, R. Kriegel, M. Schulz, E. Sommer, W. Reuner, M. Kanis, 11. Aachener Membrankolloquium 28–29 March 2007.
[22] R. Kriegel, R. Kircheisen, K. Ritter, Patent: DE 10 2009 050 019 B3, 2011.03.17, 2009.
[23] F.Y. Liang, H.Q. Jiang, H.X. Luo, J. Caro, A. Feldhoff, Chem. Mater. 23 (2011) 4765.
[24] P. Müller, H. Störmer, L. Dieterle, C. Niedrig, E. Ivers-Tiffée, D. Gerthsen, Solid State Ionics 206 (2012) 57.
[25] R. Kriegel, R. Kircheisen, J. Töpfer, Solid State Ionics 181 (2010) 64.
[26] A.C. van Veen, M. Rebeilleau, D. Farrusseng, C. Mirodatos, Chem. Commun. (2003) 32.
[27] C. Wagner, Prog. Solid State Chem. 10 (1975) 3.
[28] C.H. Chen, H.J.M. Bouwmeester, R.H.E. vanDoorn, H. Kruidhof, A.J. Burggraaf, Solid State Ionics 98 (1997) 7.
[29] R. Spillman, in: R.D. Noble, S.A. Stern (Eds.), Membrane Science and Technology, vol. 2, Elsevier, New York, 1996, p. 269.
[30] H.H. Wang, S. Werth, T. Schiestel, J. Caro, Angew. Chem. Int. Ed. 44 (2005) 6906.
[31] R. Kriegel, in: J. Kriegesmann (Ed.), Handbuch Technische Keramische Werkstoffe, HvB-Verlag Ellerau, 119, Chapter 8.10.1.1, 2010, p. 1.
[32] Z. Chen, Z. Shao, R. Ran, W. Zhou, P. Zeng, S. Liu, J. Membr. Sci. 300 (2007) 182.
[33] H.H. Wang, R. Wang, D.T. Liang, W.S. Yang, J. Membr. Sci. 243 (2004) 405.
[34] A.V. Kovalevsky, A.A. Yaremchenko, V.A. Kolotygin, A.L. Shaula, V.V. Kharton, F.M.M. Snijkers, A. Buekenhoudt, J.R. Frade, E.N. Naumovich, J. Membr. Sci. 380 (2011) 68.

3 High-purity oxygen production using perovskite hollow fiber membranes

3.1 Summary

Oxygen transporting membranes can be produced in different geometries by different technologies. Usually, the conventional disc membranes are applied for the evaluation of the oxygen permeation flux through a perovskite membrane. However, because of low oxygen fluxes due to the membrane thickness and limited area, the conventional disc membranes are not suitable for practical application. Tubular membranes were developed to reduce the engineering difficulties, especially the problem of the high temperature sealing. However, their small membrane area per unit volume and relatively thick wall limit them in practical application. A hollow fiber membrane with a thin wall can solve the above problem. By keeping the two sealed ends outside the high temperature zone, polymer O-rings can be used for sealing. Compared to the conventional disk and tubular membranes, hollow fiber membranes give very high values of the membrane area per unit permeator/reactor volume. Furthermore, due to the thin wall, the materials costs of the hollow fiber membranes are reduced.

In this chapter, the production of pure oxygen and O_2-enriched air were studied by using $BaCo_xFe_yZr_{1-x-y}O_{3-\delta}$ (BCFZ) hollow fiber membranes. In a first step, O_2-enriched air with an oxygen concentration of 30-50 vol.% is produced in a flow-through permeator from 1 bar of air as feed applying a vacuum pump to keep the pressure on the O_2-enriched air side at about 0.12 bar. This O_2-enriched air was used as pressurized feed for the production of pure oxygen. In a second step, pure oxygen is produced in a dead-end permeator using (i) pressurized air/O_2-enriched air as feed, (ii) reduced pressure on the permeate side, and (iii) a combination of both. For the effective production of oxygen with a high space-time-yield, a two-step-process is proposed. The oxygen permeation fluxes increase with increasing temperature, pressure on the feed side, and oxygen concentration in the fed O_2-enriched air. An oxygen permeation flux of 10.2 $cm^3(STP)$ $cm^{-2}min^{-1}$ was reached using O_2-enriched air with 50 vol.% O_2 at 5 bar as feed and reduced pressure of 0.05 bar on the permeate side at 900 °C. The reliability of the perovskite hollow fiber membrane was tested for 150 h under the conditions of 0.05 bar on permeate side and an elevated pressure on the feed side at 900 °C. A high oxygen purity up to 99.9 vol.% and an oxygen permeation flux of 9.7 $cm^3(STP)cm^{-2}min^{-1}$ were obtained during 150 h operation.

3.2 High-purity oxygen production using perovskite hollow fiber membranes

Fangyi Liang, Heqing Jiang, Thomas Schiestel and Jürgen Caro

Industrial & Engineering Chemistry Research 2010, 49, 9377.

High-Purity Oxygen Production from Air Using Perovskite Hollow Fiber Membranes

Fangyi Liang,[†] Heqing Jiang,[†] Thomas Schiestel,[‡] and Jürgen Caro*,[†]

Institute of Physical Chemistry and Electrochemistry, Leibniz University of Hannover, Callinstrasse 3A, D-30167 Hannover, Germany, and Fraunhofer Institute of Interfacial Engineering and Biotechnology (IGB), Nobelstrasse 12, D-70569 Stuttgart, Germany

The production of O_2-enriched air and of high-purity oxygen was studied in a flow-through and in a dead-end permeator with $BaCo_xFe_yZr_{1-x-y}O_{3-\delta}$ (BCFZ) hollow fiber membranes at high temperatures using (i) pressurized air/O_2-enriched air as feed, (ii) reduced pressure on the permeate side, and (iii) a combination of both. For the effective production of oxygen with a high space-time yield, a two-step process is proposed. In a first step, O_2-enriched air with an oxygen concentration of 30−50 vol % is produced in a flow-through permeator from 1 bar of air as feed applying a vacuum pump to keep the pressure on the O_2-enriched air side at about 0.12 bar. In a second step, pure oxygen is produced in a dead-end permeator using the O_2-enriched air from step 1 as pressurized feed and using again a vacuum pump to establish a reduced oxygen pressure of about 0.05 bar on the permeate side. The oxygen permeation fluxes increase with increasing temperature, pressure on the feed side, and oxygen concentration in the fed O_2-enriched air. An oxygen permeation flux of 10.2 cm^3 (STP) cm^{-2} min^{-1} was reached using O_2-enriched air with 50 vol % O_2 at 5 bar as feed and reduced pressure of 0.05 bar on the permeate side at 900 °C. A high oxygen purity up to 99.9 vol % and high permeation rates of almost 10 cm^3 (STP) cm^{-2} min^{-1} were obtained at 900 °C in a 150 h operation under the conditions of 0.05 bar on the oxygen side and oxygen-enriched air at 4 bar on the feed side.

1. Introduction

Depending on the amount and the purity of oxygen needed, several techniques are available to separate oxygen from air. The cryogenic fractionation technology after Linde can produce pure oxygen with oxygen concentration >99 vol %. Pressure swing adsorption (PSA)[1] can give oxygen with a purity of up to 95−97 vol %. The membrane technology is also used for air-to-oxygen production. Because of the low separation factor, the oxygen enrichment of polymeric membranes[2] is of the order of around 50 vol %.

Dense perovskite ceramic membranes with mixed oxygen−ionic and electronic conductivity[3−7] provide a promising way for oxygen production. At high temperatures, oxygen can permeate through the membrane from the high to low oxygen partial pressure side. Theoretically, the permselectivity of oxygen is infinite. These ceramic membranes also can find potential applications in membrane reactors for the partial oxidation of methane (POM) to synthesis gas,[8] the selective oxidative dehydrogenation of light hydrocarbons to olefins,[9] and the hydrogen production by water splitting.[10−12]

Usually, for the evaluation of the oxygen permeation flux through a perovskite membrane, inert sweep gases like He or Ar are applied to reduce the oxygen partial pressure on the permeate side of the membrane,[13−15] while having air (oxygen partial pressure, $P_{O_2} \approx 0.21$ bar) as feed. However, this method of using sweep gases is not suitable for an industrial oxygen production because of the need of a subsequent separation of oxygen from the sweep gas.

When using a perovskite material as membrane, pure oxygen (theoretically up to 100%) can be obtained at atmospheric pressure if the oxygen partial pressure of the compressed air is higher than 1 bar,[16] by pumping off the permeated oxygen from the permeation side, by combining both techniques,[17] or by using steam as condensable sweep gas.[18]

If oxygen is produced with relatively thick disk perovskite membranes, the complicated high-temperature sealing has to be solved, and only low oxygen fluxes are obtained due to the membrane thickness and limited area. Tubular membranes were developed to reduce the engineering difficulties, especially the problem of the high temperature sealing. However, their small membrane area per unit volume and relatively thick wall limit them in practical application. A hollow fiber membrane with a thin wall can solve the above problem. By keeping the two sealed ends outside the high temperature zone, polymer O-rings can be used. As compared to the conventional disk and tubular membranes, hollow fiber membranes give very high values of the membrane area per unit volume. Furthermore, due to the thin wall, the material costs of the hollow fiber membrane are reduced.

Recently, the perovskite with the composition of $BaCo_xFe_yZr_{1-x-y}O_{3-\delta}$ (BCFZ)[19] was developed as hollow fiber[20] with high oxygen permeability and has been evaluated in oxygen separation from air,[20] partial oxidation of hydrocarbons,[21] and the decomposition of nitrogen oxides.[22,23] In a previous paper, we have already reported some results on the production of O_2-enriched air using these BCFZ hollow fiber membranes.[24] O_2-enriched air can be used in many industrial processes, such as methane combustion at high temperatures, the synthesis of ammonia, the Claus process, steel plants, and waste burning.[25] In this work, O_2-enriched air and pure oxygen were produced in a flow-through and a dead-end BCFZ membrane permeator, respectively. To obtain a high oxygen permeation flux and thus a high space-time yield, a large oxygen partial pressure gradient across the membrane is required, which can be achieved by increasing the air pressure on the feed side, by using O_2-enriched air as feed, or by applying reduced pressure on the permeate side.

* To whom correspondence should be addressed. E-mail: juergen.caro@pci.uni-hannover.de.
† Leibniz University of Hannover.
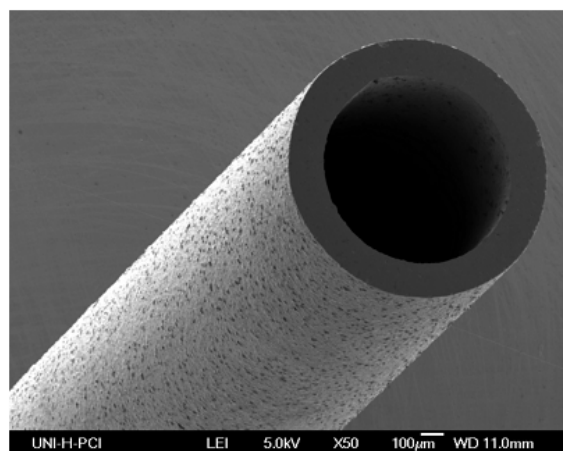‡ Fraunhofer Institute of Interfacial Engineering and Biotechnology.

Figure 1. SEM micrograph of the dense BCFZ hollow fiber membrane produced by a spinning technique[20] after sintering.

2. Experimental Section

Dense BCFZ perovskite hollow fiber membranes were manufactured by a phase inversion spinning process followed by high-temperature sintering at 1320 °C.[20] A simple hydrolysis of the corresponding metal nitrates by an ammonium hydroxide solution was applied to get the precursor BCFZ material. The precursor was mixed with a solution of polysulfone in 1-methyl-2-pyrrolidone and was ball-milled for 16 h.[20] As shown in Figure 1, the sintered fiber has a thickness of around 0.17 mm with outer diameter of 1.10 mm and inner diameter of 0.76 mm. Figure 2 shows schematically the flow-through membrane permeator 1 used for the production of O_2-enriched air. The fibers used here had a length of 30 cm. The two ends of the BCFZ hollow fiber membrane were sealed by two silicone rubber rings outside the oven. Synthetic air (O_2 concentration 20 vol %) was fed to the shell side, and another flow of synthetic air was sent through the core side at different flow rates (25−75 cm^3 min^{-1}). The reduced pressure on the core/permeate side of the hollow fiber membrane was kept at about 0.12 bar by connection to an oil-free diaphragm vacuum pump (Pfeiffer vacuum MVP 015-4). Because of the difference in the oxygen partial pressure between shell and core side, oxygen from the shell side permeates through the hollow fiber membrane to the core side and mixes there with air, thus forming O_2-enriched air.

Figure 3 presents the dead-end membrane permeator 2 used for the production of pure oxygen. The dead-end hollow fiber membrane is obtained by sealing one end of the BCFZ hollow fiber with a gold plug using Au paste (Hereaus, sintering the gold paste at 950 °C to make it gastight). The dead-end BCFZ hollow fiber was coated by dense gold film (Au paste from Hereaus, sintering the Au layer at 950 °C to obtain the dense gold film that is not permeable to oxygen) except for the 3 cm part close to the end with a gold plug. The uncoated part (3 cm, effective membrane area: 0.86 cm^2) of the hollow fiber was put in the middle of the oven, thus ensuring isothermal conditions (cf., Figure 3). Synthetic air or oxygen-enriched air at atmospheric or elevated pressures (1−5 bar) was fed to the shell/feed side. On the core side, high-purity oxygen was produced at about 0.05 bar. This reduced pressure on the core side was achieved with a vacuum pump (Pfeiffer vacuum MVP 015-4).

All gas concentrations were determined by an online coupled gas chromatograph (Agilent 7890A). The flow rates were controlled by gas mass flow controllers (Bronkhorst). The flow

rates were regularly calibrated by using a simple bubble flow meter. The O_2 permeation rate J_{O_2} (cm^3 min^{-1} cm^{-2}) can be calculated by eq 1 in which $F_{air,inlet}$ (cm^3 min^{-1}) is the air flow rate at the inlet to the feed side; C_{O_2} (vol %) is the O_2 concentration at the outlet of the core side, which can be determined by GC; S (cm^2) is the effective membrane surface area.

$$J_{O_2} = \frac{F_{air,inlet}(C_{O_2} - 20)}{S(100 - C_{O_2})} \tag{1}$$

The oxygen permeation flux F_{O_2} during the production of pure oxygen was directly determined by using a bubble flow meters. The O_2 permeation rates J_{O_2} (cm^3 min^{-1} cm^{-2}) in the production of pure oxygen were calculated by eq 2.

$$J_{O_2} = \frac{F_{O_2}}{S} \tag{2}$$

The oxygen recovery has been calculated by

$$O_{2,recovery} = \frac{F_{O_2}}{F_{air,inlet} \cdot C_{O_2}} \tag{3}$$

with F_{O_2} as oxygen permeation flux, C_{O_2} as the oxygen concentration in vol %, and $F_{air,inlet}$ as air flow rate at the inlet of the feed.

3. Results and Discussion

3.1. Production of Oxygen-Enriched Air Applying Reduced Pressure on the Permeate Side. In a previous paper, we reported the production of O_2-enriched air by raising the air pressure on the shell side while having air at atmospheric pressure on the core side.[24] Here, we propose to produce O_2-enriched air in a flow-through permeator by using a vacuum pump to achieve a reduced pressure of 0.12 bar on the permeate/core side. Air was fed to the feed/shell side at 1.0 bar. Figure 4 shows the influence of the extraction rate of the O_2-enriched air by the vacuum pump on its oxygen content. By tuning the air supply to the core side and the extraction rate of the O_2-enriched air, different oxygen concentrations can be obtained in the O_2-enriched air. O_2 concentrations between 30 and 50 vol % with O_2-enriched air fluxes of 40−90 cm^3 (STP) min^{-1} were obtained. Although the oxygen concentration decreases from 50% to 30% with raising the air flow rate on the permeate side from 25 to 75 cm^3 (STP) min^{-1}, there is only a slight change of the oxygen partial pressure gradient across the membrane, and the oxygen permeation flux was found to be almost constant, as shown in Figure 4. As compared to the pressure-driven process for the production of O_2-enriched air (pressurized air on the feed side, O_2-enriched air at 1 bar on the permeate side),[24] the reduced-pressure process gives an about 4 times higher production rate of O_2-enriched air of a certain oxygen concentration. This O_2-enriched air produced in the flow-through permeator can be used as feed in the dead-end permeator for the production of pure oxygen.

3.2. Production of Pure Oxygen from 1 bar of O_2-Enriched Air Applying Reduced Pressure on the Permeate Side. Figure 5 shows the influence of the temperature on the production of pure oxygen from O_2-enriched air with different oxygen content in a dead-end permeator. The pressure of the feed/shell side was 1 bar, and the oxygen pressure on the permeate/core side was kept at 0.05 bar by using a vacuum pump. The oxygen
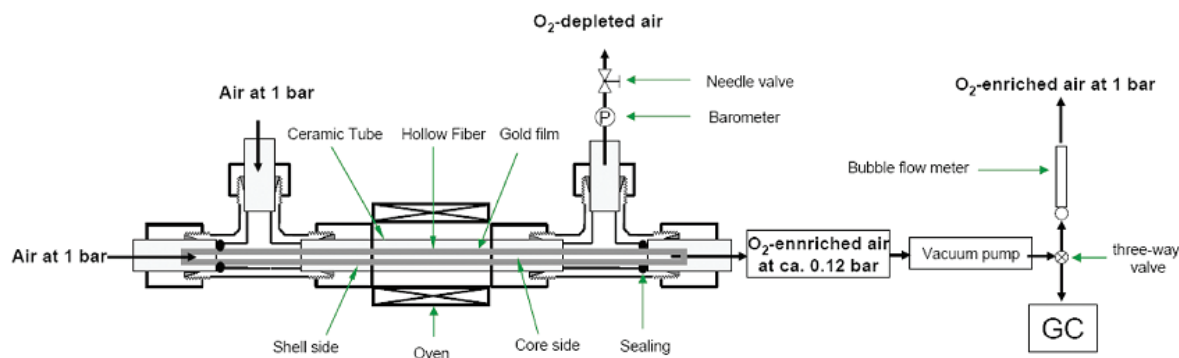
Figure 2. Permeator 1 in flow-through geometry for the production of O_2-enriched air.
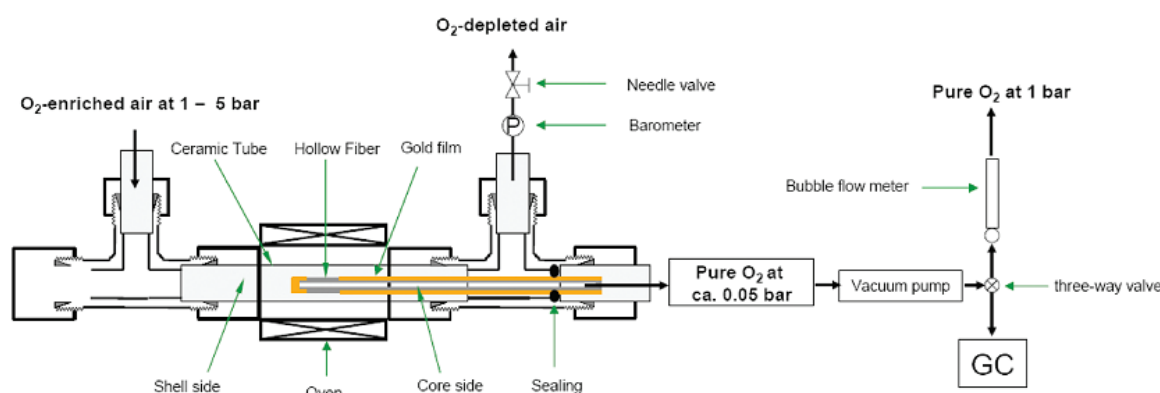

Figure 3. Permeator 2 in dead-end geometry for the production of pure O_2.
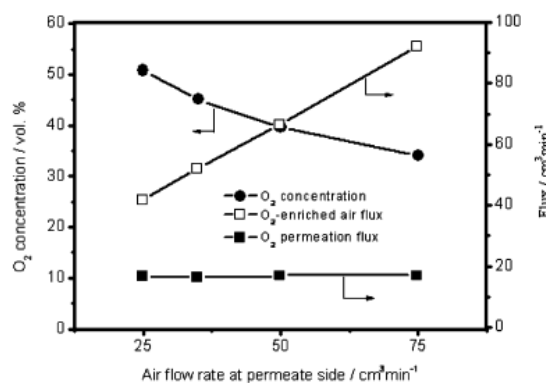

Figure 4. Influence of the air flow rate on the permeate side on the production of O_2-enriched air in permeator 1 (cf., Figure 2). Note that the amount of oxygen separated from air is constant. Feed/shell side: air flow = 300 cm^3 min^{-1} at 1 bar. Permeate/core side: O_2-enriched air flow = 25−75 cm^3 (STP) min^{-1} at 0.12 bar. T = 950 °C.

Figure 5. Influence of the temperature on the production of pure oxygen from O_2-enriched air with different oxygen concentration in permeator 2 (cf., Figure 3). Feed/shell side: air flow rate = 150 cm^3 min^{-1} at 1 bar. Permeate/core side: pure O_2 at about 0.05 bar.

production rate increases with increasing temperature and with increasing oxygen content of the O_2-enriched air. For example, the oxygen permeation rate increases from 3.7 to 6.8 cm^3 (STP) cm^{-2} min^{-1} with increasing oxygen concentration in the fed air from 20 to 50 vol %. In a former study,[20] we reported an oxygen permeation rate of 7.6 cm^3 cm^{-2} min^{-1} using He as sweep gas at 900 °C. Obviously, the use of a sweep gas to reduce the oxygen partial pressure as driving force is more effective than removing the permeated oxygen at an oxygen pressure of 0.05 bar by a vacuum pump. However, the

application of sweep gases, except steam, needs a subsequent separation step.

Figure 6 presents the influence of the O_2-enriched air flow rate at 1 bar on the core side of the BCFZ hollow fiber membrane on the oxygen permeation rate at 900 °C. The oxygen permeation flux decreases slowly with decreasing flow rate of the fed air from 200 to 50 cm^3 min^{-1} and quickly with decreasing the air flow rate from 50 to 10 cm^3 min^{-1}. For example, the oxygen permeation rate decreased to 5% and 21% with decreasing the flow rate of air with oxygen concentration of 50 vol % from 200 to 50 cm^3 min^{-1} and 50 to 10 cm^3 min^{-1}, respectively.
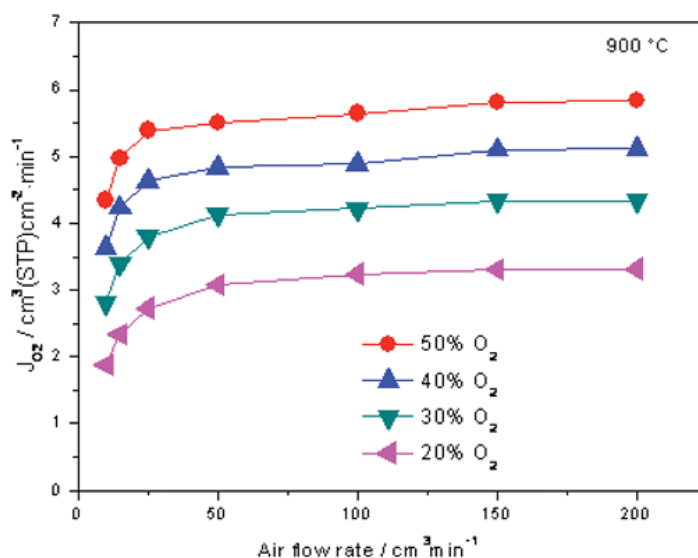
Figure 6. Influence of the flow rate of the fed O_2-enriched air on the production of pure oxygen for different oxygen concentration at 900 °C in permeator 2 (cf., Figure 3). Feed/shell side: O_2-enriched air flow rate = 10−200 cm^3 min^{-1} at 1 bar. Permeate/core side: pure O_2 at about 0.05 bar.
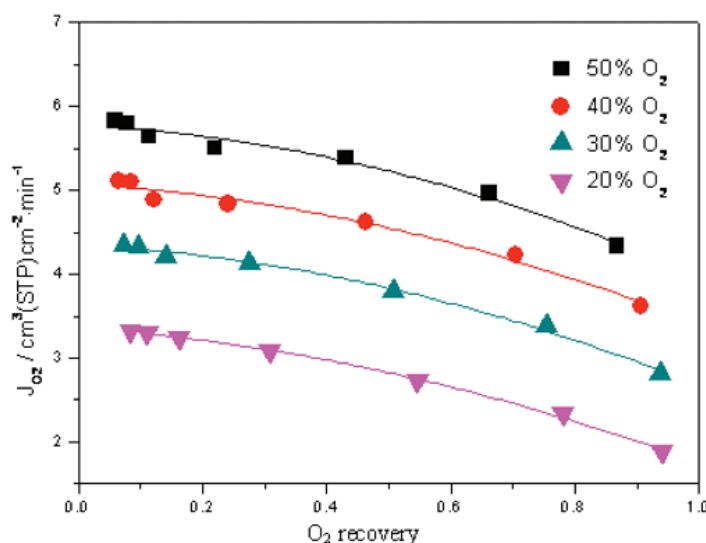

Figure 7. Interplay of oxygen permeation flux and oxygen recovery for fed O_2-enriched air at 900 °C in permeator 2 (cf., Figure 3). Feed/shell side: O_2-enriched air flow rate = 10−200 cm^3 min^{-1} at 1 bar. Permeate/core side: pure O_2 at about 0.05 bar.

Figure 7 shows the influence of the oxygen permeation rate on oxygen recovery (at 1.0 bar and at 900 °C) for different O_2 concentration in the feed. The relation between the oxygen permeation rate and the oxygen recovery was reached by variation of the flow rate of air on the feed side. The oxygen permeation rates increase with increasing the oxygen concentration of air. Under the same oxygen concentration, the oxygen recovery decreases with increasing the oxygen permeation rate. It also means that the improvement in oxygen recovery comes at the cost of a decreased permeation rate. Accordingly, an optimal compromise between the oxygen permeation rate and the oxygen recovery can be realistic. For example, at an oxygen recovery of 50%, an oxygen permeation rate is around 2.8 and 5.2 cm^3 cm^{-2} min^{-1} under the oxygen concentration 20 and 50 vol % in air, respectively.

3.3. Production of Pure Oxygen from O_2-Enriched Air at Elevated Pressure on the Feed Side. The oxygen permeation rate J_{O_2} can be expressed by the Wagner equation:[4,26]

$$J_{O_2} = -\frac{RT}{4^2F^2L}\int_{\ln P_2}^{\ln P_1}\frac{\sigma_i \cdot \sigma_e}{\sigma_i + \sigma_e}d\ln P_{O_2} \tag{4}$$

Integration of eq 4 for assuming $\sigma_e \gg \sigma_i$ and assuming constant σ_i gives

$$J_{O_2} = -\frac{RT\sigma_e\sigma_i}{4^2F^2(\sigma_e + \sigma_i)L}\ln\frac{P_1}{P_2} \tag{5}$$

where σ_e and σ_i are the electronic and ionic conductivities, respectively. R, F, T, and L denote the gas constant, Faraday
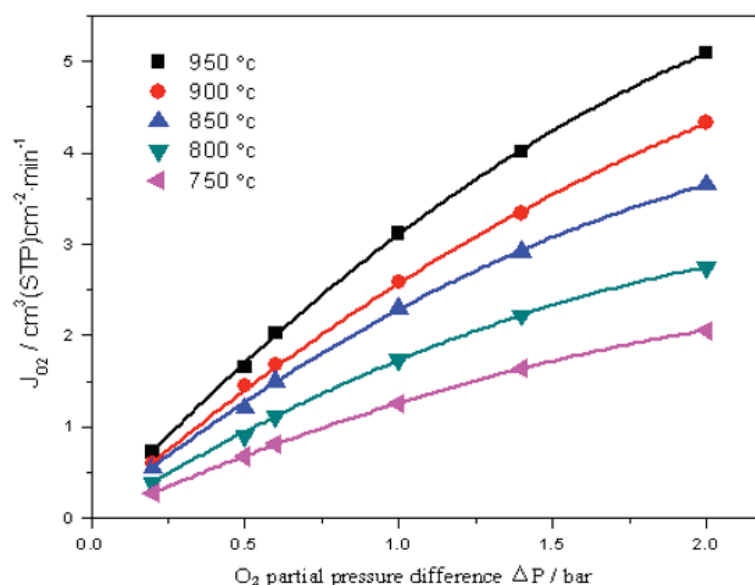
56

Figure 8. Influence of the oxygen partial pressure difference on the production of pure oxygen in permeator 2 (cf., Figure 3) at different temperatures. Feed/shell side: O_2-enriched air flow = 150 cm³ min⁻¹ at different pressure. Permeate/core side: pure O_2 at 1 bar.

constant, temperature, and thickness of the membrane, respectively. P_1 and P_2 are the oxygen partial pressures on the feed and permeate sides, respectively. Therefore, the oxygen permeation flux J_{O_2} is proportional to the logarithmic ratio of the oxygen partial pressures P_1 and P_2 if all other conditions are fixed. When increasing the oxygen partial pressure gradient across the membrane, according to the Wagner theory a higher oxygen permeation flux can be obtained.

However, for mixed oxygen ion−electron conducting materials, the surface processes can become rate limiting for oxygen transport through the membrane rather than bulk diffusion. Under surface reaction, we understand the incorporation of oxygen into the lattice (adsorption, dissociation, ionization, incorporation on a lattice vacancy) and vice versa on the permeate side. For our perovskite hollow fiber membrane with 170 μm wall thickness, we found that the main transport mechanism is bulk diffusion with a contribution of the surface reaction.[27] This conclusion was drawn as follows. Assuming that $\sigma_e \gg \sigma_i$ and further assuming that the oxygen partial pressure dependence of the ionic conductivity σ_i follows a power law of the form $\sigma_i = \sigma_i^0 \cdot P_{O_2}{}^n$,[28] integration of eq 4 yields

$$J_{O_2} = -\frac{\sigma_i^0 RT}{4^2 F^2 nL}(P_1^n - P_2^n) \qquad (6)$$

with σ_i^0 as the oxygen ionic conductivity at $P_{O_2} = 10^5$ Pa, and L as membrane thickness. n is the fit parameter, which is derived from the steady-state oxygen permeation. From the value of n, the rate-limiting step of the oxygen permeation can be identified.[29,30] For negative values of n, the oxygen permeation is dominated by the bulk diffusion, while for $n \geq 0.5$ the exchange processes at the membrane surfaces can be assumed as rate-limiting. In the case of the surface exchange as rate-limiting step, a catalytic coating of the membrane can accelerate the oxygen flux. In the surface exchange current model,[31] J_{O_2} gives a linear relationship with $(P_1/P_{O_2})^{0.5} - (P_2/P_{O_2})^{0.5}$ if oxygen transport is controlled by the surface exchange reaction. In the case of bulk diffusion control, J_{O_2} is a linear function of $\ln(P_1/$

P_2). The detailed analysis of oxygen transport through our BCFZ hollow fiber membrane with 170 μm wall thickness gave that bulk diffusion dominates oxygen transport with a remarkable influence of the surface reaction.

When the pressure on the permeate side is fixed at 1 bar, the oxygen partial pressure gradient can be established by elevating the pressure of O_2-enriched air with different oxygen content. For example, an oxygen pressure gradient of 1.5 bar across the membrane can be established by compressing oxygen-enriched air with 50 vol % oxygen at 5 bar. Figure 8 indicates the influence of the oxygen partial pressure difference on the production of pure O_2 at different temperatures. The oxygen permeation rates increase with increasing oxygen partial pressure difference and with increasing temperature. At an oxygen partial pressure difference of 1 bar, an oxygen flux of 3.0 cm³ (STP) cm⁻² min⁻¹ is obtained at 950 °C.

3.4. Production of Pure Oxygen Combining Reduced Pressure on the Permeate Side and Elevated Feed Pressure. As discussed above, according to the Wagner theory,[4,26] the oxygen permeation flux can be enhanced by increasing the oxygen partial pressure gradient across membrane. To obtain a higher oxygen permeation flux, the pressure on the permeate side was reduced to 0.05 bar by using a vacuum pump, and the pressure on the feed side was simultaneously elevated. Figure 9 shows the influence of the air pressure on the feed side on the production of pure oxygen at different temperatures. It can be seen that the oxygen permeation flux increased with raising the pressure on the feed side while keeping the pressure at 0.05 bar on the permeate side. For the same pressure difference, the oxygen permeation flux increases with rising temperature. At 950 °C and 5 bar of total pressure difference, the oxygen permeation rate reaches 8.5 cm³ (STP) cm⁻² min⁻¹. It can be predicted that the oxygen permeation rate can be further enhanced by compressing O_2-enriched air as feed.

The oxygen-enriched air produced in permeator 1 (Figure 2) with different oxygen concentration was used as feed in permeator 2 (Figure 3) for the production of pure oxygen. Figure 10 shows the dependence of the oxygen permeation flux on the
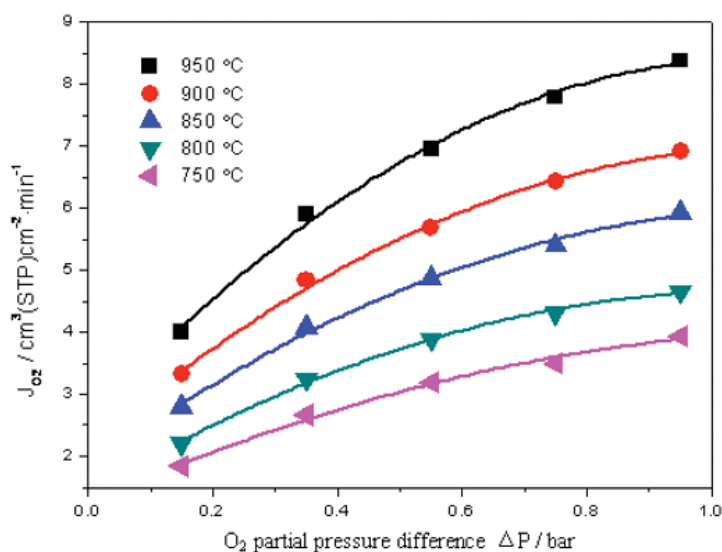
Figure 9. Influence of the oxygen partial pressure difference on the production of pure oxygen in permeator 2 (cf., Figure 3) at different temperatures. Feed/shell side: air flow = 150 cm³ min⁻¹ with 20 vol % O_2 at different pressure. Permeate/core side: pure O_2 at about 0.05 bar.
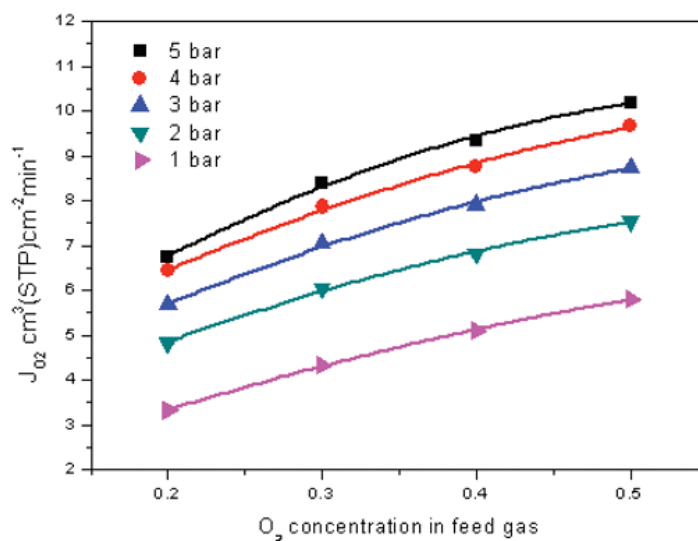

Figure 10. Influence of oxygen concentration in the fed air at different feed pressure on the production of pure oxygen for different feed pressures at 900 °C in permeator 2 (cf., Figure 3). Feed/shell side: O_2-enriched air flow rate = 150 cm³ min⁻¹. Permeate/core side: pure O_2 at about 0.05 bar.

oxygen concentration in the O_2-enriched air at different pressure on the feed side at 900 °C. For different feed pressures, the oxygen permeation rates increase with increasing the oxygen concentration. Raising the oxygen concentration in the fed oxygen-enriched air has the same effect as raising the pressure of the O_2-enriched air on the feed side. The oxygen permeation flux increases from 5.8 to 10.2 cm³ (STP) cm⁻² min⁻¹ when increasing the oxygen concentration in the fed O_2-enriched air from 20 to 50 vol % at 5 bar and at 900 °C. Zhu et al.[17] reported an oxygen flux of 9.5 cm³ (STP) cm⁻² min⁻¹ in a dead-end tube perovskite membrane permeator at 925 °C and vacuum of ~100 Pa on the permeate side and 7 bar air on the feed side. Ito et al.[16] reported an oxygen flux of 9 cm³ (STP) cm⁻² min⁻¹ of an asymmetrical tubular perovskite membrane with a ~50 μm dense layer at 900 °C and 10 bar air pressure. Here, by using the oxygen-enriched air as feed, an almost equivalent

oxygen permeation rate was obtained at relatively low pressure on the feed side.

Figure 11 presents the temperature dependence of oxygen permeation rate when using air or O_2-enriched air as feed. For all of the investigated temperatures and in the case of air as feed, the oxygen permeation fluxes have been significantly enhanced when raising the air pressure from 1 to 5 bar. In addition, by holding the pressure at 5 bar and replacing air by O_2-enriched air as the feed, the oxygen permeation fluxes were further enhanced. It can be seen from Figure 11 that the oxygen permeation rate reached 13 cm³ (STP) cm⁻² min⁻¹ at 950 °C.

3.5. Long-Term Operation of Production of Pure Oxygen. In our previous study, the perovskite BCFZ hollow fiber membrane permeator showed excellent stability and was operated steadily over more than 800 h in the production of O_2-
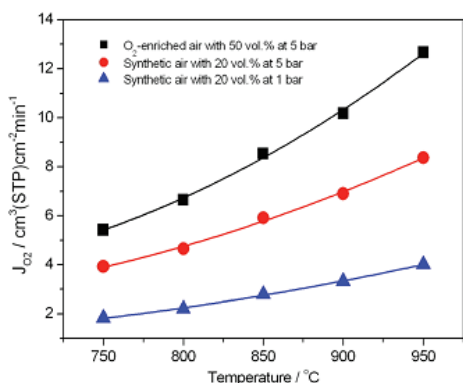
the conditions of 0.05 bar on permeate side and an elevated pressure on the feed side at 900 °C. A high oxygen purity up to 99.9 vol % and an oxygen permeation flux of 9.7 cm^3 (STP) cm^{-2} min^{-1} were obtained during 150 h of operation.

Literature Cited

(1) Jasra, R. V.; Choudary, N. V.; Baht, S. G. T. Separation of gases by pressure swing adsorption. *Sep. Sci. Technol.* **1991**, *16*, 885.

(2) Matson, S. L.; Ward, W. J.; Kimure, S. G.; Browall, W. R. Membrane oxygen enrichment. 2. Economic-assessment. *J. Membr. Sci.* **1986**, *29*, 79.

(3) Caro, J.; Caspary, K. J.; Hamel, C.; Hoting, B.; Kölsch, P.; Langanke, B.; Nassauer, K.; Schiestel, T.; Schmidt, A.; Schomäcker, R.; Seidel-Morgenstern, A.; Tsotsas, E.; Voigt, I.; Wang, H. H.; Warsitz, R.; Werth, S.; Wolf, A. Catalytic membrane reactors for partial oxidation using perovskite hollow fiber membranes and for partial hydrogenation using a catalytic membrane contactor. *Ind. Eng. Chem. Res.* **2007**, *46*, 2286.

(4) Liu, Y. T.; Tan, X. Y.; Li, K. Mixed conducting ceramics for catalytic membrane processing. *Catal. Rev.-Sci. Eng.* **2006**, *48*, 145.

(5) Chen, C. S.; Feng, S. J.; Ran, S.; Zhu, D. C.; Liu, W.; Bouwmeester, H. J. M. Conversion of methane to syngas by a membrane-based oxidation-reforming process. *Angew. Chem., Int. Ed.* **2003**, *42*, 5196.

(6) Martynczuk, J.; Liang, F. Y.; Arnold, M.; Sepelak, V.; Feldhoff, A. Aluminum-doped perovskites as high-performance oxygen permeation materials. *Chem. Mater.* **2009**, *21*, 1586.

(7) Kharton, V. V.; Yaremchenko, A. A.; Kovalevsky, A. V.; Viskup, A. P.; Naumovich, E. N.; Kerko, P. F. Perovskite-type oxides for high-temperature oxygen separation membranes. *J. Membr. Sci.* **1999**, *163*, 307.

(8) Bouwmeester, H. J. M. Dense ceramic membranes for methane conversion. *Catal. Today* **2003**, *82*, 141.

(9) Wang, H. H.; Cong, Y.; Yang, W. S. Continuous oxygen ion transfer medium as a catalyst for high selective oxidative dehydrogenation of ethane. *Catal. Lett.* **2002**, *84*, 101.

(10) Jiang, H. Q.; Wang, H. H.; Werth, S.; Schiestel, T.; Caro, J. Simultaneous production of hydrogen and synthesis gas by combining water splitting with partial oxidation of methane in a hollow fiber membrane reactor. *Angew. Chem., Int. Ed.* **2008**, *47*, 9341.

(11) Jiang, H. Q.; Cao, Z. W.; Schirrmeister, S.; Schiestel, T.; Caro, J. A coupling strategy to produce hydrogen and ethylene in a membrane reactor. *Angew. Chem., Int. Ed.* **2010**, *49*, 5656.

(12) Jiang, H. Q.; Liang, F. Y.; Czuprat, O.; Efimov, K.; Feldhoff, A.; Schirrmeister, S.; Schiestel, T.; Wang, H. H.; Caro, J. Hydrogen production by water dissociation in surface-modified BaCo$_x$Fe$_y$Zr$_{1-x-y}$O$_{3-\delta}$ hollow fiber membrane reactor with improved oxygen permeation. *Chem.-Eur. J.* **2010**, *16*, 7898.

(13) Tong, J. H.; Yang, W. S.; Zhu, B. C.; Cai, R. Investigation of ideal zirconium-doped perovskite-type ceramic membrane materials for oxygen separation. *J. Membr. Sci.* **2002**, *203*, 175.

(14) Luo, H. X.; Wei, Y. Y.; Jiang, H. Q.; Yuan, W. H.; Lv, Y. X.; Caro, J.; Wang, H. H. Performance of a ceramic membrane reactor with high oxygen flux Ta-containing perovskite for the partial oxidation of methane to syngas. *J. Membr. Sci.* **2010**, *350*, 154.

(15) Liu, S. M.; Gavalas, G. R. Oxygen selective ceramic hollow fiber membranes. *J. Membr. Sci.* **2005**, *246*, 103.

(16) Ito, W.; Nagai, T.; Sakon, T. Oxygen separation from compressed air using a mixed conducting perovskite-type oxide membrane. *Solid State Ionics* **2007**, *178*, 809.

(17) Zhu, X. F.; Sun, S. M.; Cong, Y.; Yang, W. S. Operation of perovskite membrane under vacuum and elevated pressures for high-purity oxygen production. *J. Membr. Sci.* **2009**, *345*, 47.

(18) Wang, H. H.; Kölsch, P.; Schiestel, T.; Tablet, C.; Werth, S.; Caro, J. Production of high-purity oxygen by perovskite hollow fiber membranes swept with steam. *J. Membr. Sci.* **2006**, *284*, 5.

(19) Tong, J. H.; Yang, W. S.; Zhu, B. C.; Cai, R. Investigation of ideal zirconium-doped perovskite-type ceramic membrane materials for oxygen separation. *J. Membr. Sci.* **2002**, *203*, 175.

Figure 11. Temperature dependence of oxygen permeation rate when using air or O$_2$-enriched air as feed. The pressure on the permeate/core side was kept at about 0.05 bar by using a vacuum pump. Feed/shell side: feed gas flow rate = 150 cm^3 (STP) min^{-1}.
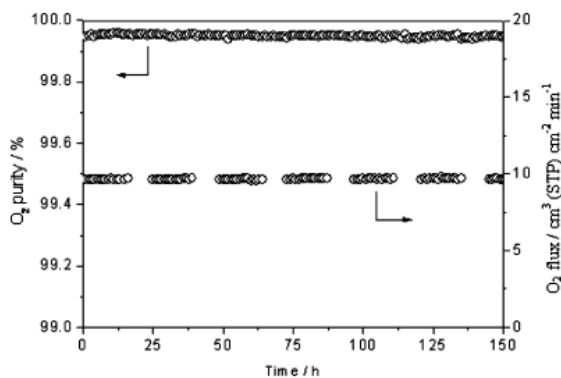

Figure 12. Long-term operation of the production of pure oxygen in permeator 2 (cf., Figure 3): O$_2$ purity and oxygen permeation flux of the BCFZ hollow fiber membrane at 900 °C. Feed/shell side: air flow rate = 150 cm^3 min^{-1} at 4 bar. Permeate/core side: pure O$_2$ at about 0.05 bar.

enriched air.[24] The reliability of the perovskite BCFZ hollow fiber membrane for the production of pure oxygen in the dead-end permeator was evaluated for a 150 h oxygen permeation with a feed of 50 vol % O$_2$-enriched air at 4 bar and reduced pressure of 0.05 bar on the permeate side. The BCFZ hollow-fiber membrane was still gastight after 150 h, at which time we stopped the test. Figure 12 shows the oxygen permeation rate and the oxygen purity during the 150 h operation. A high oxygen purity of 99.9 vol % and a stable oxygen permeation rate of 9.7 cm^3 cm^{-2} min^{-1} were found. This experimental finding indicates that the BCFZ hollow fiber itself was stable.

4. Conclusions

The production of pure oxygen and O$_2$-enriched air using BCFZ hollow fiber membranes was studied in this work. In a flow-through type permeator, O$_2$-enriched air with an oxygen concentration of 30−50 vol % was produced from air on the feed/shell side of the hollow fiber when applying a reduced pressure of 0.12 bar on the permeate side. This O$_2$-enriched air was used as pressurized feed in a dead-end type permeator for the production of pure oxygen at 0.05 bar. An oxygen permeation flux of 10.2 cm^3 (STP) cm^{-2} min^{-1} was reached in the production of pure oxygen at 900 °C when using pressurized O$_2$-enriched air with 50 vol % O$_2$ at 5 bar. The reliability of the perovskite hollow fiber membrane was tested for 150 h under

(20) Schiestel, T.; Kilgus, M.; Peter, S.; Caspary, K. J.; Wang, H. H.; Caro, J. Hollow fibre perovskite membranes for oxygen separation. *J. Membr. Sci.* **2005**, *258*, 1.

(21) Wang, H. H.; Tablet, C.; Schiestel, T.; Werth, S.; Caro, J. Partial oxidation of methane to syngas in a perovskite hollow fiber membrane reactor. *Catal. Commun.* **2006**, *7*, 907.

(22) Jiang, H. Q.; Wang, H. H.; Liang, F. Y.; Werth, S.; Schiestel, T.; Caro, J. Direct decomposition of nitrous oxide to nitrogen by in situ oxygen removal with a perovskite membrane. *Angew. Chem., Int. Ed.* **2009**, *48*, 2983.

(23) Jiang, H. Q.; Xing, L.; Czuprat, O.; Wang, H. H.; Schirrmeister, S.; Schiestel, T.; Caro, J. Highly effective NO decomposition by in situ removal of inhibitor oxygen using an oxygen transporting membrane. *Chem. Commun.* **2009**, 6738.

(24) Wang, H. H.; Werth, S.; Schiestel, T.; Caro, J. Perovskite hollow-fiber membranes for the production of oxygen-enriched air. *Angew. Chem., Int. Ed.* **2005**, *44*, 6906.

(25) Baker, R. In *Membrane Technology in the Chemical Industry: Further Directions": Membrane Technology in the Chemical Industry, Part II*; Nunes, S. P., Peinemann, K. V., Eds.; Wiley−VCH: Weinheim, 2001; p. 280.

(26) Sunarso, J.; Baumann, S.; Serra, J. M.; Meulenberg, W. A.; Liu, S.; Lin, Y. S.; Da Costa, J. C. D. Mixed ionic-electronic conducting (MIEC) ceramic-based membranes for oxygen separation. *J. Membr. Sci.* **2008**, *320*, 13.

(27) Tablet, C.; Grubert, G.; Wang, H. H.; Schiestel, T.; Schroeder, M.; Langanke, B.; Caro, J. Oxygen permeation study of perovskite hollow fiber membranes. *Catal. Today* **2005**, *104*, 126.

(28) Schroeder, M. On the behaviour of mixed-conducting complex metal oxides in oxygen potential gradients. Habilitation Thesis, RWTH Aachen, 2005.

(29) Wang, H. H.; Schiestel, T.; Tablet, C.; Schroeder, M.; Caro, J. Mixed oxygen ion and electron conducting hollow fiber membranes for oxygen separation. *Solid State Ionics* **2006**, *177*, 2255.

(30) Huang, K. Q.; Schroeder, M.; Goodenough, J. B. Oxygen permeation in Co-containing perovskites: Surface exchange vs. bulk diffusion. Proc. of the Intern. Symp. "Solid State Ionic Devices". *Electrochem. Soc. Proc. Ser.* **1999**, *99-13*, 95.

(31) Kim, S.; Yang, Y. L.; Jacobson, A. J.; Abeles, B. Diffusion and surface exchange coefficients in mixed ionic electronic conducting oxides from the pressure dependence of oxygen permeation. *Solid State Ionics* **1999**, *121*, 31.

4 Novel cobalt-free membranes $BaFe_{0.95-x}La_xZr_{0.05}O_{3-\delta}$ (BFLZ) for oxygen separation

4.1 Summary

In practice, the oxygen permeability and stability of OTM under harsh operating conditions such as intermediate temperatures, large oxygen partial pressure gradients, or reducing atmospheres, are crucial for their industrial applications. In the past few decades, a large number of cobalt-based perovskite-type membranes with high oxygen permeability such as $Ba_{1-x}Sr_xCo_{1-y}Fe_yO_{3-\delta}$, and $La_{1-x}Sr_xCo_{1-y}Fe_yO_{3-\delta}$ have been developed. However, due to the toxic and expensive Co, and the structural instability of the cobalt-based perovskite-type membranes, which were studied in detail in the chapter 2, the cobalt-based perovskite-type membranes is very challenging in the industrial application. Therefore, the development of cobalt-free perovskite-type oxides is of great interest.

In this capital, we selected La to partially substitute for Fe on the B-site of $BaFe_{0.95}Zr_{0.5}O_{3-\delta}$ owing to its large ionic radius ($La^{3+}(VI) = 1.03$ Å) and its common trivalent oxidation state. The BFLZ materials were characterized by X-ray diffraction (XRD), scanning electron microscopy (SEM), and after pressing and sintering as membranes which were used for oxygen separation from air. The influence of the partial substitution of La for Fe on the B-site of $BaFe_{0.95}Zr_{0.5}O_{3-\delta}$ on crystal structure and oxygen permeability was investigated. It was found that the highest La content in BFLZ for the formation of a pure cubic perovskite structure without any detectable impurities is about x = 0.04. For the La content of x = 0.04 with the largest volume of the cubic unit cell, the highest oxygen permeation flux with 6.3 and 1.24 $cm^3(STP) \cdot min^{-1}cm^{-2}$ was found at 750 and 950 °C, respectively. It follows from XRD that for La contents x > 0.04 the secondary phase $Ba_6La_2Fe_4O_{15}$ has been formed in high-La BFLZ (x = 0.05 and 0.075) materials. Furthermore, the influence of oxygen partial pressures on the oxygen permeation flux and the oxygen ionic conductivity can be described with the Wagner theory for bulk diffusion of oxygen ions as rate-limiting step for oxygen permeation. The result of the long-term oxygen permeability suggests that the BFLZ (x = 0.04) membrane exhibits good oxygen permeability and stability, which make this material a promising candidate for industrial applications like oxygen separation from air and catalytic hydrocarbon partial oxidation.

4.2 B-site La-doped BaFe$_{0.95-x}$La$_x$Zr$_{0.05}$O$_{3-\delta}$ perovskite-type membranes for oxygen separation

Fangyi Liang, Kaveh Partovi, Heqing Jiang, Huixia Luo, and Jürgen Caro

Journal of Materials Chemistry A

RSC Publishing

B-site La-doped BaFe$_{0.95-x}$La$_x$Zr$_{0.05}$O$_{3-\delta}$ perovskite-type membranes for oxygen separation

Fangyi Liang,[a] Kaveh Partovi,[a] Heqing Jiang,[b] Huixia Luo[a] and Jürgen Caro*[a]

Partial La-substitution for Fe on the B-site of the perovskite BaFe$_{0.95-x}$La$_x$Zr$_{0.05}$O$_{3-\delta}$ (BFLZ) was achieved by applying a sol–gel synthesis method. The highest La content in BFLZ for the formation of a pure cubic perovskite structure without any detectable impurities is about $x = 0.04$. It is found for the first time that the introduction of La on the B-site of a mixed oxide stabilizes the cubic structure. Furthermore, the formation of the cubic structure of BFLZ increases significantly the oxygen permeability. The maximum oxygen permeation flux is found for a La-content of $x = 0.04$ with the largest volume of the cubic unit cell, reaching 0.63 and 1.24 cm^3 (STP) min^{-1} cm^{-2} for a 1.1 mm thick membrane at 750 and 950 °C, respectively. This finding is in complete agreement with the XRD structure analysis, showing that the highest B-site La-substitution of BFLZ under conservation of the pure cubic perovskite phase without forming any foreign phase was about $x = 0.04$. For BFLZ with $x > 0.04$, the secondary phase Ba$_6$La$_2$Fe$_4$O$_{15}$ forms increasingly and the oxygen permeation flux decreases. The influence of the sweep gas flow rates on the oxygen permeation flux and the oxygen ionic conductivity were found to be in good agreement with the Wagner theory, indicating the oxygen ion bulk diffusion as a rate-limiting step of oxygen transport. Stable oxygen permeation fluxes were obtained during the long-term oxygen permeation operation of the BFLZ ($x = 0.04$) membrane over 170 h at 750 and 950 °C, respectively.

Introduction

Oxygen transporting membranes (OTMs),[1,2] based on mixed electronic and ionic conductors of perovskite-type oxides, attract much attention due to their promising potential applications for high purity oxygen production,[3–5] in catalytic membrane reactors,[6–8] and as cathodes in solid oxide fuel cells (SOFCs).[9] In practice, the oxygen permeability and stability of OTMs under harsh operating conditions such as intermediate temperatures, large oxygen partial pressure gradients, or reducing atmospheres are crucial for their industrial applications.

In the past few decades, a large number of cobalt-based perovskite-type membranes with high oxygen permeability such as Ba$_{1-x}$Sr$_x$Co$_{1-y}$Fe$_y$O$_{3-\delta}$,[10,11] and La$_{1-x}$Sr$_x$Co$_{1-y}$Fe$_y$O$_{3-\delta}$[12–14] have been developed. However, the stability of cobalt-based perovskite-type membranes at intermediate temperatures or under reducing conditions is poor, because of the easy reduction of cobalt ions and the resulting big changes in the unit cell dimension.[15–17] Therefore, the development of cobalt-free perovskite-type oxides is of great interest. Recently, a number of cobalt-free membranes have been developed,

such as Ba$_{0.5}$Sr$_{0.5}$Fe$_{0.8}$Zn$_{0.2}$O$_{3-\delta}$,[18] Ba$_{0.5}$Sr$_{0.5}$Fe$_{1-x}$Al$_x$O$_{3-\delta}$,[19] Ba$_{0.5}$Sr$_{0.5}$Fe$_{0.8}$Cu$_{0.2}$O$_{3-\delta}$,[20] BaFe$_{1-x}$Y$_x$O$_{3-\delta}$,[21] BaFe$_{1-x}$Ce$_x$O$_{3-\delta}$,[22] BaFe$_{1-y}$Zr$_y$O$_{3-\delta}$,[23] and La$_x$Ba$_{1-x}$FeO$_{3-\delta}$.[24]

The cobalt-free membranes are mostly based on BaFeO$_{3-\delta}$ oxides. However, BaFeO$_{3-\delta}$ shows a low oxygen permeability and crystallizes in a hexagonal structure because of the ionic radius of Ba^{2+} which is too large to stabilize a cubic perovskite structure. A perovskite-type oxide with cubic structure usually exhibits a higher oxygen permeability than those with other structures such as hexagonal, rhombohedral, or fluorite structures. The cubic perovskite structure of BaFeO$_{3-\delta}$ can be stabilized by (i) the partial substitution of the A-site with smaller cations, such as Sr, Ca, La, and Y,[24,25] (ii) the partial substitution of the B-site with larger cations, such as Y, Cu, Ni, and Zr,[21,23,26] (iii) the partial substitution of both A- and B-sites by *e.g.* Y.[27] The partial substitution of the A-site with smaller cations can lead to a stabilization of the cubic perovskite structure. However, the volume of the cubic unit cell will be reduced which – in turn – reduces the oxygen flux. On the other hand, the partial substitution of the B-site with larger low-valency cations can result not only in the stabilization of the cubic perovskite structure, but can also increase the volume of the cubic unit cell and the oxygen vacancy concentration which are beneficial to the oxygen permeation. The improvement of the stability of the perovskite structure by introducing Zr on the B-site was reported by several authors.[28–30]

[a]*Institute of Physical Chemistry and Electrochemistry, Leibniz University Hannover, Callinstr. 3A, D-30167 Hannover, Germany. E-mail: juergen.caro@pci.uni-hannover.de; Fax: +49-511-762-19121; Tel: +49-511-762-3175*

[b]*Max-Planck-Institut für Kohlenforschung, Kaiser-Wilhelm-Platz 1, D-45470 Mülheim an der Ruhr, Germany*

63

In this work, we selected La to partially substitute for Fe on the B-site of $BaFe_{0.95}Zr_{0.05}O_{3-\delta}$ owing to its large ionic radius $(La^{3+}(vi,\dagger) = 1.03$ Å$)$[31] and its common trivalent oxidation state. To the best of our knowledge, the only La-doping on the B-site of a perovskite to stabilize the cubic structure was reported for $SrCo_{0.95}La_{0.05}O_{3-\delta}$ with hexagonal structure by Zeng *et al.*[32] However, bringing La on the B-site of $SrCoO_{3-\delta}$ perovskite cannot stabilize the cubic structure since the electron configuration in the outer orbits of La^{3+} is 4d(10).[32] Here, we will study the influence of the partial substitution of La for Fe on the B-site of $BaFe_{0.95}Zr_{0.05}O_{3-\delta}$ (BFLZ) on crystal structure and oxygen permeability.

Experimental

$BaFe_{0.95-x}La_xZr_{0.05}O_{3-\delta}$ (BFLZ, $0 \le x \le 0.075$) powders were prepared by a combined citric acid and ethylene-diamine tetra-acetic acid (EDTA) complex method, as described in detail elsewhere.[33,34] The calculated amounts of $Ba(NO_3)_2$, $Fe(NO_3)_3$, $ZrO(NO_3)_2$ and $La(NO_3)_3$ in their appropriate stoichiometric ratios were dissolved in an aqueous solution, followed by the addition of EDTA and citric acid with the molar ratios of EDTA/citric acid/ metal cations $= 1 : 1.5 : 1$. The pH value of the solution was adjusted to around 9 by adding NH_4OH. The solution was then heated in the temperature range of 120–150 °C under constant stirring to obtain a dark gel. After the dark gel was burnt in a heating mantle, the obtained product was treated at 950 °C for 10 h to obtain BFLZ perovskite powder. The calcined powders were uniaxially pressed into pellets under 150 kN and sintered under ambient pressure at 1200 °C for 10 h in air to become gas-tight membrane discs with 14 mm in diameter and 1.1 mm in thickness.

X-Ray diffraction (XRD) was performed at room temperature using a Bruker-AXS D8 Advance diffractometer equipped with a Cu Kα radiation at 40 kV and 40 mA and a receiving slit of 0.05 mm using a step-scan mode in the 2θ range of 20–80° with intervals of 0.02.

Oxygen permeation was measured in a high-temperature permeation device, which is described in our previous papers.[35] The disc membranes were sealed onto an alumina tube with a gold paste (Heraeus, Germany) at 950 °C for 5 h. The feed side was fed with synthetic air (20 vol% O_2/80 vol% N_2), whereas Ne (99.995%) and He (99.995%) were fed to the sweep side. All gas flows were controlled by mass flow controllers (Bronkhorst, Germany) and all flow rates were regularly calibrated by using a bubble flow meter. The concentrations of the gases at the exit of the reactor were analyzed by an on-line gas chromatograph (Agilent 7890A) with a Molsieve 5A column. The total flow rate of the effluents on the permeate side was calculated by using Ne as an internal standard. The total O_2 leakage was calculated and subtracted from the total O_2 flux after the N_2 concentration was measured, as described in detail elsewhere.[36]

Results and discussions

Crystal structure

Perovskite-type oxides of the composition ABO_3 can host different cations on the A- and B-sites, which results in different

Table 1 Tolerance factors and crystal structures of $BaFeO_{3-\delta}$ and the compositions of $BaFe_{0.95-x}La_xZr_{0.05}O_{3-\delta}$ (BFLZ) with the assumption of sole Fe^{4+} and Fe^{3+}

Materials	Tolerance factor t		Crystal structure
	Fe^{4+}	Fe^{3+}	
$BaFeO_{3-\delta}$[38]	1.072	1.041	Hexagonal
$BaFe_{0.95}Zr_{0.05}O_{3-\delta}$	1.069	1.039	Rhombohedral
$BaFe_{0.95-x}La_xZr_{0.05}O_{3-\delta}$ ($x = 0.025$)	1.062	1.034	Cubic
$BaFe_{0.95-x}La_xZr_{0.05}O_{3-\delta}$ ($x = 0.04$)	1.059	1.031	Cubic
$BaFe_{0.95-x}La_xZr_{0.05}O_{3-\delta}$ ($x = 0.05$)	1.057	1.029	Cubic + $Ba_6La_2Fe_4O_{15}$
$BaFe_{0.95-x}La_xZr_{0.05}O_{3-\delta}$ ($x = 0.075$)	1.051	1.024	Cubic + $Ba_6La_2Fe_4O_{15}$

lattice structures. A good benchmark for the calculation of the lattice structure is the tolerance factor t described by Goldschmidt.[37]

$$t = \frac{r_A + r_O}{\sqrt{2}(r_B + r_O)} \qquad (1)$$

where r_A, r_B, and r_O are the ionic radii of the A-site metal ion (12-fold coordinated), the B-site cation (6-fold coordinated), and the oxygen ion (1.40 Å), respectively. The cubic perovskite structure can be maintained in the case of $0.75 \le t \le 1.0$ ($t = 1.0$ is the ideal cubic perovskite structure). When the tolerance factor is $t > 1.0$, a hexagonal structure tends to form. The values of the tolerance factor t for $BaFeO_{3-\delta}$[38] and the composition $BaFe_{0.95-x}La_xZr_{0.05}O_{3-\delta}$ (BFLZ) were estimated assuming Fe in the valency of $Fe^{3+}(vi, HS\ddagger)$ (0.645 Å) or $Fe^{4+}(vi, HS)$ (0.585 Å), as shown in Table 1. Introducing the large cation La^{3+} on the B-site of BFLZ leads to a slight decrease of the tolerance factor, which has a significant effect on the phase structure, as shown in Fig. 1. In praxis, iron on the B-site of BFLZ has a mixed oxidation state of Fe^{3+}–Fe^{4+}. Several authors reported that the fraction of Fe^{3+}/Fe in the perovskite oxides $BaSrFeO_{3-\delta}$ and $SrFeO_{3-\delta}$ increases with increasing content of the trivalent dopant on the B-site such as Ga,[39] Al,[19,40] or Sc.[41] An increasing trivalent Fe content results in a higher oxygen vacancy concentration and a larger unit cell, both of which are beneficial for oxygen permeation. It can be observed from Fig. 1a that the $BaFe_{0.95}Zr_{0.05}O_{3-\delta}$ samples without La^{3+} have a rhombohedral structure.[42] Surprisingly, we found that the phase transformation from a rhombohedral to a cubic perovskite structure takes place for La^{3+} doping for Fe on the B-site of BFLZ even for small La^{3+} contents ($x \le 0.025$). Therefore, our BFLZ samples with La contents of $x = 0.025$ and 0.04 consist of only a single cubic perovskite phase. However, for BFLZ with higher La contents ($x = 0.05$ and 0.075), beside the cubic perovskite as the major phase, weak reflexes of a secondary phase can be detected. The intensity of this secondary phase increases with increasing La content from $x = 0.05$ to $x = 0.075$. The relatively weak reflexes at Miller Index (110) of BFLZ (for $x = 0.05$ and 0.075) between
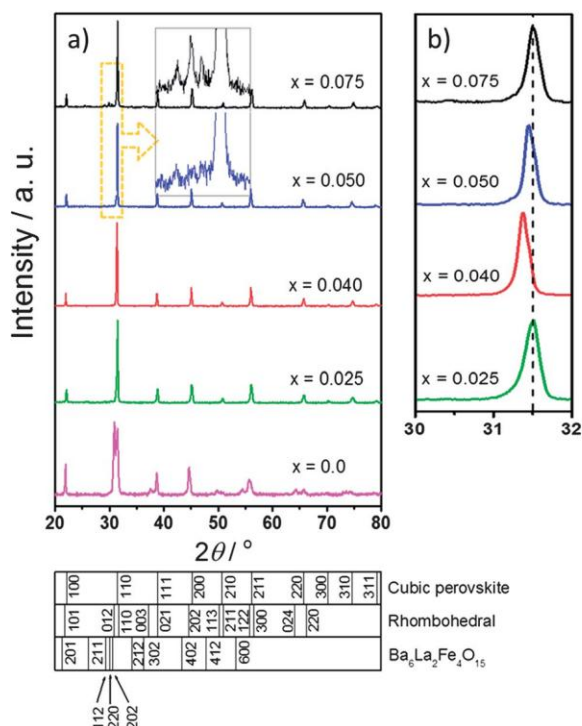

Fig. 1 XRD patterns of BaFe$_{0.95-x}$La$_x$Zr$_{0.05}$O$_{3-\delta}$ (BFLZ) (x = 0.025, 0.04, 0.05, and 0.075) samples after calcinations at 950 °C in air for 10 h. (a) 2θ from 20 to 80°. (b) 2θ from 30 to 32°.

Fig. 2 Oxygen permeation fluxes: (a) temperature dependence for BFLZ disc membranes with a thickness of 1.1 mm; (b) for membranes with various La contents at different temperatures. Feed side: 150 cm^3 (STP) min^{-1} synthetic air. Permeate side: 49 cm^3 (STP) min^{-1} He and 1 cm^3 (STP) min^{-1} of Ne (for calibration).

28° and 32° is marked and magnified in Fig. 1a. The secondary phase was identified as Ba$_6$La$_2$Fe$_4$O$_{15}$ with the space group $P6_3mc$, which belongs to the dihexagonal pyramidal class of crystal structures.[43] Thus, the highest La content in BFLZ for the formation of a pure cubic perovskite structure without any detectable impurities is about x = 0.04.

For a more precise evaluation of the effect of La incorporation, the XRD patterns of BFLZ at *ca.* 31.5° were magnified and compared, as shown in Fig. 1b. For low La contents ($x \leq 0.04$), the peak shifts gradually towards smaller angles with increasing La content from x = 0.025 to 0.04, indicating the expansion of the unit cell since the ionic radius of La^{3+}(VI) (1.03 Å) is larger than those of Fe^{3+} and Fe^{4+}. However, with further increasing La content in BFLZ from x = 0.05 to 0.075, the peak shifts back to bigger angles, which means that the BFLZ unit cell shrinks again. It seems that the La content in the perovskite phases is similar for x = 0.025 and 0.075, but maximum for x = 0.04. For the sample BFLZ (x = 0.05 and 0.075), with increasing La content, the foreign phase Ba$_6$La$_2$Fe$_4$O$_{15}$ is increasingly formed. La goes preferentially into this phase and the La content of the BFLZ perovskite phase decreases with increasing La content of the synthesis batch (x > 0.04).

The incorporation of La on the B-site of the BFLZ lattice is supported by the following three points. At first, BFLZ samples with La contents x = 0.025 and 0.04 consist of only a single cubic perovskite phase (see Fig. 1a). If La were to be incorporated on the A-site, secondary phases like barium oxide can be
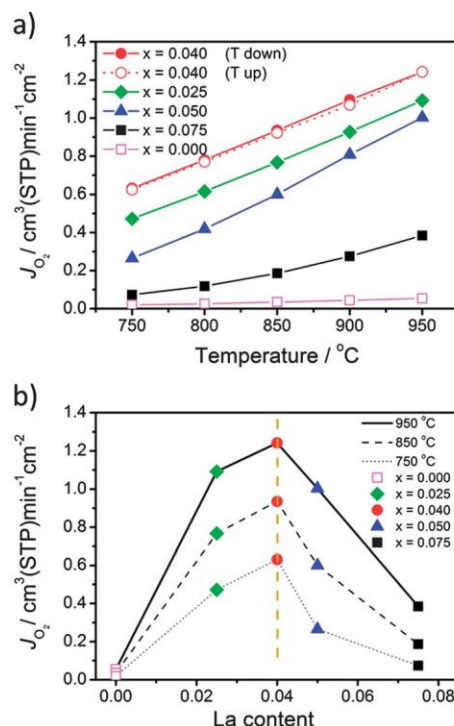
expected because the stoichiometry of the BFLZ composition would have changed. Second, for low La contents, the unit cell expands with increasing La content in a range from x = 0.025 to 0.04 (see Fig. 1b), which is a clear indication that La occupies the B-site of the BFLZ lattice. If La were to be on the A-site of the BFLZ lattice, the peak would shift towards higher angles since the ionic radius of La^{3+}(XII) (1.36 Å) is smaller than that of Ba^{2+}(XII) (1.61 Å). Third, doping La on the B-site increases the oxygen flux due to a higher oxygen vacancy concentration if the trivalent La^{3+} occupies tetravalent Fe^{4+} ion sites which was found in this paper.

Oxygen permeability

The oxygen permeation fluxes through BFLZ disc membranes as a function of temperature are presented in Fig. 2a. The oxygen permeation flux of all BFLZ membranes increases with increasing temperatures. For the BFLZ (x = 0.04) membrane, the effects of cooling and heating cycles on the oxygen permeation flux were also shown in Fig. 2a. Repeated cooling and heating cycles show no influence on the oxygen permeability. The change in oxygen permeation flux with varying La content at different temperatures is shown in Fig. 2b. For La content $\leq$ 0.04, the oxygen permeation flux increases with rising La content and reaches a maximum of 1.24 cm^3 (STP§) min^{-1} cm^{-2}

---

§ STP = standard temperature and pressure.

at 950 °C for the BFLZ composition with $x = 0.04$. It can be observed from Fig. 2 that the oxygen permeation flux of the membranes with cubic structure is significantly enhanced in comparison with the membrane of $BaFe_{0.95}Zr_{0.05}O_{3-\delta}$ with a rhombohedral structure. An increasing La content results in a higher oxygen vacancy concentration and a larger unit cell, both of which support an increase of the oxygen permeation flux. However, further increasing the La content ($x > 0.04$) leads to a decrease of the oxygen permeation flux in the samples with $x = 0.05$ and 0.075. This finding is attributed to the formation of the secondary phase $Ba_6La_2Fe_4O_{15}$ which (i) itself is not an oxygen ion conductor and (ii) collects the La from the BFLZ ($x = 0.05$ and 0.075) perovskite phases which results in a shrinking of the unit cell (see Fig. 1b).

Influence of the air and sweep gas flow rate on oxygen permeation

Fig. 3 shows the influence of the sweep gas (He) flow rate on the oxygen permeation flux through the BFLZ ($x = 0.025$) disc membrane at 950 °C. It can be seen that the oxygen permeation flux increases from 0.95 to 1.2 cm^3 (STP) min^{-1} cm^{-2} with increasing sweep gas flow rate from 30 to 100 cm^3 (STP) min^{-1}. An increase in the sweep gas flow rate, causing a reduced oxygen partial pressure on the permeate side, and an increase of feed gas flow rate reducing the effect of oxygen concentration depletion, can enhance the driving force for oxygen permeation through the membrane, which can be described by the Wagner equation:[44]

$$J_{O_2} = \frac{RT\sigma_i}{4^2 F^2 L} \ln \frac{P_{O_2,feed}}{P_{O_2,permeate}} \quad (2)$$

where σ_i is the ionic conductivity, R, F, T, and L denote the gas constant, Faraday constant, temperature, and thickness of the membrane, respectively. $P_{O_2,permeate}$ and $P_{O_2,feed}$ are the oxygen partial pressures on permeate and feed sides, respectively.

Bulk diffusion as a rate-limiting step for oxygen transport

For a better understanding of the effect of the O$_2$ partial pressure ratio across the disc membrane, the oxygen permeation
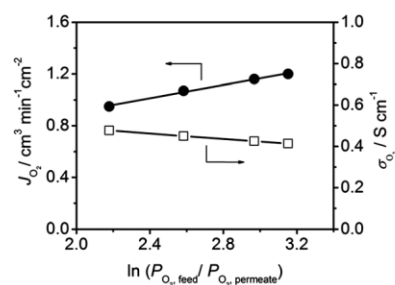

Fig. 4 Oxygen permeation rate and the calculated oxygen ionic conductivity of the BFLZ ($x = 0.025$) disc membrane as a logarithmic function of the oxygen partial pressure ratios on the feed and permeate sides at 950 °C, based on the data shown in the figure. Feed side: 150 cm^3 (STP) min^{-1} air. Permeate side: 29–99 cm^3 (STP) min^{-1} He and 1 cm^3 (STP) min^{-1} Ne (for calibration).

flux was plotted against the natural logarithmic ratios of oxygen partial pressures on feed and permeate sides (*i.e.* $\ln(P_{O_2,feed}/P_{O_2,permeate})$) as shown in Fig. 4. For the 1.1 mm thick BFLZ ($x = 0.025$) membrane under study, the oxygen permeation flux increases linearly with increasing logarithmic ratios of the oxygen partial pressures, which is in agreement with the prediction from the Wagner theory for bulk diffusion of oxygen ions as a rate-limiting step for oxygen transport (see eqn (2)).

According to the Wagner theory, the oxygen ionic conductivity of the OTM at various oxygen partial pressure ratios and temperatures can be calculated based on eqn (2):[45]

$$\sigma_i = J_{O_2} \frac{4^2 F^2 L}{RT} \left(\ln \frac{P_{O_2,feed}}{P_{O_2,permeate}} \right)^{-1} \quad (3)$$

The calculated oxygen ionic conductivity of the BFLZ ($x = 0.025$) disc membrane is also shown in Fig. 4. The oxygen ionic conductivity decreases linearly as a natural logarithmic function of the oxygen partial pressure ratios as it is predicted by eqn (3). At 950 °C, the oxygen ionic conductivity reaches a value of *ca.* 0.45 S cm^{-1} for the 1.1 mm thick BFLZ ($x = 0.025$) disc membrane at $\ln(P_{O_2,feed}/P_{O_2,permeate}) = 3.0$. Chen *et al.*[45] reported a higher value of oxygen ionic conductivity of *ca.* 1.4 S cm^{-1} for a 1.1 mm thick $Ba_{0.5}Sr_{0.5}Co_{0.8}Fe_{0.2}O_{3-\delta}$ (BSCF) disc membrane at 900 °C.
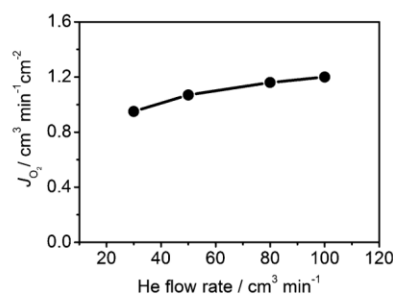
Fig. 3 Influence of the sweep gas (He) flow rate on the oxygen permeation flux through the BFLZ ($x = 0.025$) disc membrane with 1.1 mm thickness at 950 °C. Feed side: 150 cm^3 (STP) min^{-1} air. Permeate side: 29–99 cm^3 (STP) min^{-1} He and 1 cm^3 (STP) min^{-1} Ne (for calibration).

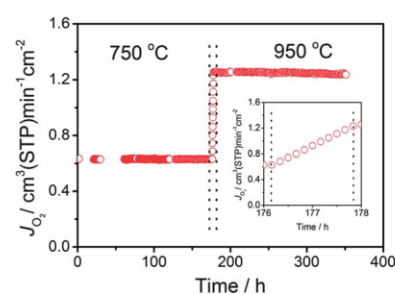**Fig. 5** Oxygen permeation flux through the BFLZ ($x = 0.04$) disc membrane with a thickness of 1.1 mm as a function of time at 750 and 950 °C. The inset shows the transition from 750 to 950 °C. Feed side: 150 cm^3 (STP) min^{-1} air. Permeate side: 49 cm^3 (STP) min^{-1} He and 1 cm^3 (STP) min^{-1} Ne (for calibration).

Table 2 Comparison of the oxygen permeation fluxes through several cobalt-free OTMs in disc geometry with 1.1 mm thickness under similar oxygen partial pressure gradient (air/inert sweep gas)

Membranes	Oxygen permeation flux/m^3 (STP) min^{-1} cm^{-2}		
	750 °C	950 °C	Ref.
$Ba(Fe_{0.91}La_{0.04}Zr_{0.05})O_{3-\delta}$	0.63	1.24	This work
$(Ba_{0.5}Sr_{0.5})(Fe_{0.8}Zn_{0.2})O_{3-\delta}$	0.36	0.98	18
$(Ba_{0.5}Sr_{0.5})(Fe_{0.8}Al_{0.1})O_{3-\delta}$	0.41^a	1.19	19
$(Ba_{0.5}Sr_{0.5})(Fe_{0.8}Cu_{0.2})O_{3-\delta}$	0.53	1.60	20
$Ba(Fe_{0.95}Y_{0.05})O_{3-\delta}$	0.48^a	0.93^a	21

^{a} Value is extrapolated.

Long-term oxygen permeation

High oxygen permeability and stability are two key factors for the industrial applications of OTMs. Fig. 5 shows the long-term operation of the BFLZ ($x = 0.04$) membrane with a thickness of 1.1 mm as a function of time at 750 and 950 °C. Stable oxygen permeation fluxes of 0.63 and 1.24 cm^3 (STP) min^{-1} cm^{-2} over 170 h were found at 750 and 950 °C, respectively. When the temperature was slowly increased from 750 °C to 950 °C with a heating rate of 2 °C min^{-1}, the oxygen permeation flux increases continuously (inset in Fig. 5). However, for BSCF, which is the most studied cobalt-based perovskite-type membrane material, the oxygen permeation flux continuously decreases with time at the intermediate temperature of 750 °C.[10,15,16,46] Efimov *et al.*[16] reported that the oxygen permeation flux of a BSCF membrane was reduced to 50% of its former value after 200 h. In our previous work, we found that the decay of the flux can be even larger. The oxygen permeation flux of a tube BSCF membrane was reduced by 1/3 after 120 h.[15]

The oxygen permeation flux through an OTM strongly depends on its composition, the membrane geometry such as the membrane thickness, and the operation conditions such as the temperature or the oxygen partial pressure ratio on the feed and permeate sides. Table 2 shows the oxygen permeation fluxes of several cobalt-free disc OTMs with the same thickness of 1.1 mm under similar experimental conditions. At 750 °C, our BFLZ ($x = 0.04$) disc membrane has a higher oxygen permeation flux with a reasonable long-term stability (see Fig. 5) than the other membranes in Table 2. Thus, compared to other cobalt-free perovskite-type membranes, the BFLZ ($x = 0.04$) membrane exhibits a higher oxygen permeability for oxygen separation in the intermediate temperature range.

Conclusions

The partial La-substitution for Fe on the B-site of $BaFe_{0.95-x}La_xZr_{0.05}O_{3-\delta}$ (BFLZ, $x \leq 0.04$) results in a cubic structure that is beneficial to oxygen permeation. The successful B-site doping by La^{3+} is indicated by (i) a single cubic perovskite phase of BFLZ with La contents $x = 0.025$ and 0.04, (ii) an increase of the unit cell as detected from XRD data since La^{3+} is larger than Fe^{3+} and Fe^{4+}, and (iii) an increased oxygen flux due to a higher oxygen vacancy concentration if trivalent La^{3+} occupies tetravalent Fe^{4+} ion sites. Only for La contents of $x \leq 0.04$ the pure cubic perovskite phase without any foreign phase as impurity was obtained. Moreover, the formation of the cubic structure of BFLZ by introducing La on the B-site increases significantly the oxygen permeability. For the La content of $x = 0.04$ with the largest volume of the cubic unit cell, the higher oxygen permeation flux with 0.63 and 1.24 cm^3 (STP) min^{-1} cm^{-2} was found at 750 and 950 °C, respectively. It follows from XRD that for La contents $x > 0.04$ the secondary phase $Ba_6La_2Fe_4O_{15}$ has been formed inside the BFLZ ($x = 0.05$ and 0.075) materials. The influence of oxygen partial pressures on the oxygen permeation flux and the oxygen ionic conductivity can be described with the Wagner theory for bulk diffusion of oxygen ions as a rate-limiting step for oxygen permeation. The result of the long-term oxygen permeability suggests that the BFLZ ($x = 0.04$) membrane exhibits good oxygen permeability and stability, which make this material a promising candidate for industrial applications such as oxygen separation from air and catalytic hydrocarbon partial oxidation.

Acknowledgements

Notes and references

1 J. Sunarso, S. Baumann, J. M. Serra, W. A. Meulenberg, S. Liu, Y. S. Lin and J. C. D. da Costa, *J. Membr. Sci.*, 2008, **320**, 13.

2 Y. Y. Liu, X. Y. Tan and K. Li, *Catal. Rev.: Sci. Eng.*, 2006, **48**, 145.

3 F. Y. Liang, H. Q. Jiang, T. Schiestel and J. Caro, *Ind. Eng. Chem. Res.*, 2010, **49**, 9377.

4 X. F. Zhu, S. M. Sun, Y. Cong and W. S. Yang, *J. Membr. Sci.*, 2009, **345**, 47.

5 H. J. M. Bouwmeester and A. J. Burggraaf, in *Fundamentals of Inorganic Membrane Science and Technology*, ed. A. J. Burggraaf and L. Cot, Elsevier 1996, p. 435.

6 J. Caro, K. J. Caspary, C. Hamel, B. Hoting, P. Kölsch, B. Langanke, K. Nassauer, T. Schiestel, A. Schmidt, R. Schomäcker, A. Seidel-Morgenstern, E. Tsotsas, I. Voigt, H. H. Wang, R. Warsitz, S. Werth and A. Wolf, *Ind. Eng. Chem. Res.*, 2007, **46**, 2286.

7 H. Q. Jiang, H. H. Wang, F. Y. Liang, S. Werth, T. Schiestel and J. Caro, *Angew. Chem., Int. Ed.*, 2009, **48**, 2983.

8 H. Q. Jiang, Z. W. Cao, S. Schirrmeister, T. Schiestel and J. Caro, *Angew. Chem., Int. Ed.*, 2010, **49**, 5656.

9 Z. P. Shao and S. M. Haile, *Nature*, 2004, **431**, 170.

10 Z. P. Shao, W. S. Yang, Y. Cong, H. Dong, J. H. Tong and G. X. Xiong, *J. Membr. Sci.*, 2000, **172**, 177.

11 J. F. Vente, S. McIntosh, W. G. Haije and H. J. M. Bouwmeester, *J. Solid State Electrochem.*, 2006, **10**, 581.

12 L. Qiu, T. H. Lee, L. M. Liu, Y. L. Yang and A. J. Jacobson, *Solid State Ionics*, 1995, **76**, 321.

13 Y. Teraoka, H. M. Zhang, S. Furukawa and N. Yamazoe, *Chem. Lett.*, 1985, 1743.

14 H. J. M. Bouwmeester, M. W. Den Otter and B. A. Boukamp, *J. Solid State Electrochem.*, 2004, **8**, 599.

15 F. Y. Liang, H. Q. Jiang, H. X. Luo, J. Caro and A. Feldhoff, *Chem. Mater.*, 2011, **23**, 4765.

16 K. Efimov, Q. A. Xu and A. Feldhoff, *Chem. Mater.*, 2010, **22**, 5866.

17 S. Švarcová, K. Wiik, J. Tolchard, H. J. M. Bouwmeester and T. Grande, *Solid State Ionics*, 2008, **178**, 1787.

18 H. H. Wang, C. Tablet, A. Feldhoff and J. Caro, *Adv. Mater.*, 2005, **17**, 1785.

19 J. Martynczuk, F. Y. Liang, M. Arnold, V. Sepelak and A. Feldhoff, *Chem. Mater.*, 2009, **21**, 1586.

20 K. Efimov, T. Halfer, A. Kuhn, P. Heitjans, J. Caro and A. Feldhoff, *Chem. Mater.*, 2010, **22**, 1540.

21 X. T. Liu, H. L. Zhao, J. Y. Yang, Y. Li, T. Chen, X. G. Lu, W. Z. Ding and F. S. Li, *J. Membr. Sci.*, 2011, **383**, 235.

22 X. F. Zhu, H. H. Wang and W. S. Yang, *Chem. Commun.*, 2004, 1130.

23 K. Watanabe, D. Takauchi, M. Yuasa, T. Kida, K. Shimanoe, Y. Teraoka and N. Yamazoe, *J. Electrochem. Soc.*, 2009, **156**, E81.

24 T. Kida, D. Takauchi, K. Watanabe, M. Yuasa, K. Shimanoe, Y. Teraoka and N. Yamazoe, *J. Electrochem. Soc.*, 2009, **156**, E187.

25 Y. Teraoka, H. Shimokawa, C. Y. Kang, H. Kusaba and K. Sasaki, *Solid State Ionics*, 2006, **177**, 2245.

26 T. Kida, A. Yamasaki, K. Watanabe, N. Yamazoe and K. Shimanoe, *J. Solid State Chem.*, 2010, **183**, 2426.

27 K. Zhang, R. Ran, L. Ge, Z. P. Shao, W. Q. Jin and N. P. Xu, *J. Alloys Compd.*, 2009, **474**, 477.

28 J. H. Tong, W. S. Yang, B. C. Zhu and R. Cai, *J. Membr. Sci.*, 2002, **203**, 175.

29 L. Yang, L. Tan, X. H. Gu, W. Q. Jin, L. X. Zhang and N. P. Xu, *Ind. Eng. Chem. Res.*, 2003, **42**, 2299.

30 S. Yakovlev, C. Y. Yoo, S. Fang and H. J. M. Bouwmeester, *Appl. Phys. Lett.*, 2010, **96**, 254101.

31 R. D. Shannon, *Acta Crystallogr., Sect. A: Cryst. Phys., Diffr., Theor. Gen. Crystallogr.*, 1976, **32**, 751.

32 P. Y. Zeng, Z. P. Shao, S. M. Liu and Z. P. Xu, *Sep. Purif. Technol.*, 2009, **67**, 304.

33 A. Feldhoff, J. Martynczuk and H. Wang, *Prog. Solid State Chem.*, 2007, **35**, 339.

34 A. Feldhoff, M. Arnold, J. Martynczuk, T. M. Gesing and H. Wang, *Solid State Sci.*, 2008, **10**, 689.

35 H. X. Luo, H. Q. Jiang, K. Efimov, F. Y. Liang, H. H. Wang and J. Caro, *Ind. Eng. Chem. Res.*, 2011, **50**, 13508.

36 F. Y. Liang, H. Q. Jiang, H. X. Luo, R. Kriegel and J. Caro, *Catal. Today*, 2012, **193**, 95.

37 V. M. Goldschmidt, *Naturwissenschaften*, 1926, **14**, 477.

38 X. F. Zhu, H. H. Wang and W. S. Yang, *Solid State Ionics*, 2006, **177**, 2917.

39 M. V. Patrakeev, E. B. Mitberg, A. A. Lakhtin, I. A. Leonidov, V. L. Kozhevnikov, V. V. Kharton, M. Avdeev and F. M. B. Marques, *J. Solid State Chem.*, 2002, **167**, 203.

40 J. C. Waerenborgh, D. P. Rojas, A. L. Shaula, G. C. Mather, M. V. Patrakeev, V. V. Kharton and J. R. Frade, *Mater. Lett.*, 2005, **59**, 1644.

41 Y. Rizki, Y. Breard, J.-M. Le Breton, E. Folcke, L. Lechevallier, W. Kobayashi and A. Maignan, *Solid State Sci.*, 2010, **12**, 1661.

42 S. Mori, *J. Am. Ceram. Soc.*, 1966, **49**, 600.

43 H. Mevs and H. Mullerbuschbaum, *J. Less-Common Met.*, 1990, **157**, 173.

44 C. H. Chen, H. J. M. Bouwmeester, R. H. E. vanDoorn, H. Kruidhof and A. J. Burggraaf, *Solid State Ionics*, 1997, **98**, 7.

45 Z. H. Chen, Z. P. Shao, R. Ran, W. Zhou, P. Y. Zeng and S. M. Liu, *J. Membr. Sci.*, 2007, **300**, 182.

46 A. C. van Veen, M. Rebeilleau, D. Farrusseng and C. Mirodatos, *Chem. Commun.*, 2003, 32.

This journal is © The Royal Society of Chemistry 2013

J. Mater. Chem. A, 2013, **1**, 746–751 | **751**

68

5 Dual phase membrane for oxygen permeation and the partial oxidation of methane

5.1 Summary

So far, the most studied oxygen-permeable materials are single-phase perovskite since these materials possess high oxygen permeability. However, most of these perovskite-type materials have stability problems in a low oxygen partial pressure atmosphere, and especially in a CO_2 containing atmosphere. Dual phase membranes which consist of an oxygen ionic conducting phase and an electronic conducting phase in a micro-scale phase mixture are considered to be promising substitutes for the single phase MIEC (Mixed Ionic Electronic Conductor) membranes. In addition to good phase stability in CO_2 and reducing atmospheres, their chemical compositions can be tailored according to practical requirements.

In this chapter, a novel cobalt-free noble metal-free dual phase oxygen transporting membrane with the composition $40Pr_{0.6}Sr_{0.4}FeO_{3-\delta}$ - $60\ Ce_{0.9}Pr_{0.1}O_{2-\delta}$ (40PSFO-60CPO) has been developed by using the one-pot one-step glycine-nitrate combustion technique. In this dual phase system, CPO is the main phase for ionic transport, and PSFO is the main phase for electronic transport. However, the latter phase PSFO also assists the ionic transport. In-situ XRD demonstrated that the 40PSFO-60CPO dual phase membrane shows a good phase stability not only in air but also in 50 vol.% CO_2/50 vol.% N_2 atmosphere. At 950 °C using pure He as sweep gas, a stable oxygen permeation flux of 0.26 $cm^3(STP)cm^{-2}min^{-1}$ is obtained through the 40PSFO-60CPO dual phase membrane. Whereas, an oxygen permeation flux of 0.18 $cm^3(STP)cm^{-2}min^{-1}$ through the 40PSFO-60CPO dual phase membrane was obtained when using pure CO_2 as sweep gas. The POM to syngas in the 40PSFO-60CPO dual phase reactor was successfully performed. Methane conversion was found to be higher than 99.0 % with 97.0 % CO selectivity, a 4.4 $cm^3(STP)cm^{-2}min^{-1}$ oxygen permeation flux was obtained under a steady state condition at 950 °C. XRD indicated that the spent membrane operated for 100 h in the POM to synthesis gas retained its dual phase structure, which suggests that the 40PSFO-60CPO dual phase membrane is chemically stable under a reducing atmosphere.

5.2 A novel cobalt-free noble metal-free oxygen-permeable $40Pr_{0.6}Sr_{0.4}FeO_{3-\delta}$ - $60Ce_{0.9}Pr_{0.1}O_{2-\delta}$ dual phase membrane

Huixia Luo, Heqing Jiang, Tobias Klande, Zhengwen Cao, Fangyi Liang, Haihui Wang, Jürgen Caro,

Chemistry of Materials 24 (2012) 2148-2154.

Novel Cobalt-Free, Noble Metal-Free Oxygen-Permeable 40Pr$_{0.6}$Sr$_{0.4}$FeO$_{3-\delta}$−60Ce$_{0.9}$Pr$_{0.1}$O$_{2-\delta}$ Dual-Phase Membrane

Huixia Luo,[†] Heqing Jiang,[‡] Tobias Klande,[†] Zhengwen Cao,[†] Fangyi Liang,[†] Haihui Wang,*,[§] and Jürgen Caro*,[†]

[†]Institute of Physical Chemistry and Electrochemistry, Leibniz University Hannover, Callinstrasse 3A, D-30167 Hannover, Germany

[‡]Max-Planck-Institut für Kohlenforschung, Kaiser-Wilhelm-Platz 1, D-45470 Mülheim an der Ruhr, Germany

[§]School of Chemistry & Chemical Engineering, South China University of Technology, No. 381 Wushan Road, 510640 Guangzhou, China

ABSTRACT: A novel cobalt-free and noble metal-free dual-phase oxygen-transporting membrane with a composition of 40 wt % Pr$_{0.6}$Sr$_{0.4}$FeO$_{3-\delta}$−60 wt % Ce$_{0.9}$Pr$_{0.1}$O$_{2-\delta}$ (40PSFO−60CPO) has been successfully developed via an in situ one-pot one-step glycine-nitrate combustion process. In situ XRD demonstrated that the 40PSFO−60CPO dual-phase membrane shows a good phase stability not only in air but also in 50 vol % CO$_2$/50 vol % N$_2$ atmosphere. When using pure He or pure CO$_2$ as sweep gases, at 950 °C steady oxygen permeation fluxes of 0.26 cm^3 min^{-1} cm^{-2} and 0.18 cm^3 min^{-1} cm^{-2} are obtained through the 40PSFO−60CPO dual-phase membrane. The partial oxidation of methane (POM) to syngas was also successfully investigated in the 40PSFO−60CPO dual-phase membrane reactor. Methane conversion was found to be higher than 99.0% with 97.0% CO selectivity and 4.4 cm^3 min^{-1} cm^{-2} oxygen permeation flux in steady state at 950 °C. Our dual-phase membrane - without any noble metals such as Ag, Pd or easily reducible metals oxides of Co or Ni - exhibits high oxygen permeation fluxes as well as good phase stability at high temperatures. Furthermore, the dual-phase membrane shows a good chemical stability under the harsh conditions of the POM reaction and in a CO$_2$ atmosphere at high temperatures.

KEYWORDS: *dual-phase membrane, CO$_2$-stable membrane, glycine-nitrate combustion process (GNP), oxygen permeation, partial oxidation of methane (POM)*
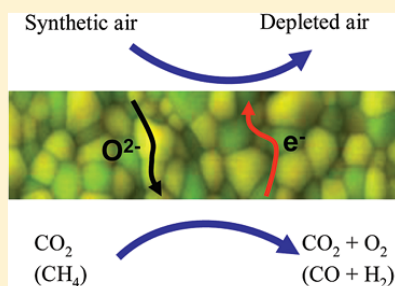
1. INTRODUCTION

Clean energy delivery is a global goal to avert the climate change impacts arising from greenhouse gas emissions. Oxygen transport membranes (OTMs) with mixed ionic-electronic conductivity are attractive as environmentally friendly, economical, and efficient means of producing oxygen from air,[1,2] for example, for catalytic hydrocarbon partial oxidations such as the conversion of natural gas into synthesis gas.[3,4] In addition, oxygen permeable membranes have been rapidly becoming attractive because of their potential oxygen supply to power stations with CO$_2$ capture according to the oxy-fuel concept[5,6] by using flue gas as sweep gas. Further promising applications are high-temperature catalytic membrane reactors for hydrocarbon conversion into syngas and added-value products[7,8] and the thermal decomposition of carbon dioxide in combination with the partial oxidation of methane to syngas.[9,10]

Over the last two decades, much efforts have been directed on the development of perovskite-type oxide membranes with the general formula ABO$_3$ (A = alkaline earth metals or lanthanide element; B = transition metal). Typically, alkaline earth cobaltites such as Ba$_{1-x}$Sr$_x$Co$_{1-y}$Fe$_y$O$_{3-\delta}$,[11,12] Ba-Co$_{1-y}$Fe$_y$O$_{3-\delta}$,[13] and SrCo$_{1-y}$Fe$_y$O$_{3-\delta}$[14] were fabricated as

high oxygen permeation membranes. However, their wide-spread applications of the above oxygen permeation membranes are hampered owing to the poor phase stability and chemical stability under a large oxygen concentration gradient, with one side of the membrane exposed to air as oxidizing atmosphere and the other side to a reducing or CO$_2$ containing atmosphere.[15,16] At present, new CO$_2$-stable materials are attracting much interest. So far, some CO$_2$-tolerant OTMs, such as K$_2$NiF$_{4-\delta}$-type (Pr$_{0.9}$La$_{0.1}$)$_2$(Ni$_{0.74}$Cu$_{0.21}$Ga$_{0.05}$)O$_{4-\delta}$,[17,18] La$_2$NiO$_{4-\delta}$,[19] perovskite-type La$_{0.6}$Ca$_{0.4}$Co$_{0.8}$Fe$_{0.2}$O$_{3-\delta}$[20] fluorite-type Ce$_{1-x}$Tb$_x$O$_{2-\delta}$ + Co,[21] have been reported. Recently, we have developed novel cobalt-free CO$_2$-tolerant dual-phase OTMs which consist of a mixture of pure ionic and pure electronic conducting oxides, such as NiFe$_2$O$_4$−Ce$_{0.9}$Gd$_{0.1}$O$_{2-\delta}$(NFO-CGO)[22,23] and Fe$_2$O$_3$−Ce$_{0.9}$Gd$_{0.1}$O$_{2-\delta}$ (FO-CGO).[24] Very recently, Zhu et al.[25] have reported a novel CO$_2$-stable dual-phase membrane which is made of ionic conducting oxides and mixed conducting oxides, showing 1 order of magnitude higher oxygen permeation fluxes than the

2148   dx.doi.org/10.1021/cm300710p | *Chem. Mater.* 2012, 24, 2148−2154

traditional dual-phase membranes. However, most of the above-mentioned materials contain easily reducible metals oxides of Co or Ni in their composition, which is unfavorable for the membrane stability in reducing atmospheres. Therefore, it is highly desired to develop novel OTMs with high stability under real application conditions, especially in the presence of gases like CO_2, CH_4, etc.

In the present work, we report the development a novel cobalt-free noble-metal free dual-phase membrane material, 40 wt % $Pr_{0.6}Sr_{0.4}FeO_{3-\delta}$—60 wt % $Ce_{0.9}Pr_{0.1}O_{2-\delta}$ (abbreviated as 40PSFO−60CPO). The 40PSFO−60CPO dual-phase material was prepared via an in situ one-pot one-step glycine-nitrate combustion process. In this dual-phase system, CPO is the main phase for ionic transport, and PSFO is the main phase for electronic transport, however, the latter phase PSFO also assists the ionic transport. Phase structure and stability as well as oxygen permeability are investigated under different atmospheres at high temperatures. Special attention is paid to the stability under CO_2 and the reducing atmosphere of CH_4.

2. EXPERIMENTAL SECTION

2.1. Preparation of Powders and Membranes.
The 40 wt % $Pr_{0.6}Sr_{0.4}FeO_{3-\delta}$—60 wt % $Ce_{0.9}Pr_{0.1}O_{2-\delta}$ dual-phase powder mixture was directly synthesized via an in situ one-pot one-step glycine-nitrate combustion process (GNP), a proven means of obtaining fine and homogeneous powders.[26] The process flowchart
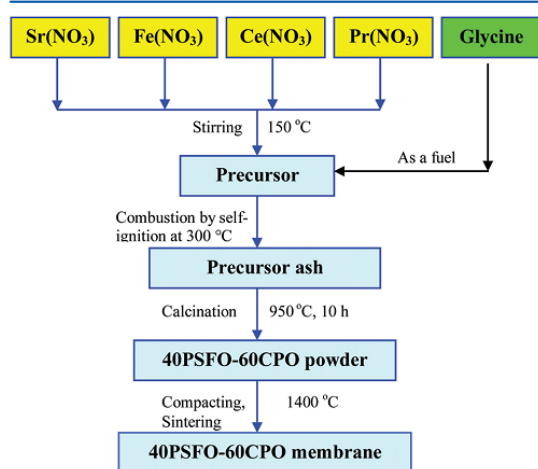

Figure 1. Flowchart for the one-pot one-step preparation of dual-phase 40 wt % $Pr_{0.6}Sr_{0.4}FeO_{3-\delta}$—60 wt % $Ce_{0.9}Pr_{0.1}O_{2-\delta}$ (40PSFO−60CPO) membranes by the glycine-nitrate combustion process.

is shown in Figure 1. A precursor was prepared by combining glycine and the metal nitrates $Sr(NO_3)_2$, $Fe(NO_3)_3$, $Ce(NO_3)_3$ and $Pr(NO_3)_3$ in their appropriate stoichiometric ratios in an aqueous solution. The molar ratio of glycine: total metal ions was 2: 1. The precursor was stirred and heated at 150 °C in air to evaporate excess water until a viscous liquid was obtained. Further heating of the viscous liquid up to 300 °C caused the precursor liquid to autoignite. Combustion was rapid and self-sustaining, and a precursor ash was obtained. For comparison, the single phase $Pr_{0.6}Sr_{0.4}FeO_{3-\delta}$ (PSFO) and $Ce_{0.9}Pr_{0.1}O_{2-\delta}$ (CPO) materials were also prepared via the GNP method. All the powders were calcined at 950 °C in air for 10 h. The 40PSFO−60CPO powders were pressed to disk membranes under a pressure of 5 MPa in a stainless steel module with a diameter of 18

mm to get green disk membranes. These green disks were sintered at 1400 °C in air for 5 h. The surfaces of the disks were carefully polished to 0.6 mm thickness by using 1200 grit-sandpaper (average particle diameter 15.3 μm), then the membranes were washed with ethanol.

2.2. Characterizations of Powders and Membranes.
X-ray diffraction (XRD, D8 Advance, Bruker-AXS, with Cu Kα radiation) was used to determine the phase structure of the dual-phase membranes after sintering at 1400 °C for 5 h. Data sets were recorded in a step-scan mode in the 2θ range of 20° - 80° with intervals of 0.02°. In situ XRD was conducted in a high-temperature cell HTK-1200N (Anton-Paar) from 30 to 1000 °C. The in situ XRD studies in air and a 50 vol % CO_2/50 vol % N_2 atmosphere were performed with a heating rate of 12 °C min^{-1}. At each temperature step, the sample was held for 50 min for the thermal equilibrium before diffraction data collection. The disk membranes were studied by scanning electron microscopy (SEM) and back scattered SEM (BSEM) using a JEOL JSM-6700F at an excitation voltage of 20 keV. The element distribution in the grains of the fresh dual-phase membranes under study was investigated on the same electron microscope by energy dispersive X-ray spectroscopy (EDXS), Oxford Instruments INCA-300 EDX spectrometer with an ultrathin window at an excitation voltage of 20 keV.

2.3. Oxygen Permeation and POM Performances of Membranes.
Oxygen permeation was studied using air as feed gas and He or CO_2 as sweep gas using a homemade high-temperature oxygen permeation device, which is described in a previous paper.[24] The disk membranes were sealed onto a alumina tube at 950 °C for 5 h with a gold paste (Heraeus, Germany), the side wall of the membrane disk was also covered with the gold paste to avoid any contribution to the oxygen permeation flux. The effective areas of the membranes for oxygen permeation were 0.785 cm^2. All the inlet gas flow rates were controlled by gas mass flow controllers (Bronkhorst, Germany) and all flow rates were regularly calibrated by using a bubble flow meter. Synthetic air (20% O_2 and 80% N_2) with a flow rate of 150 cm^3 min^{-1} was the feed; a mixture of He or CO_2 (29 cm^3 min^{-1}) and Ne (1 cm^3 min^{-1}) as the internal standard gas was fed to the sweep side.

In addition, the 40PSFO−60CPO dual-phase membrane has been used as a membrane reactor for POM. The membrane reactor configuration for POM was described elsewhere.[25] A Ni-based catalyst (0.3 g, Süd Chemie AG) was loaded on the top of the membrane disk and then the temperature of the reactor was increased to 950 °C with a heating rate of 2 °C min^{-1}. All gas lines to the reactor and the gas chromatograph were heated to 180 °C. High-purity methane of 7.32 cm^3 min^{-1} without dilution was used as the reactant for the POM to synthesis gas. Gas composition was analyzed by an online gas chromatograph (GC, Agilent 6890A).

3. RESULTS AND DISCUSSION

3.1. Characterizations of the 40PSFO−60CPO Dual-Phase Materials.
Figure 2 shows the XRD patterns of the PSFO, CPO, 40PSFO−60CPO powders after calcination at 950 °C for 10 h and the 40PSFO−60CPO dual-phase membrane after sintered at 1400 °C for 5 h. The XRD characterization indicates that both the calcined dual-phase powder and the sintered membrane consist of only the orthorhombic distorted perovskite PSFO and the cubic fluorite CPO phases, suggesting that the coexistence of PSFO and CPO is stable. The unit cell parameters of the pure CPO ($a = b = c = 5.4110$ Å, space group No. 225: $Fm3m$) and PSFO ($a = 5.4828$ Å, $b = 7.7855$ Å, $c = 5.4855$ Å, space group No. 74: $Imma$) are similar in the 40PSFO−60CPO dual-phase powder (CPO: $a = b = c = 5.4132$ Å, PSFO: $a = 5.4906$ Å, $b = 7.7667$ Å, $c = 5.5244$ Å) and the sintered membrane (CPO: $a = b = c = 5.4117$ Å, PSFO: $a = 5.4930$ Å, $b = 7.7974$ Å, $c = 5.4945$ Å). It is worth to note that even though the dual-phase mixture preparation by the one-pot one-step GNP method, no additional phases, such
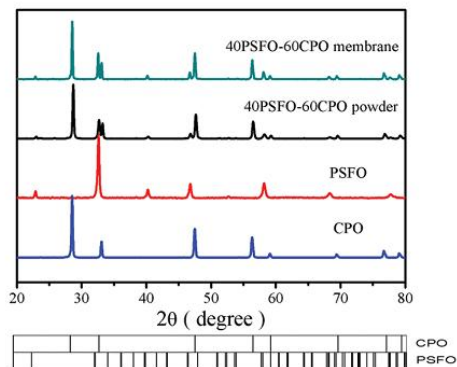
Figure 2. XRD patterns of CPO, PSFO and the dual-phase 40PSFO−60CPO powder calcined at 950 °C for 10 h and the 40PSFO−60CPO dual-phase membrane sintered at 1400 °C for 5 h (see Figure 1).

as PrFeO$_3$ and SrPrFeO$_4$, were observed. Therefore, from the absence of foreign phase signals different from PSFO and CPO, it is concluded that the dual-phase membranes 40PSFO−60CPO can be successfully synthesized via a one-pot one-step GNP combustion process.

Figure 3 depicts the SEM, BSEM, and EDXS pictures of the 40PSFO−60CPO dual-phase membrane after sintering at 1400 °C for 5 h and before polishing at two different magnifications. Obviously, the microsized grains are packed closely; no major cracks are visible. The PSFO and CPO grains could be
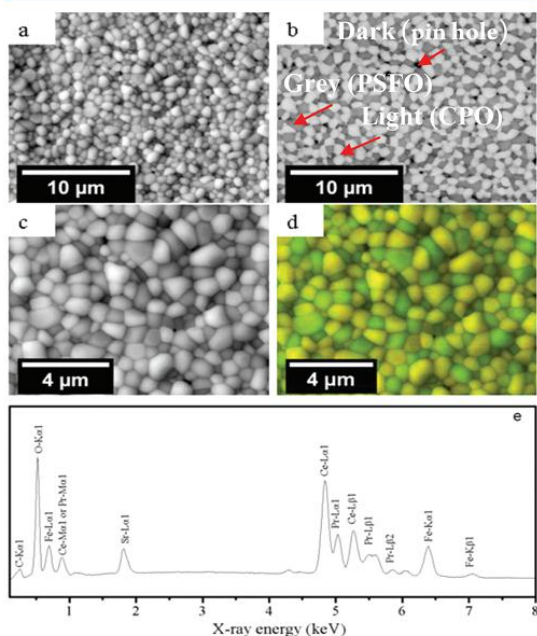
distinguished by BSEM and EDXS (Figure 3b, d). The two phases are well-distributed with clear grain boundaries, demonstrating the good chemical compatibility between the PSFO and CPO phases, which is in good agreement with the XRD results (Figure 2). However, there are three different contrast levels observable (dark, gray and light) in the BSEM. The dark spots in BSEM are pin holes, the gray grains are PSFO and the light ones are CPO since the contribution of the back scattered electrons to the SEM signal intensity is proportional to the atomic number (Figure 3b). The same information is provided by EDXS (Figure 3d, e), which suggests that the green color (gray in the black-and-white version) is an overlap of the Pr, Fe, and Sr signals, whereas the yellow color (light) stems from an average of the Ce and Pr signals. The mean grain size areas of PSFO and CPO have been estimated to 0.146 and 0.230 μm^2 from the analysis of 100 grains, respectively. Furthermore, the two phases are well-distributed and form a percolation network of both phases that can be clearly observed in the BSEM and EDXS micrographs, which is beneficial to the oxygen ion and electron transport.

3.2. Phase Stability of the 40PSFO−60CPO Dual-Phase Material. In situ XRD provides an effective and direct way to characterize high-temperature structure changes during increasing and decreasing temperatures under different atmospheres. The in situ XRD patterns of the calcined 40PSFO−60CPO powder in air with increasing temperature from 30 to 1000 °C, as shown in Figure 4, indicate that the

Figure 3. (a, c) SEM, (b) BSEM, and (d, e) EDXS images of the 40PSFO−60CPO membrane after sintered at 1400 °C for 5 h in air before polishing (see Figure 1). For the EDXS mapping in d, superimpositions of the Pr-Lα, Pr-Lβ, Sr-Lα, and Fe-Kα and Fe-Kβ (green) and Pr-Lα, Pr-Lβ and Ce-Lα, Ce-Lβ (yellow) signals have been used.

Figure 4. In situ XRD patterns of the 40PSFO−60CPO dual-phase powder after calcination at 950 °C (see Figure 1) in air for increasing temperature. Conditions: heating rate = 12 °C min^{-1}; equilibration time at each temperature, 50 min for recording the XRD data at each temperature.

phases CPO and PSFO remain unchanged in the 40PSFO−60CPO dual-phase material. The high-temperature phase stability has been studied by in situ XRD (Figure 5) between 30 and 1000 °C in an atmosphere of 50 vol % CO$_2$ and 50 vol % N$_2$. Figure 5 shows that the dual-phase membrane completely keeps its dual phases PSFO and CPO. No carbonate formation was observed in an atmosphere of 50 vol % CO$_2$ and 50 vol % N$_2$ in the temperature range of 30 and 1000 °C. These results suggest that the dual-phase membrane
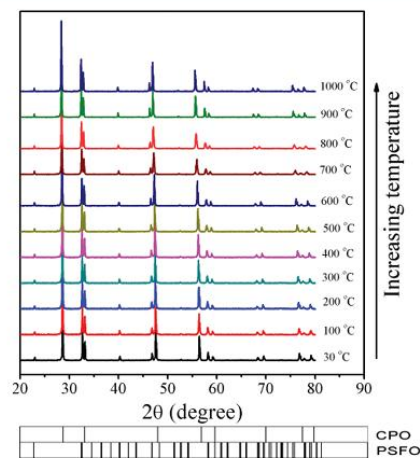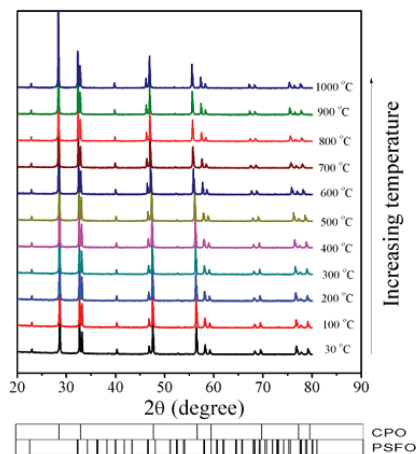
Figure 5. In situ XRD patterns of the 40PSFO−60CPO dual-phase powder after calcination at 950 °C (see Figure 1) in 50 vol % CO_2 and 50 vol % N_2 atmosphere for increasing temperatures. Conditions: heating rate = 12 °C min^{-1}; equilibration time at each temperature, 50 min for recording the XRD data at each temperature.

40PSFO−60CPO is thermally and chemically stable both in air and in CO_2 between 30 and 1000 °C.

3.3. Oxygen Permeability and Chemical Stability under CO_2 and CH_4 Atmospheres. To further assess the CO_2 stability of our dual-phase material during oxygen permeation, the oxygen permeation performance through the 40PSFO−60CPO dual-phase membrane was studied over 150 h using pure CO_2 as sweep gas. Figure 6 shows the oxygen
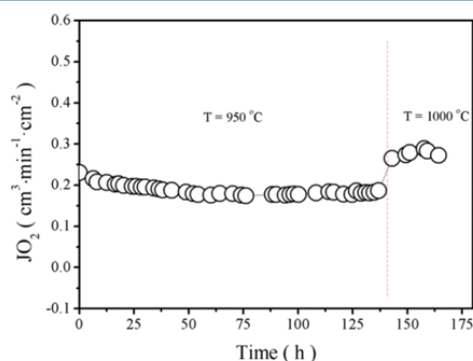

Figure 6. Oxygen permeation flux through 40PSFO−60CPO dual-phase membrane as a function of time with pure CO_2 as sweep gas. Conditions: 150 cm^3 min^{-1} air as feed gas, 29 cm^3 min^{-1} CO_2 as sweep gas; 1 cm^3 min^{-1} Ne as internal standard gas. Membrane thickness: 0.5 mm. Temperature: 950−1000 °C.

permeation flux as a function of time. It is found that the oxygen permeation flux decreased slightly from 0.22 cm^3 min^{-1} cm^{-2} and stabilized at the level of 0.18 cm^3 min^{-1} cm^{-2} with pure CO_2 as sweep gas at 950 °C. At 1000 °C, the oxygen permeation flux was kept constant at 0.28 cm^3 min^{-1} cm^{-2} for 20 h. This stable performance in CO_2 suggests that the 40PSFO−60CPO dual-phase membrane possess a high CO_2 stability. To benchmark the 40PSFO−60CPO material, the

oxygen permeation flux and stability under CO_2 have been compared with results of previously reported materials. From the comparison shown in Table 1, it follows that the oxygen permeation flux through the alkaline earth metal-containing single-phase perovskite membranes is higher than that of the dual-phase membranes, when He as sweep gas has been used. However, if CO_2 becomes the sweep gas, the oxygen permeation flux sharply decreased. The decrease of the oxygen permeation flux through most of these perovskite membranes was more than 90%. In some cases, the materials were even decomposed due to the carbonate formation.

It has been reported by Yi et al.[15] that the reaction of the$BaCo_{0.7}Fe_{0.2}Nb_{0.1}O_{3−\delta}$ membrane with CO_2 leads to a decomposition of the membrane and to the formation of a compact $BaCO_3$ surface layer and a porous decomposed zone; the latter consists of mainly CoO and a Co-depleted perovskite phase. However, 40PSFO−60CPO dual-phase membrane shows lower oxygen permeation fluxes than most of the alkaline earth metal-containing single-phase perovskite membranes, but it shows a much higher stability in CO_2. Moreover, compared with the dual-phase membranes $NiFe_2O_4$−$Ce_{0.9}Gd_{0.1}O_{2−\delta}$ and Fe_2O_3−$Ce_{0.9}Gd_{0.1}O_{2−\delta}$, we can see that our 40PSFO−60CPO membrane shows a higher oxygen permeation flux. However, the oxygen flux can be increased as well by technical measures such as an asymmetric membrane structures[28−30] or by surface enlargement as demonstrated for a hollow fiber.[31] Combining an asymmetric structure and surface enlargement, it was shown by Baumann et al.[28] that a sophisticated material processing using tape casting and cofiring results in high oxygen fluxes of up to 12.2 cm^3 (STP) min^{-1} cm^{-2} at 1000 °C for an oxygen partial pressure gradient with air on the feed side and Ar on the sweep side. The disk-shaped membrane consists of only the material BSCF: a gastight layer (70 μm) is deposited by tape casting on a porous substrate (830 μm) with 34% open porosity. An open-porous surface activation layer on the air side was prepared via screen printing and increases substantially the surface exchange rate and notably the oxygen permeation rate. A CGO membrane with an asymmetric structure, which was tested under oxy-fuel and syngas conditions by Kaiser et al.,[29,30] consists of an about 30 μm thick gastight CGO layer on top of an about 300 μm thick porous CGO support. The basic membrane structure was produced by tape casting, lamination and cosintering. For this type of asymmetric CGO membranes, three measures have been taken to increase the oxygen fluxes: (i) A thin dense CGO layer of only 30 μm thickness was used. (ii) Co_3O_4 (or Fe_2O_3) was used as sintering aids for membrane layer (and support) and as electronically conductive grain boundary phase. These metal oxides with high electron conductivities were found to be enriched in the grain boundaries, and (iii) the porous support layer was infiltrated with the perovskite $La_{0.6}Sr_{0.4}CoO_{3−\delta}$ (LSC) as air catalyst for incorporation of oxygen into the membrane.

Furthermore, we also found that the 40PSFO−60CPO dual-phase membrane reactor was successfully operated in the partial catalytic oxidation of methane (POM) to synthesis gas (see Figure 7). There is an activation period at the beginning, which is attributed to the reduction of Ni oxide to Ni^0 in the catalyst. A similar behavior was found in previous studies.[31] As shown in Figure 7, a CO selectivity of more than 90.0% was obtained in our POM, with about 99.0% methane conversion. After an activation period of 14 h, the CO selectivity can reach 97.0%, the CH_4 conversion remained 99.0% and the oxygen permeation flux through the 40PSFO−60CPO dual-phase

74

Table 1. Effect of CO_2 as sweep Gas on the Oxygen Permeation Flux through Several MIEC Membranes in Disk Geometry in Comparison with the Sweep Gas He

membrane materials	thickness (mm)	T (°C)	oxygen flux (cm^3 min^{-1} cm^{-2}) air/ He	oxygen flux (cm^3 min^{-1} cm^{-2}) air/ CO_2	ref
$BaCo_{0.8}Fe_{0.2}Nb_{0.1}O_{3-\delta}$	1	900	0.70	0	15
$Ba_{0.5}Sr_{0.5}Fe_{0.8}Zn_{0.2}O_{3-\delta}$	1.15	750	0.36	0	16
$Ba_{0.5}Sr_{0.5}Co_{0.8}Fe_{0.2}O_{3-\delta}$	1	875	1.9	0	27
$40wt.\%NiFe_2O_4-60wt.\%Ce_{0.9}Gd_{0.1}O_{2-\delta}$	0.5	950	0.18	0.16	22, 23
$40wt.\%Fe_2O_3-60wt.\%Ce_{0.9}Gd_{0.1}O_{2-\delta}$	0.5	950	0.10	0.08	24
$40wt.\%Pr_{0.6}Sr_{0.4}FeO_{3-\delta}-60wt.\%Ce_{0.9}Pr_{0.1}O_{2-\delta}$	0.6	950	0.27	0.18	this work
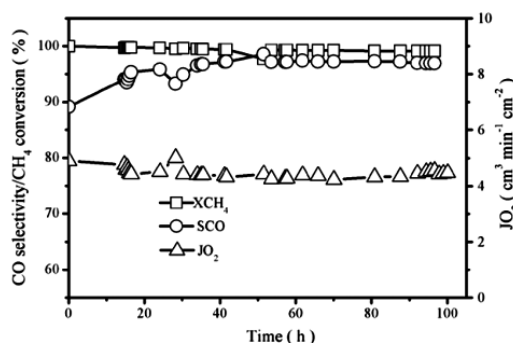
Figure 7. Time dependence of oxygen permeation flux ($\triangle$), CH_4 conversion ($\square$), and CO selectivity ($\bigcirc$) for 40PSFO−60CPO dual-phase membrane at 950 °C in the POM to synthesis gas. Conditions: 150 cm^3 min^{-1} air as feed gas, 7.32 cm^3 min^{-1} CH_4 as sweep gas; 1 cm^3 min^{-1} Ne as internal standard gas. Membrane thickness: 0.6 mm.

membrane reached 4.4 cm^3 min^{-1} cm^{-2} at 950 °C. These results indicate that 40PSFO−60CPO membranes possess good chemical stability under a reducing atmosphere such as in the POM, in combination with a high oxygen permeation flux.

After the steady state was reached, the influence of temperature on the CH_4 conversion, the CO selectivity and the oxygen permeation flux was investigated (Figure 8). It was found that the methane conversions increased from 80.5% to
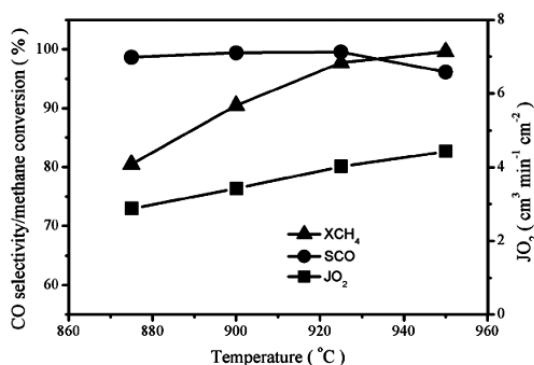
Figure 8. Influence of temperature on the CH_4 conversion ($\blacktriangle$), CO selectivity ($\bullet$), and oxygen permeation flux ($\blacksquare$) through the 40PSFO−60CPO dual-phase membrane in the POM to synthesis gas. Conditions: 150 cm^3 min^{-1} air as feed gas, 7.32 cm^3 min^{-1} CH_4 as sweep gas; 1 cm^3 min^{-1} Ne as internal standard gas. Membrane thickness: 0.6 mm.

99.6%, and the oxygen permeation fluxes increased from 2.9 cm^3 min^{-1} cm^{-2} to 4.4 cm^3 min^{-1} cm^{-2} with increasing temperatures from 875 to 950 °C. However, the CO selectivity decreased from 99.0% to 96.0%. This behavior has been observed also for single phase perovskite-type membrane reactors, e.g. using $BaCo_{0.7}Fe_{0.2}Ta_{0.1}O_{3-\delta}$.[33] The explanation for this phenomenon is as follows: (i) The increased oxygen permeation flux was ascribed to the increase of oxygen diffusion rate through the 40PSFO−60CPO membrane and the faster surface kinetics with increasing temperature. (ii) The methane conversion was mainly controlled by the amount of the permeated oxygen through the dense membrane. Therefore, the increase in the oxygen permeation flux results in an increase of methane conversion. (iii) With the increased oxygen permeation flux, there is more oxygen available than needed for the stoichiometric POM. Consequently, CO was deeper oxidized to CO_2, resulting in the decrease in the CO selectivity with increasing temperature.

In the POM to synthesis gas under industrial conditions, oxygen permeable membranes are operated under a highly reducing environment. Unfortunately, only a few perovskite-type membranes can keep their structures in such a harsh environment. In the open literature, it has been reported that carbonates and metals were found on the surface of the spent membrane in the POM because of the corrosive gases H_2, CO, CO_2, and H_2O destroying the membrane. For example, it has been found that cobalt-enriched particles were formed on the surface of a $BaCo_{0.7}Fe_{0.2}Ta_{0.1}O_{3-\delta}$ membrane after operating in the POM to synthesis gas for 400 h.[32] The perovskite-type $Ba_{0.5}Sr_{0.5}Co_{0.8}Fe_{0.2}O_{3-\delta}$ membrane has been found to be completely destroyed in a hydrogen-containing environment.[34] On the other hand, doped ceria is known as very prone to chemical expansion because of partial reduction of the cations, particularly at high temperatures in highly reducing atmospheres such as H_2 and CH_4.[12,35] It has been reported that ceria-based electrolytes (e.g., $Ce_{0.8}Gd_{0.2}O_{2-\delta}$) is hindered by poor mechanical strength, a problem notably undesirable for electrolyte-supported cells[36,37] or is limited to intermediate temperatures because of cracks induced by a chemical expansion gradient across the electrolyte (membrane) at temperatures above ca. 700 °C.[30,38] The CPO is reported to be even worse.[38] Therefore, it is necessary to test the structural stability of the dual-phase membrane under POM reaction conditions. After 100 h operation in POM to synthesis gas, both sides of the 40PSFO−60CPO dual-phase membrane were studied by XRD (see Figure 9). Comparing the fresh and spent 40PSFO−60CPO dual-phase membrane, no obvious difference in the XRD patterns except the gold diffraction peaks from the gold paste sealant was observed. Therefore, it can be concluded that the 40PSFO−60CPO dual-phase membrane keeps its dual-
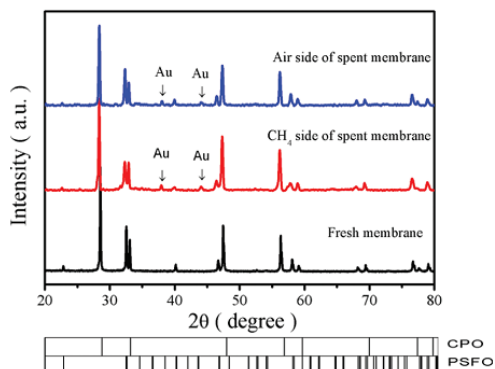
Figure 9. XRD patterns of fresh and spent 40PSFO−60CPO dual-phase membranes in the POM to synthesis gas after 100 h time on stream at 950 °C (see Figure 7).

phase structure, which suggests that 40PSFO−60CPO has a good chemical stability in the reducing POM atmosphere.

Figure 10 shows the temperature dependence of the oxygen permeation fluxes for the 40PSFO−60CPO dual-phase
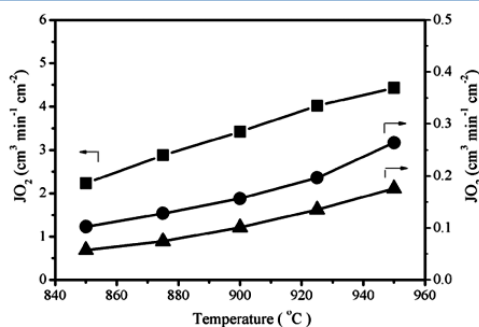

Figure 10. Temperature dependence of oxygen permeation fluxes through 40PSFO−60CPO dual-phase membranes using different gases as the sweep gas: CH_4 (■), He (●), or CO_2 (▲). Conditions: 150 cm^3 min^{-1} air as feed gas, 29 cm^3 min^{-1} He or CO_2 as sweep gas, or in POM reaction condition (7.32 cm^3 min^{-1} CH_4 as sweep gas, Ni-based catalyst as catalyst); 1 cm^3 min^{-1} Ne as internal standard gas. Membrane thickness: 0.6 mm.

membrane under different gas atmospheres. At 950 °C, a stable oxygen permeation flux of 0.26 cm^3 min^{-1} cm^{-2} is obtained through a membrane with a thickness of 0.6 mm, when He as sweep gas has been used. In the POM to synthesis gas, the oxygen permeation flux can be enhanced to 4.4 cm^3 min^{-1} cm^{-2}. According to the well-known Wagner theory, the

driving force is the oxygen partial pressure gradient between the two sides of the membrane. The presence of the reactive CH_4 lowers the oxygen partial pressure on the reaction side much more than He. Thus, the oxygen permeation flux through 40PSFO−60CPO with CH_4 as reactant was remarkably increased compared with the inert He. The oxygen permeation flux of our dual-phase membrane is higher or comparable with some single-phase perovskite-type and dual-phase-type OTMs in the POM to synthesis gas. As shown in Table 2, the oxygen permeation flux though our 40PSFO−60CPO membrane is higher than that of the single-phase perovskite-type membrane $Ba_{0.5}Sr_{0.5}Fe_{0.8}Zn_{0.2}O_{3-\delta}$ and comparable with them of dual-phase-type membranes (e.g., 40 wt % $Gd_{0.6}Sr_{0.4}FeO_{3-\delta}$−60 wt % $Ce_{0.8}Gd_{0.2}O_{2-\delta}$, 25 wt % $Sm_{0.6}Sr_{0.4}FeO_{3-\delta}$−75 wt % $Ce_{0.85}Sm_{0.15}O_{2-\delta}$, and 25 wt % $Sm_{0.6}Sr_{0.4}Fe_{0.7}Al_{0.3}O_{3-\delta}$−75 wt % $Ce_{0.85}Sm_{0.15}O_{2-\delta}$[31,39−42] under similar POM reaction conditions. Thus, we propose that the 40PSFO−60CPO dual-phase membrane is a promising membrane material for applications in the oxy-fuel process using CO_2 flue gas as sweep gas and high-temperature catalytic membrane reactors for hydrocarbon conversion into syngas and added-value products or thermal decomposition of carbon dioxide in combination with the partial oxidation of methane to syngas.

4. CONCLUSIONS

By using the one-pot one-step glycine-nitrate combustion technique, a novel cobalt-free noble metal-free dual-phase oxygen transporting membrane with the composition 40 wt % $Pr_{0.6}Sr_{0.4}FeO_{3-\delta}$−60 wt % $Ce_{0.9}Pr_{0.1}O_{2-\delta}$ (40PSFO−60CPO) has been developed. The membrane consists of a microscale mixture of well-separated PSFO (mixed ion-electron conductor) and CPO (oxygen ions conductor) grains forming a percolation network. According to its chemical composition, the new 40PSFO−60CPO dual-phase membrane is CO_2-stable. For a 0.6 mm thick membrane, a stable oxygen flux of 0.18 cm^3 min^{-1} cm^{-2} has been found at 950 °C when using CO_2 as sweep gas. The POM to syngas in the 40PSFO−60CPO dual-phase reactor was successfully performed. Methane conversion was found to be higher than 99.0% with 97.0% CO selectivity, a 4.4 cm^3 min^{-1} cm^{-2} oxygen permeation flux was obtained under a steady state condition at 950 °C. XRD indicated that the spent membrane operated for 100 h in the POM to synthesis gas retained its dual-phase structure, which suggests that the 40PSFO−60CPO dual-phase membrane is chemically stable under a reducing atmosphere.

■ AUTHOR INFORMATION

Corresponding Author
*E-mail: hhwang@scut.edu.cn (H.W.); juergen.caro@pci.uni-hannover.de (J.C.). Tel.: +86-20-8711-0131 (H.W.); +49-511-762-3175(J.C.). Fax: +86-20-8711-0131 (H.W.); +49-511-762-19121 (J.C.).

Table 2. Comparison of MIEC OTMs in Disk Geometries for Oxygen Separation under Similar POM Conditions

Mmembrane materials	thickness (mm)	T (°C)	oxygen flux (cm^3 min^{-1} cm^{-2})	catalyst	ref
$Ba_{0.5}Sr_{0.5}Fe_{0.8}Zn_{0.2}O_{3-\delta}$	1.25	900	2.6	Ni-based catalyst	31
$BaCe_{0.15}Fe_{0.85}O_{3-\delta}$	1.5	950	4.2	LiLaNiO/γ-Al$_2$O$_3$	39
40 wt % $Gd_{0.7}Sr_{0.3}FeO_{3-\delta}$−60 wt % $Ce_{0.8}Gd_{0.2}O_{2-\delta}$	0.5	950	2−5	LiLaNiO/γ-Al$_2$O$_3$	40
25 wt % $Sm_{0.6}Sr_{0.4}FeO_{3-\delta}$−75 wt % $Ce_{0.85}Sm_{0.15}O_{2-\delta}$	0.6	950	~4	LiLaNiO/γ-Al$_2$O$_3$	41
25 wt % $Sm_{0.6}Sr_{0.4}Fe_{0.7}Al_{0.3}O_{3-\delta}$−75 wt % $Ce_{0.85}Sm_{0.15}O_{2-\delta}$	0.5	950	~4.3	LiLaNiO/γ-Al$_2$O$_3$	42
40 wt % $Pr_{0.6}Sr_{0.4}FeO_{3-\delta}$− 60 wt % $Ce_{0.9}Pr_{0.1}O_{2-\delta}$	0.6	950	~4.4	Ni-based catalyst	This work

Chemistry of Materials

Article

Notes

The authors declare no competing financial interest.

■ REFERENCES

(1) Watenabe, K.; Yuasa, M.; Kida, T.; Teraoka, Y.; Yamazoe, N.; Shimanoe, K. *Adv. Mater.* **2010**, *22*, 2367.

(2) Watenabe, K.; Yuasa, M.; Kida, T.; Shimanoe, K.; Teraoka, Y.; Yamazoe, N. *Chem. Mater.* **2008**, *20*, 6965.

(3) Kniep, J.; Lin, Y. S. *Ind. Eng. Chem. Res.* **2011**, *50*, 7941.

(4) Chen, C. S.; Feng, S. J.; Ran, S.; Zhu, D. C.; Liu, W.; Bouwmeester, H. J. M. *Angew. Chem., Int. Ed.* **2003**, *42*, 5196.

(5) Smart, S.; Lin, C. X. C.; Ding, L.; Thambimuthu, K.; Dinizda Costa, J. C. *Energy Environ. Sci.* **2010**, *3*, 268.

(6) Engels, S.; Beggel, F.; Modigell, M.; Stadler, H. *J. Membr. Sci.* **2010**, *359*, 93.

(7) Yaremchenko, A. A.; Kharton, V. V.; Valente, A. A.; Snijkers, F. M. M.; Cooymans, J. F. C.; Luyten, J. J.; Marques, F. M. B. *J. Membr. Sci.* **2008**, *319*, 141.

(8) Slade, D. A.; Duncan, A. M.; Nordheden, K. J.; Stagg-Williams, S. M. *Green Chem.* **2007**, *9*, 577.

(9) Zhang, C.; Chang, X. F.; Fan, Y. Q.; Jin, W. J.; Xu, N. P. *Ind. Eng. Chem. Res.* **2007**, *46*, 2000.

(10) Jin, W. J.; Zhang, C.; Chang, X. F.; Fan, Y. Q.; Xin, W. H.; Xu, N. P. *Environ. Sci. Technol.* **2008**, *42*, 3064.

(11) Fang, S. M.; Yoo, C. Y.; Bouwmeester, H. J. M. *Solid State Ionics* **2011**, *195*, 1.

(12) Sunarso, J.; Baumann, S.; Serra, J. M.; Meulenberg, W. A.; Liu, S.; Lin, Y. S.; Diniz da Costa, J. C. *J. Membr. Sci.* **2008**, *320*, 13.

(13) Tong, J. H.; Yang, W. S.; Zhu, B. C.; Cai, R. *J. Membr. Sci.* **2002**, *203*, 175.

(14) Qiu, L.; Lee, T. H.; Liu, L. M.; Yang, Y. L.; Jacobson, A. J. *Solid State Ionics* **1995**, *76*, 321.

(15) Yi, J. X.; Schroeder, M.; Weirich, T.; Mayer, J. *Chem. Mater.* **2010**, *22*, 6246.

(16) Martynczuk, J.; Efimov, K.; Robben, L.; Feldhoff, A. *J. Membr. Sci.* **2009**, *344*, 62.

(17) Wei, Y. Y.; Tang, J.; Zhou, L. Y.; Xue, J.; Li, Z.; Wang, H. H. *AIChE J.* **2011**, DOI: 10.1002/aic.12802.

(18) Tang, J.; Wei, Y. Y.; Zhou, L. Y.; Li, Z.; Wang, H. H. *AIChE J.* **2011**, DOI: 10.1002/aic.12742.

(19) Klande, T.; Efimov, K.; Cusenza, S.; Becker, K. D.; Feldhoff, A. *J. Solid State Chem.* **2011**, *184*, 3310.

(20) Efimov, K.; Klande, T.; Juditzki, N.; Feldhoff, A. *J. Membr. Sci.* **2011**, *389*, 205.

(21) Balaguer, M.; Solís, C.; Serra, J. M. *Chem. Mater.* **2011**, *23*, 2333.

(22) Luo, H. X.; Efimov, K.; Jiang, H. Q.; Feldhoff, A.; Wang, H. H.; Caro, J. *Angew. Chem., Int. Ed.* **2011**, *50*, 759.

(23) Luo, H. X.; Jiang, H. Q.; Efimov, K.; Wang, H. H.; Caro, J. *AIChE J.* **2011**, *57*, 2738.

(24) Luo, H. X.; Jiang, H. Q.; Efimov, K.; Liang, F. Y.; Wang, H. H.; Caro, J. *Ind. Eng. Chem. Res.* **2011**, *50*, 13508.

(25) Zhu, X. F.; Liu, H. Y.; Cong, Y.; Yang, W. S. *Chem. Commun.* **2012**, *48*, 251.

(26) Mokkelbost, T.; Kaus, I.; Grande, T.; Einarsrud, M. A. *Chem. Mater.* **2004**, *16*, 5489.

(27) Arnold, M.; Wang, H. H.; Feldhoff, A. *J. Membr. Sci.* **2007**, *293*, 44.

(28) Baumann, S.; Serra, J. M.; Lobera, M. P.; Escolástico, S.; Schulze-Küppers, F.; Meulenberg, W. A. *J. Membr. Sci.* **2011**, *377*, 198.

(29) Lobera, M. P.; Serra, J. M.; Foghmoes, S. P.; Søgaard, M.; Kaiser, A. *J. Membr. Sci.* **2011**, *385−386*, 154.

(30) Kaiser, A.; Foghmoes, S.; Chatzichristodoulou, C.; Søgaard, M.; Glasscock, J. A.; Frandsen, H. L.; Hendriksen, P. V. *J. Membr. Sci.* **2011**, *378*, 51.

(31) Tan, X. Y.; Wang, Z. G.; Meng, B.; Meng, X. X.; Li, K. *J. Membr. Sci.* **2010**, *352*, 189.

(32) Wang, H. H.; Tablet, C.; Feldhoff, A.; Caro, J. *Adv. Mater.* **2005**, *17*, 1785.

(33) Luo, H. X.; Wei, Y. Y.; Jiang, H. Q.; Yuan, W. H.; Lv, Y. X.; Caro, J.; Wang, H. H. *J. Membr. Sci.* **2010**, *350*, 154.

(34) Tong, J. H.; Yang, W. S.; Suda, H.; Haraya, K. *Catal. Today* **2006**, *118*, 144.

(35) Pu, Z. Y.; Lu, J. Q.; Luo, M. F.; Xie, Y. L. *J. Phys. Chem. C* **2007**, *111*, 18695.

(36) Fagg, D. P.; Mather, G. C.; Frade, J. R. *Ionics* **2003**, *9*, 214.

(37) Fagg, D. P.; Kharton, V. V.; Frade, J. R. *J. Electroceram.* **2002**, *9*, 199.

(38) Fagg, D. P.; Marozau, I. P.; Shaula, A. L.; Kharton, V. V.; Frade, J. R. *J. Solid State Chem.* **2006**, *179*, 3347.

(39) Zhu, X. F.; Wang, H. H.; Cong, Y.; Yang, W. S. *Catal. Lett.* **2006**, *111*, 179.

(40) Zhu, X. F.; Yang, W. S. *AIChE J.* **2008**, *54*, 665.

(41) Zhu, X. F.; Li, Q. M.; He, Y. F.; Yang, W. S. *J. Membr. Sci.* **2010**, *360*, 454.

(42) Zhu, X. F.; Li, Q. M.; Cong, Y.; Yang, W. S. *Catal. Commun.* **2008**, *10*, 309.

6 Conclusions

This thesis is dedicated to the development and investigation of four membranes with different geometry (disc, tubular and hollow fiber) and different chemical composition $(Ba_{0.5}Sr_{0.5}Co_{0.8}Fe_{0.2}O_{3-\delta}$ (BSCF), $BaCo_xFe_yZr_{1-x-y}O_{3-\delta}$ (BCFZ), $BaFe_{0.95-x}La_xZr_{0.05}O_{3-\delta}$ (BFLZ), and $40Pr_{0.6}Sr_{0.4}FeO_{3-\delta}$-$60Ce_{0.9}Pr_{0.1}O_{2-\delta}$ (40PSFO-60CPO)) for oxygen permeation from air. As described in the first part of Section 2, phase stability of cobalt-based single phase perovskite-type BSCF membrane was first investigated in long-term oxygen production at 950 °C and 750 °C. At 950 °C, the BSCF tube membranes exhibit good long-term phase stability and a stable oxygen permeation flux. However, at the intermediate temperature of 750 °C, both the oxygen permeation flux and the oxygen purity decrease continuously. This behavior is related to the formation of two secondary phases that are a hexagonal perovskite, $Ba_{0.5\pm x}Sr_{0.5\pm x}CoO_{3-\delta}$, and a trigonal mixed oxide, $Ba_{1-x}Sr_xCo_{2-y}Fe_yO_5$, that evolved in the ceramic membrane made of cubic BSCF perovskite during the dynamic flow of oxygen through it. In the second part of this Section, after the identification of stable operation conditions of BSCF membrane, we studied the oxygen permeation at the temperature of 950 °C using dead-end BSCF tubes in a (i) pressure-driven process, (ii) vacuum process, and (iii) by combining both techniques. In all cases, a high oxygen purity of almost 100 vol.% can be obtained at operation temperatures $\geq$ 850 °C.

The second way to improve the stability problem of cobalt-based single phase OTM is to bring less reducible metal ion Zr^{4+} on the B position of the perovskite structure. As described in Section 3, a Zr-doped BCFZ hollow fiber membrane with improved stability was also investigated for the production of O_2-enriched air and of high-purity oxygen in a flow-through and in a dead-end permeator at high temperatures. In a flow-through type permeator, O_2-enriched air with an oxygen concentration of 30-50 vol.% is produced in a flow-through permeator from 1 bar of air as feed applying a vacuum pump to keep the pressure on the O_2-enriched air side at about 0.12 bar. This O_2-enriched air was used as pressurized feed in a dead-end type permeator for the production of pure oxygen at 0.05 bar. A high oxygen purity up to 99.9 vol.% and an oxygen permeation flux of 9.7 $cm^3(STP)cm^{-2}min^{-1}$ were obtained during a 150 h oxygen permeation with a feed of 50 vol.% O_2-enriched air at 4 bar and reduced pressure of

0.05 bar on the permeate side.

To solve the stability problem of the cobalt-based OTM, cobalt-free OTMs with high oxygen permeability were proposed. A Cobalt-free OTM of the composition BFLZ with the cubic structure was successfully developed by partial La-substitution for Fe on the B-site of $BaFe_{0.95}Zr_{0.5}O_{3-\delta}$. It was for the first time that the introduction of La on the B-site of a mixed oxide stabilized the cubic structure. Furthermore, the formation of the cubic structure of BFLZ increases significantly the oxygen permeability. The maximum oxygen permeation flux is found for a La-content of $x = 0.04$ with the largest volume of the cubic unit cell, reaching 0.63 and 1.24 $cm^3(STP)min^{-1}cm^{-2}$ for a 1.1 mm thick membrane at 750 and 950 °C, respectively. This finding is in complete agreement with the XRD structure analysis, showing that the highest B-site La-substitution of BFLZ under conservation of the pure cubic perovskite phase without forming any foreign phase was about $x = 0.04$. Moreover, stable oxygen permeation fluxes were obtained during the long-term oxygen permeation operation of the BFLZ ($x = 0.04$) membrane over 170 h at 750 and 950 °C, respectively.

Dual phase OTMs can solve not only the problem of the stability but also the problem of the carbonate formation of the cobalt-based OTM since that type of OTM usually contains alkaline earth metal cations. A novel cobalt-free noble metal-free dual phase OTM with the composition 40PSFO-60CPO has been developed. The membrane consists of a micro-scale mixture of well-separated PSFO (mixed ion-electron conductor) and CPO (oxygen ions conductor) grains forming a percolation network. According to its chemical composition, the new 40PSFO-60CPO dual phase membrane is CO_2-stable. Steady oxygen permeation fluxes of 0.26 and 0.18 $cm^3(STP)min^{-1}cm$ are obtained through the 40PSFO-60CPO dual phase membrane using pure He or pure CO_2 as sweep gases at 950 °C. Moreover, the POM to syngas in the 40PSFO-60CPO dual phase reactor was successfully performed. Methane conversion was found to be higher than 99.0 % with 97.0 % CO selectivity, a 7.8 cm^3 min^{-1} cm^{-2} oxygen permeation flux was obtained under a steady state condition at 950 °C. XRD indicated that the spent membrane operated for 100 h in the POM to synthesis gas retained its dual phase structure, which suggests that the 40PSFO-60CPO dual phase membrane is chemically stable under a reducing atmosphere. However, due to the low oxygen permeability of the dual phase membrane, the new chemical composition of dual phase membrane

needs improvement and should be further investigated.

In summary, this Ph. D. work presented the OMTs with three different geometries (disc, tubular and hollow fiber) for oxygen permeation from air. Compared to the conventional disk and tubular membranes, a hollow fiber membrane with a thin wall not only gives very high values of the membrane area per unit volume but also reduces the materials costs. In addition, the special problem of the high temperature sealing can be solved by keeping the two sealed ends of the hollow fiber membrane outside the high temperature zone. Thus, hollow fiber membrane is considered as the most promising candidate for the industrial application for the high-purity oxygen production and catalytic membrane reactors.

Moreover, according the requirement of the practical industrial application, OMTs with different chemical composition should be developed to adapt it. Four OMTs with different chemical composition (BSCF, BSFZ, BFLZ, and 40PSFO-60CPO) were developed and investigated in this thesis. The cobalt-based BSCF membrane can be used for high-purity oxygen production in the high temperature range due to its high oxygen transport properties and good phase stability at temperatures $\geq$ 850 °C. BCFZ membrane with improved stability in the intermediate temperature (ca. 500-850 °C) range can be applied in a wide temperature range. The cobalt-free BFLZ membrane was developed for the application in the intermediate temperature range instead of the cobalt-based membrane. The cobalt-free BFLZ membrane not only solves the phase stability problem of the cobalt-based OTMs, but also reduces the materials costs and the environment problem because of the high price and toxicity of cobalt. The dual phase 40PSFO-60CPO membrane was developed to solve the problem of the carbonate formation of the alkaline earth-based OTM in a CO_2 containing atmosphere.

Publications and conferences

Publications included in this thesis

1.   **Liang, F.Y.**; Partovi, K.; Jiang, H.Q.; Luo, H.X.; Caro, J. B-site La-doped $BaFe_{0.95-x}La_xZr_{0.05}O_{3-\delta}$ perovskite-type membranes for oxygen separation. *Journal of Materials Chemistry A* **2012**, DOI:10.1039/C1032TA00377E.

2.   **Liang, F.Y.**; Jiang, H.Q.; Luo, H.X.; Kriegel, R.; Caro, J. High-purity oxygen production by a dead-end $Ba_{0.5}Sr_{0.5}Co_{0.8}Fe_{0.2}O_{3-\delta}$ tube membrane. *Catalysis Today* **2012**, 193, 95-100.

3.   **Liang, F.Y.**; Jiang, H.Q.; Luo, H.X.; Caro, J.; Feldhoff, A. Phase Stability and Permeation Behavior of a Dead-End $Ba_{0.5}Sr_{0.5}Co_{0.8}Fe_{0.2}O_{3-delta}$ Tube Membrane in High-Purity Oxygen Production. *Chemistry of Materials* **2011**, 23, 4765-4772.

4.   **Liang, F.Y.**; Jiang, H.; Schiestel, T.; Caro, J. High-Purity Oxygen Production from Air Using Perovskite Hollow Fiber Membranes. *Industrial & Engineering Chemistry Research* **2010**, 49, 9377-9384.

5.   Luo, H.X.; Jiang, H.Q.; Klande, T.; Cao, Z.W.; **Liang, F.Y.**; Wang, H.H.; Caro, J. Novel Cobalt-Free, Noble Metal-Free Oxygen-Permeable $40Pr_{0.6}Sr_{0.4}FeO_{3-delta}$ - $60Ce_{0.9}Pr_{0.1}O_{2-delta}$, Dual-Phase Membrane. *Chemistry of Materials* **2012**, 24, 2148-2154.

Publications not included in this thesis

6.   **Liang, F.Y.**; Caro, J., Perovskite Membranes for High-Temperature Oxygen Separation. In *Membrane Engineering for the Treatment of Gases*, E. Drioli, Ed. RSC Publishing, **2011**; Vol. 2, p 192-222.

7.   Luo, H.X.; Jiang, H.Q.; Klande, T.; **Liang, F.Y.**; Cao, Z.W.; Wang, H.H.; Caro, J. Rapid glycine-nitrate combustion synthesis of the CO_2-stable dual phase membrane $40Mn_{1.5}Co_{1.5}O_{4-\delta}$ - $60Ce_{0.9}Pr_{0.1}O_{2-\delta}$ for CO_2 capture via an oxy-fuel process. *Journal of Membrane Science* **2012**, 423-424, 450-458.

8. Luo, H.X.; Jiang, H.Q.; Efimov, K.; **Liang, F.Y.**; Wang, H.H.; Caro, J. CO_2-Tolerant Oxygen-Permeable Fe_2O_3-$Ce_{0.9}Gd_{0.1}O_{2\text{-delta}}$ Dual Phase Membranes. *Industrial & Engineering Chemistry Research* **2011**, 50, 13508-13517.

9. Li, Y.S.; **Liang, F.Y.**; Bux, H.; Yang, W.S.; Caro, J. Zeolitic imidazolate framework ZIF-7 based molecular sieve membrane for hydrogen separation. *Journal of Membrane Science* **2010**, 354, 48-54.

10. Li, Y.S.; **Liang, F.Y.**; Bux, H.; Feldhoff, A.; Yang, W.S.; Caro, J. Molecular Sieve Membrane: Supported Metal-Organic Framework with High Hydrogen Selectivity. *Angewandte Chemie-International Edition* **2010**, 49, 548-551.

11. Jiang, H.Q.; Wang, H.H.; **Liang, F.Y.**; Werth, S.; Schirrmeister, S.; Schiestel, T.; Caro, J. Improved water dissociation and nitrous oxide decomposition by in situ oxygen removal in perovskite catalytic membrane reactor. *Catalysis Today* **2010**, 156, 187-190.

12. Jiang, H.Q.; **Liang, F.Y.**; Czuprat, O.; Efimov, K.; Feldhoff, A.; Schirrmeister, S.; Schiestel, T.; Wang, H.H.; Caro, J. Hydrogen Production by Water Dissociation in Surface-Modified $BaCo_xFe_yZr_{1\text{-}x\text{-}y}O_{3\text{-}\delta}$ Hollow-Fiber Membrane Reactor with Improved Oxygen Permeation. *Chemistry-a European Journal* **2010**, 16, 7898-7903.

13. Huang, A.S.; **Liang, F.Y.**; Steinbach, F.; Gesing, T.M.; Caro, J. Neutral and Cation-Free LTA-Type Aluminophosphate ($AlPO_4$) Molecular Sieve Membrane with High Hydrogen Permselectivity. *Journal of the American Chemical Society* **2010**, 132, 2140-2141.

14. Huang, A.S.; **Liang, F.Y.**; Steinbach, F.; Caro, J. Preparation and separation properties of LTA membranes by using 3-aminopropyltriethoxysilane as covalent linker. *Journal of Membrane Science* **2010**, 350, 5-9.

15. Martynczuk, J.; **Liang, F.Y.**; Arnold, M.; Sepelak, V.; Feldhoff, A. Aluminum-Doped Perovskites As High-Performance Oxygen Permeation Materials. *Chemistry of Materials* **2009**, 21, 1586-1594.

16. Jiang, H.Q.; Wang, H.H.; **Liang, F.Y.**; Werth, S.; Schiestel, T.; Caro, J. Direct

Decomposition of Nitrous Oxide to Nitrogen by In Situ Oxygen Removal with a Perovskite Membrane. *Angewandte Chemie-International Edition* **2009**, 48, 2983-2986.

17. Bux, H.; **Liang, F.Y.**; Li, Y.S.; Cravillon, J.; Wiebcke, M.; Caro, J. Zeolitic Imidazolate Framework Membrane with Molecular Sieving Properties by Microwave-Assisted Solvothermal Synthesis. *Journal of the American Chemical Society* **2009**, 131, 16000-16001.

Contribution to the conference

1. **Liang, F.Y.**; Partovi, K.; Jiang, H.Q.; Luo, H.X.; Caro, J. *12th International Conference on Inorganic Membranes*, 9th - 13th Juli **2012**, Enschede, The Netherlands, (**Talk**).

2. **Liang, F.Y.**; Jiang, H.Q.; Luo, H.X.; Kriegel, R.; Caro, J. *10th International Conference on Catalysis in Membrane Reactors*, 20th - 24th Juni **2011**, St. Petersburg, Russia, (**Poster**).

3. Diestel, L.; Dux, H.; **Liang, F.Y.**; Caro, J. *12th International Conference on Inorganic Membranes*, 9th - 13th Juli **2012**, Enschede, The Netherlands, (**Talk**).

4. Bux, H.; **Liang, F.Y.**; Li, Y.S.; Cravillon, J.; Wiebcke, M.; Kärger, J.; Hertäg, L.; Fritzsche, S.; van Baten, J.M.; Krishma, R.; Caro, J. *2nd International Conference on Metal-Organic Frameworks and Open Framework Compounds*, 5th - 8th September **2010**, Marseille, France, (**Talk**).

5. Huang, A.S.; **Liang, F.Y.**; Steinbach, F.; Gesing, T.M.; Caro, J. *16th International Zeolite Conference (16th IZC) joint with the 7th International Mesostructureed Materials Symposium (7th IMMS)*, 4th - 9th Juli **2010**, Sorrento, Italy, (**Poster**).

6. Jiang, H.Q.; Wang, H.H.; **Liang, F.Y.**; Werth, S.; Schirrmeister, S.; Schiestel, T.; Caro, J. *9th International Conference on Catalysis in membrane reactors*, 28th Juni - 2nd Juli **2009**, Lyon, France, (**Talk**).

7. Cravillon, J.; **Liang, F.Y.**; Bux, H.; Caro, J.; Wiebcke, M. *5th International Zeolite Membrane Meeting*, 23th - 26th May **2010**, Loutraki, Greece, (**Poster**).

8. Bux, H.; **Liang, F.Y.**; Li, Y.S.; Cravillon, J.; Wiebcke, M.; Caro, J. *5th International Zeolite Membrane Meeting*, 23th - 26th May **2010**, Loutraki, Greece, (**Talk**).

9. Bux, H.; **Liang, F.Y.**; Li, Y.S.; Cravillon, J.; Wiebcke, M.; Kärger, J.; Fritzsche, S.; Caro, J. *22th Deutsche Zeolith-Tagung*, 3th - 5th March **2010**, Munich, Germany, (**Talk**).

10. Martynczuk, J.; **Liang, F.Y.**; Arnold, M.; Sepelak, V.; Feldhoff, A. *The Microscopy Conference 2009*, 30th August - 4th September **2009**, Graz, Austria, (**Poster**).

11. Jiang, H.Q.; Wang, H.H.; **Liang, F.Y.**; Werth, S.; Schiestel, T.; Caro, J. *42nd Annual Meeting of the German Catalysis Society*, 11th - 13th March **2009**, Weimar, Germany, (**Talk**).

Curriculum Vitae

Personal data:

Name: Fangyi Liang

Date of birth: April 05th, 1979

Place of birth: Anhui, China

Nationality: Chinese

Marital status: Married, one child

Higher education:

Since 02/2009:   **Gottfried Wilhelm Leibniz University Hannover,** Germany

Scientific co-worker at the group of Prof. Dr. Jürgen Caro, Institute of Physical Chemistry and Electrochemistry,

10/2006 – 01/2009:   **Gottfried Wilhelm Leibniz University Hannover**, Germany
Master of Science Degree in "Material- and Nanochemistry",

Master thesis together with Prof. Dr. Jürgen Caro: Noble metal-doped perovskit Ba(Co$_a$Fe$_b$Zr$_c$)O$_{3-\delta}$ as acatalytic coating of BCFZ membranes for improved oxygen permeation

10/2002 – 08/2006:   **Fachhochschule Hildesheim/Holzminden/Göttingen**, Germany
Diplom-Ingenieur (FH) Degree in "Construction Chemistry",

09/1998 ─ 07/2001:   **Hefei University**, China

College degree in "Construction Material",

Erklärung zur Dissertation

Hiermit erkläre ich, dass ich die vorliegende Arbeit selbstständig verfasst und nur unter Verwendung der angegebenen Quellen und Hilfsmittel angefertigt habe. Die Dissertation ist nicht schon als Diplomarbeit oder ähnliche Prüfungsarbeit verwendet worden.

Hannover, Januar 2013

Fangyi Liang